A JOINED 3D/1D FINITE ELEMENT METHOD FOR AEROSERVOELASTIC ANALYSIS OF DAMAGED HALE AIRCRAFT WINGS

A Dissertation Presented to
The Academic Faculty

By

Hanif S. Hoseini

In Partial Fulfillment
of the Requirements for the Degree
Doctor of Philosophy
in the School of Aerospace Engineering

Georgia Institute of Technology

May 2018

A JOINED 3D/1D FINITE ELEMENT METHOD FOR AEROSERVOELASTIC ANALYSIS OF DAMAGED HALE AIRCRAFT WINGS

Approved by:

Prof. Dewey H. Hodges
Committee Chair
School of Aerospace Engineering
Georgia Institute of Technology

Prof. George Kardomateas
School of Aerospace Engineering
Georgia Institute of Technology

Prof. Julian J. Rimoli
School of Aerospace Engineering
Georgia Institute of Technology

Prof. Arash Yavari
School of Civil and Environmental Engineering
Georgia Institute of Technology

Prof. Donald White
School of Civil and Environmental Engineering
Georgia Institute of Technology

Date Approved: March 29, 2018

To my mother Maryam,

My brother Mahmoud,

My sister Yasaman,

My grandmother,

and to the memories of my uncle Reza,

and

My father Hasan ...

ACKNOWLEDGEMENTS

Throughout my life I have enormously benefited from the support, guidance, and friendship of many great people without which I could not have possibly accomplished this. I would like to take this opportunity to extend my sincere gratitude to them.

First and foremost, I would like to express my gratitude and deep respect to my advisor, mentor, and role model Prof. Dewey H. Hodges. No word can do justice to express how grateful I am for being his student. Not only is he a brilliant scholar, but also one of the most wonderful human beings I have ever come across in my life. He possesses a rare combination of knowledge, wisdom, and humility at the highest level. I strongly believe he is the best advisor one may find in academia and for me having the honor of being a student of his was a dream that finally came true.

I would also like to thank the members of my thesis committee, Prof. George Kardomateas, Prof. Julian Rimoli, Prof. Arash Yavari, and Prof. Donald White, for their insightful critique and valuable suggestions which have been indispensable in shaping this thesis. Helps and guidance of Prof. Olivier Bauchau from University of Maryland are also appreciated.

If it was not for the continuous support of Prof. Jeff Jagoda during my studies I would not have been able to finish my PhD. He has truly been my guardian angel at Georgia Tech. I also need to thank Dr. Shannon Croft whose counsels were of great help through ups and downs in Atlanta and Georgia Tech.

To the end of my life, I am indebted to all of my teachers, some of whom particularly stand out. I would like to thank my undergraduate and graduate adveisors in Iran, Prof. Mahmoud Hasheminejad from IAU-SR and Prof. Ahmad Fazelzadeh from Shiraz University for all the things they taught me and for supporting and encouraging me to embark on this journey to my dream. Also, I would like to thank Prof. Mojtaba Mahzoon from Shiraz University for being an immense source of knowledge and wisdom

for me. I also need thank Prof. Gordon Parker from Michigan Tech for his support and understanding and all the things I learned from him. I would be remiss if I do not mention Mr. Mohammad Ali Moshfeghi, Mr. Mohammad Reza Akbari, Mr. Mansour Paymard, and my long time teacher and friend Mr. Isaac Soltani. They have been a great source of inspiration and courage for me.

I would specially like to thank my buddy and my fellow Amir Hossein, as well as my best frieds Esmaeel, Hossein, Sadjad, Foad, Elaheh, and Ehsan whose company and friendship have been my true asset all along. Without them my life would have been dull and empty. I would also like to thank my friends and lab-mates at Aerospace Department, Farshad, Mohit, Pezhman, Anurag, Seundo, Arman, Arohi, and Ruthvik for their company, helps, and constructive discussions we have had during my studies. Support and understanding of staff members of Aerospace Department, specially my friends and colleagues at the business office and the office of graduate studies were of great assistance during my studies.

Last but not least, I need to thank my dear family members from the bottom of my heart. I cannot even imagine that I could have been able to achieve anything without their unconditional love and sincere blessings. They believed in me even when I seriously doubted myself. Forever, I owe them my PhD as well as my life.

TABLE OF CONTENTS

LIST OF TABLES

LIST OF FIGURES

SUMMARY

Nonlinear aeroelastic analysis of damaged High-Altitude-Long-Endurance aircraft wings is considered. The structural model consists of a full three-dimensional finite element continuum model for the damaged area, which is a small localized area of the wing, and a geometrically exact one-dimensional displacement-based finite element model for the undamaged part of the wing. The solid and the beam parts are then rigorously combined using a transformation between the joined nodes of the two models at their intersection. The transformation is derived using the recovery equations of variational asymptotic beam model and employed to eliminate the six degrees of freedom of the single joined node of the beam. The validity and efficiency of the method is demonstrated using test cases involving cracks and delaminations in the solid part. It is shown that although the accuracy remains virtually the same between the full three-dimensional model and the joined one-dimensional/three-dimensional model, the computational cost is considerably lower for the latter. Finite-state induced flow theory of Peters is exploited as the unsteady aerodynamic model to compute aerodynamic forces and moments acting on the wing. Combining the structural and aerodynamic models, a dynamic nonlinear aeroelastic element is developed for the time simulation of the dynamic responses of composite high aspect-ratio wings. The model has been used for analyzing aeroelastic instability boundaries and time simulations, as well as synthesizing an active flutter suppression control system. Numerical results verifying the validity of the method are presented and the results are discussed.

The proposed joined model will enables the High-Altitude-Long-Endurance aircraft designers to tackle the problem of aeroelasticity in a computationally efficient manner, without sacrificing accuracy with regard to full three-dimensional models, hence reducing the overall time and cost of the design process.

CHAPTER I
INTRODUCTION

1.1 Motivation

There has been much interest in the aerospace community of late in High-Altitude-Long-Endurance (HALE) aircrafts. Many designs have been proposed for various HALE missions, but most feature very high aspect-ratio ($\mathcal{AR}$) wings. The design problem for high $\mathcal{AR}$ aircraft wings constructed from fiber-reinforced composite materials is a complex one. The high $\mathcal{AR}$ of the wing combined with stringent mass requirements has led to some highly flexible wing designs despite the superior specific stiffness properties of composites (compared with metallics). The large degree of flexibility in the wing leads to a strong coupling between the wing structural and aerodynamic performance. Nonlinear aeroelastic performance issues such as static load distribution, loss of control surface effectiveness, transient response and flutter are thus vitally important aspects of the performance of the vehicle. Structural failure can occur due to extreme loading, the encounter of an extreme gust, excursions beyond the flutter boundary, or over time due to the existence and growth of defects and/or cracks. The low temperatures at the extreme service altitude for this class of aircraft give rise to significant inter-laminar stresses as well as reduced damage tolerance in the wing.

The structural design of composite HALE aircraft wings is therefore often subject to stiffness requirements coming from static and dynamic aeroelastic performance in addition to commonly imposed stress-based failure and structural stability criteria (such as skin buckling). However, the existence of cracks in the structure due to a manufacturing defect and/or fatigue loading will degrade the structural performance of the wing, impacting (negatively in most cases) the aeroelastic and buckling performance

of the wing and creating stress concentrations. The fatigue loading of the wing results from transient structural vibrations due to maneuvers or gusts below the flutter speed and Limit-Cycle Oscillations (LCO) resulting from nonlinear aeroelastic behavior. Composite HALE designs that do not account for the progressive failure performance of the wing could be subject to sudden failure if aeroelastic instabilities or poorly damped transient behaviors are incurred as a result of minor damage to the wing. A progressive failure analysis for HALE aircraft would hence require consideration of the damage tolerance or growth rate of cracks, the possibility of skin buckling or other structural stability issues arising due to the degraded performance, and nonlinear aeroelastic behavior to capture the altered fatigue loading conditions. Environmental conditions commonly encountered by the aircraft should be accurately modeled.

Very efficient and yet high-fidelity aeroelastic analysis capability for HALE aircraft is possible by recognizing that two of the wing dimensions (chord and thickness) are quite small when compared with the third (span), allowing for the dimensional reduction of the Three-Dimensional (3D) structural analysis into a Two-Dimensional (2D) section analysis and a One-Dimensional (1D) beam analysis. For the 2D analysis, the computer code Variational Asymptotic Beam Section (VABS) [1, 2] implements the Variational Asymptotic Method (VAM) to calculate equivalent section constitutive properties for wing cross-sections, including those made of complex composite structure. These section properties can then be utilized in a 1D beam analysis to solve for the aeroelastic trim state as well as calculate the in-flight structural vibrations of the wing due to maneuvers or gusts.

However, the ability of a reduced-dimensional analysis tool such as VABS to analyze damage geometries that are essentially 3D, or to capture 3D stress field perturbations, may be questionable. It has been shown that for complex structures that are "beam-like" in some areas but not in others, it is possible to conduct a dimensionally reduced analysis over the "beam-like" portion and 3D Finite Elements Analysis (FEA) over the

remainder as long as stress and displacement continuity conditions are enforced over the interface of the cross-section. Such an analysis methodology would retain much of the efficiency of the dimensionally reduced analysis while providing the accuracy of 3D FEA where it is necessary. This technique of using mixed-dimensional analysis would have the potential of accurately modeling the effects and growth of damage without resorting to a full 3D analysis everywhere along the wing.

The control system design for this class of aircraft requires consideration of the inherent nonlinearities present in a system with large deflections even in the presence of small strain. Certain types of damage could introduce further nonlinearity into the system in the stress-strain relationship. To demonstrate this type of nonlinearity, consider a crack that opens when the wing bends upwards and closes when the wing bends downward. When the crack is closed, loading can be transferred over the crack and the structure might behave as if the crack did not exist, but when the crack is open there can be no load transfer over the crack and the structure could behave as if the material there is not present. The section constitutive law as obtained by a section analysis tool such as VABS is a linear matrix relationship between the integrated forces and moments and the generalized strains and curvatures, but the presence of such a crack would introduce a nonlinear constitutive relationship. The performance of the controller in terms of the ability to perform maneuvers, mitigate transient vibrations due to maneuver or gust loading, and suppress flutter behavior will be affected by such a nonlinearity in the constitutive law. This issue is exacerbated because the presence, location, and severity of the damage is unknown during the control design process. Therefore, the control design must account for the possibility of such a damage growth and be able to continue to perform adequately even if the damage develops and fails to be undetected or occurs well before scheduled inspection and maintenance.

1.2 Background and Literature Review

1.2.1 Joined Modeling Scheme

Several researchers have developed and proposed different methods for tackling mixed dimensional Finite Element (FE) problems. However, they can be categorized in two main categories: transition elements and Multi-Point Constraints (MPC).

As one of the first approaches, Surana [3–6] has developed isoparametric transition elements for both thin-wall and solid sections. In a similar vein, Cofer and Will [7], Gümr and Schorderet [8], and Gümr and Kauten [9] have proposed various transition elements for connecting solid elements to beam or shell elements. Other authors have also contributed to the field, most notable among them are Dohrmann and Key [10], Dohrmann *et al.* [11], Garusi and Tralli [12], and Chavan and Wriggers [13]. Although transition elements can give good results for mixed dimensional analysis in terms of stress and frequency, their use is limited to geometrically simple cross-sections with simple constitutive properties and, thus, they are not suitable for analyzing composite HALE wings with complicated cross-sectional topologies made of anisotropic materials.

MPC are popular for mixed dimensional analysis which, compared with transition elements, are simpler to implement and, due to growing computational power of computers, are being increasingly used in FEA. They are powerful methods, capable of dealing with both linear and nonlinear constraints between nodes. Among pioneering authors on the subject, Curiskis and Valliappan [14] have presented a solution algorithm for linear constraint equations in FEA. Abel and Shephard [15] have also proposed an algorithm for MPC in FEA. Their methods are convenient especially when the number of constraints is not very large. Shephard [16] has devised a procedure which employs the transformation approach for constraint application, thereby reducing the number of equations to be solved by the number of constraints. In a series of papers, NASA Langley Research Center has developed and published a method for

analyzing structures composed of two or more independently modeled substructures, based on a hybrid variational formulation with Lagrange multipliers, and applied it to global/local problems for 1D and 2D interfaces [17–21].

Most methods discussed so far, have been used for solid to shell coupling. However, a few authors have addressed the problem of solid to beam coupling. Among them Monaghan *et al.* [22] have obtained MPC between beam and solid elements by equating the work done by the stresses in each part of the model at the interface. Then McCune *et al.* [23] extended the method for shell to solid coupling. Shim *et al.* [24] have employed the method for some test cases. Avdeev *et al.* [25] have presented a formulation for 1D/2D coupling in sandwich beam structures based on a penalty function method. However, the methods are only applicable to problems with simple cross-sections and none of them considered composite beams as a possible test case.

As an alternative approach, Song and Hodges [26] have proposed a transformation matrix between the beam degrees of freedom and the solid degrees of freedom at the intersection, in such a way that all the nodal degrees of freedom of the solid part at the interface are constrained by the nodal degrees of freedom of the beam portion at the intersection. Information about the deflections, stresses, and strains at the intersection is available from the cross-sectional analysis, particularly from VABS. Therefore, the idea is to use that information to find the transformation matrix. Then dimensionally reduced analysis methods as VAM can be implemented for the beam-like parts and full 3D FEA can be used when needed, such as near the boundaries or around the areas with sharp geometric nonlinearities. Continuity conditions at the joined sections should be enforced using transformations from the interface between the 3D part and asymptotic beam theory. However, the standalone application written in FORTRAN90 lacks the generality and flexibility required by FEA. Moreover, it has not been developed for composite beams [27].

1.2.2 Nonlinear Aeroelasticity of HALE aircrafts

Over the years, the problem of aeroelasticity of both conventional [28–32] and composite and non-conventional aircrafts [33–37] has been the subject of numerous studies. Excellent and extensive reviews on aircraft aeroelasticity can be found in Refs. [38–41]. Aeroelasticity of high $\mathcal{AR}$ wings in general, and HALE aircrafts specifically, has been studied by many researchers. An experimental and theoretical study on aeroelastic response of high $\mathcal{AR}$ wings was carried out by Tang and Dowell [42]. An experimental high $\mathcal{AR}$ wing aeroelastic model with a slender body at the tip along with a theoretical model based on nonlinear beam theory and the ONERA aerodynamic stall model [43] has been constructed, and the response due to flutter and LCO has been measured in a wind-tunnel test. The theoretical dynamic flutter boundary is determined by a dynamic perturbation analysis about a static equilibrium. Using the same theoretical model, Tang and Dowell [44] has also studied the effects of geometric structural nonlinearity on flutter and LCO of high $\mathcal{AR}$ wings. They have shown the importance of the geometric structural nonlinearity effects of the beam theory on both the perturbation flutter boundary and the nonlinear response. Patil, Hodges, and Cesnik [45, 46] have studied nonlinear aeroelasticity of HALE aircrafts. They have shown the importance of taking into account the effects of nonlinear flexibility in the calculation of trim and flight dynamics characteristics. It is shown that the aeroelastic behavior of the complete aircraft may be drastically different from what it would be without such considerations. Patil and Hodges [47, 48] have demonstrate the need of nonlinear analysis to capture the aeroelastic behavior of HALE aircrafts and linear aeroelasticity may result to a misleading analysis. In order to show the significance of structural geometric nonlinearities and dynamic stall on the aeroelastic response of HALE aircrafts, Jian and Jinwu [49] have developed a first order state-space model for nonlinear aeroelastic analysis of high $\mathcal{AR}$ flexible wings using the fully intrinsic nonlinear composite beam model of Hodges [1, 50] and the

ONERA aerodynamic stall model. Through numerical simulations, it was shown that while at the lower flight speeds the geometric stiffness could lead to the LCO, by increasing the flight speed the effects of dynamic stall become more important in determining the onset and amplitude of flutter and LCO. Two different formulations for aeroelastic coupling of geometrically nonlinear structures and linear unsteady aerodynamics have been presented by Demasi and Livne [51]. The calculation of time domain integrals is necessary for the first method, whereas the second method converts unsteady aerodynamic time domain equations to second-order and couples them directly with the second-order structural equations without the need to compute time-domain convolution integrals. In order to provide an improved understanding of nonlinear phenomena occurring in the neighborhood of the flutter boundary and beyond, Arena *et al.* [52] have discussed the nonlinear aeroelastic modeling and the post-flutter behavior of HALE wings. The focus is on the post-flutter condition past the Hopf bifurcation when the effects of unsteady aerodynamics and dynamic stall on the dynamic behavior of the wing are more profound. Various effects of engine, including its thrust, on aeroelastic behavior of high $\mathcal{AR}$ flying wings have been studied by Mardanpour and his coworkers [53–56]. The fully intrinsic nonlinear composite beam model of Hodges is coupled with Peters' unsteady aerodynamic theory [57] to form the nonlinear aeroelastic system under consideration. Castellani *et al.* [58] have developed two methods based on nonlinear FEM and multibody dynamics for the nonlinear aeroelastic analysis of high $\mathcal{AR}$ wings and shown significant differences between linear and nonlinear analysis.

Previously cited research works have all assumed an undamaged structure for aeroelastic analysis and simulations. However, a number of authors have contributed to the theoretical and experimental aeroelastic study of damaged wings [59–62]. In an attempt to assess the aerodynamic effects of combat damage on wings and tails, Spearman [63] conducted a series of wind-tunnel tests at the NASA Langley Research

Center. The results show that the major damage to the vertical tail may lead to the loss of the aircraft at any speed. This is not the case, however, for the wing and horizontal tail which is counter-intuitive. Some authors have sought probabilistic and nondeterministic approaches, regarding damages as structural uncertainty [64–71]. On the other hand, other researchers have resorted to analytical and deterministic approaches for dealing with damage modeling and analysis. Among them, Kapania and Castel [72] have presented a 1D FE for aeroelastic analysis of undamaged and damaged wings, considering the effects of transverse shear as well as bending-stretching coupling which allows for unsymmetric laminations and arbitrary geometry. Through simulation, it is shown that unsymmetry due to damage can have a harmful effect because the extensional, bending, and bending-extension stiffness will decrease simultaneously. The model, however, may not properly account for the stress distribution and load transfer mechanisms in the damaged structure. Zhang [73], Douxchamps [74], and Bauchau *et al.* [75] have studied the nonlinear aeroelastic effects of matrix microcracking in damaged composite aerospace structures. They have shown that although the aeroelastic response of a damaged wing is qualitatively similar to that of an undamaged wing, matrix microcracking can result in oscillations with considerably higher amplitude. In a similar fashion, Kim, Atluri, and Loewy [76] have presented numerical methods to investigate the flutter response and aeroelastic stability of composite plates with matrix microcracking. The coupled bending and torsional vibration of a fiber-reinforced composite cantilever with an edge surface crack is presented by Wang *et al.* [77]. Using the approach presented in Ref. [77], Wang and Inman [78] have studied crack-induced effects on aeroelasticity of an unswept composite wing. The edge crack was modeled using the local flexibility concept, while steady and quasi-steady aerodynamics are employed to compute aerodynamic loads. It was shown that although for most cases the existence of cracks can negatively affect the flutter speed, for some cases the crack may actually improve the flutter boundary. In order to better understand the effects

of damage, Conyers *et al.* [79, 80] have modeled a plate-like wing with a hole using Lagrange's equations and coupled it with an unsteady aerodynamics model based on the doublet lattice method. The flutter characteristics have been compared with wind tunnel test results, verifying the sufficiency of linear analysis. Dang, Kapania, and Patil [81] have presented an analytical modeling of cracked thin-walled beams under torsion derived using the principle of virtual work.

Reduced order flutter analysis has also gained traction in the aerospace community. In particular, Reduced Order Modeling (ROM) schemes based on Proper Orthogonal Decomposition (POD) have been proven successful for a variety of aeroelasticity problems. A review of the POD method and its utility for dynamical characterization and order reduction of mechanical systems is presented by Kerschen *et al.* [82]. Through numerical simulation of vibro-impact of a continuous beam and transient and frequency response of a truss structure, they have shown that the principal orthogonal mode found from the POD method can be considered as an alternative to linear mode shapes as well as to nonlinear normal modes, and they can provide reduced-order models that represent a good characterization of the dynamics. However, they believe that the method may not always work when the data set lies on a nonlinear manifold, due to the linear nature of the method. Thomas *et al.* [83] and Hall *et al.* [84] have used POD for ROM and aeroelasticity analysis in the transonic regimes for a typical 2D wing section. In both references, small-disturbance unsteady aerodynamics was considered where the complex valued flow snapshots were calculated, at a few discrete frequencies, by solving the 2D Euler equations in frequency domain. The ROM was then formed from the snapshots and POD, coupled with a 2-DOF structural model of an airfoil. Although the full model has thousands of DOF, the aeroelastic stability was efficiently and accurately enough determined by solving a generalized eigenvalue problem using only twenty or fewer aerodynamic states. Lieu and Lesoinne [85] have used a POD-based ROM for three-dimensional flutter analysis at low free-stream Mach numbers

outside the transonic regime. They have specifically studied the robustness of the ROM with respect to varying free-stream Mach number, proposed a Mach-adaptation strategy, and compared the results with the full model. They have shown that the POD-based ROM is sensitive to Mach number. The aeroelastic problem has been formulated as a two-field, arbitrary Lagrangian-Eulerian finite element-finite volume system of equations. Instead of solving an eigenvalue problem for studying the stability of the linearized, reduced-order, coupled system of fluid-structure equations, they have considered the time histories of the lift as the output of the system, noting that the time histories of the lift with increasing amplitude indicates a dynamic flutter condition. POD and the method of snapshots in time have been used to find the reduced bases for the fluid system at different Mach numbers, and then two methods of interpolation of the bases were considered to find the reduced bases at intermediate Mach numbers: a Lagranges interpolation formula and the subspace angle method. While the latter was shown to be a good representation of the full model at intermediate Mach numbers, the former fails to give an acceptable approximation. The approach proposed in [85] was used by Lieu *et al.* [86] for aeroelastic modeling of a complete F-16 fighter aircraft at the transonic regime. The results show good agreement between the flutter boundaries found from the ROM method and those predicted by a full-order nonlinear CFD based aeroelastic analysis, while the computations were performed five times faster. A method based on the interpolation in a tangent space to the Grassmann manifold was developed by Amsallem *et al.* for use in CFD based applications [87, 88]. Exploiting the symmetric positive definite nature of linear structural models, they have devised an algorithm to first map the ROM onto a tangent space to the manifold, then interpolate the projected ROM in the tangent space and finally map them back to the underlying manifold. It was shown the interpolation procedure preserves the structure of the manifold.

1.2.3 Flutter Suppression

Flutter, left unchecked, can lead to catastrophic failure of the aircraft. Therefore, designing passive and active control systems to either delay or suppress the flutter is of utmost importance.

The large number of DOF arising from FEM discretization of structural models make the Full Order Model (FOM) impractical for controller design. The issue begs for a Reduced Order Model (ROM) derived from the FOM. Due to its simplicity, many references have used a 2D typical section as the representative and applied various linear and nonlinear controllers [89–92].

Linear Quadratic Regulation (LQR) has also been used extensively for flutter suppression and maneuver control of aeroelastic aircrafts [93–95]. Karpel [96] has presented an analytical design technique for active flutter suppression and gust alleviation using state-space aeroelastic modeling. The controller gains are constant and only some states are used as feedback. LQR and Linear Quadratic Gaussian (LQG) control laws have been used as the control laws for the flutter suppression of typical sections by Block and Strganac [97] and Frampton and Clark [98], respectively. Structured Model Reference Adaptive Control (SMRAC) for a wing section with structural nonlinearity has been presented by Ko *et al.* [99]. The control system enjoys the benefit of being able to suppress LCO at higher flight velocity and to effectively deal with the actuator saturation. Behal *et al.* [100] have also designed an output feedback nonlinear adaptive controller to suppress the LCO in an aeroelastic 2D wing section. Stability is guaranteed in the presence of inaccurate system parameters. Lee and Singh [101] have designed a robust output feedback controller for a 2D section with pitch nonlinearity. Wei and Mottershead [102] have designed a robust passivity based continuous sliding mode control for an under-actuated 2D wing section with torsional nonlinearity. Numerical simulations verify the local stability of the controller. A robust nonlinear sliding mode controller which uses leading and trailing edge flaps

as the control surfaces is presented by Ghorawat *et al.* [103] for stabilization of LCO of a nonlinear 2D wing section. This objective is achieved in the presence of gust loads and parameters uncertainty.

A number of other authors, however, have used continuum structural FOM and from that extracted a ROM of the structure [104–106]. Patil and Hodges [93, 107] have designed an optimal output feedback control for the flutter suppression and gust load alleviation of a nonlinear aeroelastic HALE aircraft. An *ad hoc* ROM is constructed from the nonlinear model of HALE aircraft and sensor outputs are used directly. It is shown that the performance and robustness of the controller is comparable to both LQR and LQG controllers. A similar approach has been employed by Richards [108]. Based on a ROM of a very flexible aircraft developed in Ref. [109], Sheare and Cesnik [110] have designed a nonlinear trajectory controller for the aircraft. The overal controller consists of an inner loop with LQR and dynamic inversion control laws and an outer loop that handles kinematic nonlinearities. Raghavan and Patil [111–113] have coupled a multistep nonlinear dynamic inversion controller based on a ROM, with a nonlinear guidance law to design a flight controller for path following mission of high $\mathcal{AR}$ flying wings. Addressing the need for a fast and reliable ROM procedure capable of being used in on-line and real-time simulation and controls applications, Amsallem *et al.* [114] have proposed a numerical algorithm for interpolating structural dynamics ROM built upon the method established in Refs. [87, 88]. The performance of the algorithm was evaluated through two numerical examples: a discrete multiple mass-spring-damper system and a tapered, backward-swept cantilevered wing. A modification of the interpolation method in [114] has been used by Amsallem and Farhat [115] for online robust interpolation of linear parametric projection based ROM, in which a new linear ROM for a new set of parameters is constructed from the precomputed linear ROM. In contrast to [114], an additional step has been performed before the interpolation in which the precomputed ROM is transformed

into a consistent set of generalized coordinates through a congruence transformation resulting from analytical solution of a minimization problem. This step is performed off-line. The second step is the same as the interpolation in [114] which is carried out on-line. It was demonstrated that the method is robust enough in dealing with cases in which the set of the sampled parameters leads to a mode veering phenomenon. It is known that, in general, the stability of the ROM derived from an FOM is not guaranteed even if the FOM itself is stable [116]. A method for stabilization of a projection-based ROM is proposed by Amsallem and Farhat [117]. The method is basically fixes the right Reduced Order Bases (ROB) and solves a convex optimization problem that searches for the left ROB in the already available reduced space. The operations are not performed directly on the ROB themselves, therefore, it can be considered as a post-processing step independent of the method of finding the ROM, preserving its accuracy.

1.3 Present Work

To add to the aforementioned bulk of literature, this thesis will focus on aeroservoelastic analysis of damaged high $\mathcal{AR}$ wings. When there exist no damage or geometrical nonlinearites in the structure of a HALE aircraft wing, it can be rigorously modeled as a 1D beam. However, it is not the case in the presence of damage or geometric nonlinearities. In such a situation, on the one hand, 1D beam models fail to provide a viable framework for damage analysis. On the other hand, studying the effects of damage on aeroelastic behavior of wings using full 3D FEM, requires a detailed CFD/CSD analysis. Such an analysis is a computationally intensive task which requires lots of processing power. For the case of a damaged HALE aircraft wing, one is essentially dealing with a structure which for the most part can be properly modeled as a reduced-dimensional beam. However, small areas need to be regarded as a 3D continuum. Thus, a mixed-dimensional modeling approach appears to be of a

great value. Therefore, in this research a computationally economical approach for dealing with the problem of aeroservoelasticity of damaged HALE aircraft wings will be proposed. To this end, it suggests and investigates a mixed-dimensional analysis technique in which most of the structure of a damaged high $\mathcal{AR}$ wing is modeled as 1D beam, and the small areas around the damage are regarded as full 3D. This way one can benefit from the computational efficiency of dimensionally reduced analysis, while preserving the accuracy of full 3D FEA where it is necessary. A transformation between the 1D and 3D parts of the model is necessary, in order to enforce continuity conditions at the joined interface. The approach also allows aeroelasticity modeling using beam theory, avoiding 3D CFD analysis. This way, stability analysis as well as nonlinear time-simulation would become possible at a fraction of computational cost of a CFD/CSD analysis. Moreover, it will equip the control system designer with a computationally efficient, yet numerically accurate, tool for designing and evaluating active flutter suppression systems. The approach is specially beneficial at the early stages of airframe design and analysis.

The rest of the dissertation is organized as follows:

Chapter II details the methodology and modeling approach for a joined 3D/1D FE analysis of damaged HALE aircraft wings. A geometrically exact displacement-based beam model, which is adopted for the 1D part of the structure, is formulated. Then, unsteady aerodynamic forces and moments are integrated with the 1D beam model to provide a nonlinear aeroelastic element. The transformation matrix between the nodal DOF of the 1D and 3D parts at the joined intersection is derived using the recovery equations of the variational asymptotic method. Also, POD and method of snapshot is introduced to find a ROM of the joined 3D/1D model. This chapter is, then, concluded by the formulation of an active flutter suppression system in LQR/LQG framework.

Chapter III is entirely designated to showing the validity of various analyses performed using the joined 3D/1D model. A layered composite beam, clamped at one

end and loaded by a transverse load at the other end, is considered as a test case. First static stress analysis and eigenanalysis are studied for an undamaged structure. Subsequently, different damage scenarios for that structure are investigated. For all test cases, the results are compared and contrasted with full 3D FEA.

Chapter IV will present aeroelastic analysis of a high $\mathcal{AR}$ composite wing using the joined 3D/1D approach. Through linear aeroelastic stability analysis, divergence and flutter boundaries of the wing are determined for different composite layup arrangements and various damage scenarios. Nonlinear analysis is, then, followed and effects of large deformations are investigated on the aeroelastic behavior of the wing. Also, LCO are studied using time-integration of nonlinear equations of motion, and effects of damage on LCO characteristics are highlighted.

Chapter V will detail a flutter suppression control system. POD and method of snapshots are exploited to extract a ROM of the joined 3D/1D model, to be used as a surrogate model for the controller design. This will be followed by describing the control system, which is designed using LQR/LQG. Performance and robustness of the controller, in the presence of damage and loss of control power, are assessed through nonlinear time-simulations. Also, effects of sensor/actuator non-collocation on the performance of the controller will be discussed.

Chapter VI, finally, will summarize the findings of the research, and some topics for future work are suggested.

CHAPTER II

THEORY

2.1 Introduction

Performance requirements of HALE aircrafts drive designers towards very slender high $\mathcal{AR}$ wings to decrease the induced drag, and extensive use of light weight composite materials to reduce overall weight. The wings therefore undergo geometrically nonlinear behavior such as large deflections and rotation. Since HALE aircraft wings are very slender, they can properly be modeled as beam structures. A beam model for HALE aircraft wings, therefore, must account for large deformations. On the other hand, damage is a 3D phenomenon which cannot be properly modeled in a 1D framework. Therefore, for the joined 3D/1D fininte element analysis proposed in this thesis, the damage is fully contained in a relatively small 3D continuum part of the structure. Most of the structure, however, is modeled as a 1D beam. The continuity conditions between 1D and 3D part is derived and enforced at the interface. For the purpose of joined 3D/1D finite elements analysis of damaged HALE aircraft wings, a geometrically exact displacement based FEM 1D beam model is desired. The model also provides a compatible framework with the 3D continuum part of the wing. To this end, a geometrically exact beam model developed by Bauchau [118] is being used for the 1D part. For the 3D part standard continuum elements of Abaqus are being exploited.

To enforce the continuity conditions at the interface between 1D and 3D parts, variational asymptotic method is used to derive the transformation between the joined elements.

Aerodynamic forces and moments are applied to the flexible wing, and hence, deform the structure. The resulting deformations alter the aerodynamic loads. Therefore,

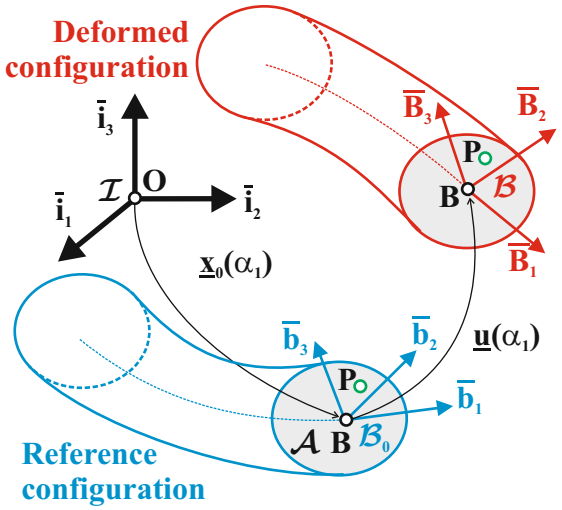

Figure 2.1: Moving beam in an inertial reference frame [119]

the structural and aerodynamic problems are essentially coupled and the interactions need to be accounted. Finite-state induced flow theory of Peters *et al.* [57] is exploited as the unsteady aerodynamic model to compute aerodynamic forces and moments acting on the wing.

2.2 A Geometrically Exact Beam Model

A displacement-based geometrically exact FE beam model, developed by Bauchau [118], is adopted and the formulation is presented in this section. More details can be found in [118].

An initially curved and twisted beam moving in an inertial reference frame $\mathcal{I}$ is shown in Fig. 2.1. An orthogonal basis, $\mathcal{B}_0(\alpha_1) = \left(\bar{b}_1, \bar{b}_2, \bar{b}_3\right)$, is attached to the point **B** located at the intersection of the refernce line with the plane of the cross section of the beam. α_1 is the curvilinear coordinate measuring the length along the beam's reference line. The beam can undergo large deformations, however, the strain remains small. The position vector of **B** is denoted as $\underline{x}_0(\alpha_1)$, and the position vector of a material point **P** of the beam is expressed as

$$\underline{x}\,(\alpha_1, \alpha_2, \alpha_3) = \underline{x}_0\,(\alpha_1) + \alpha_2\,\overline{b}_2 + \alpha_3\,\overline{b}_3, \tag{2.1}$$

where α_2 and α_3 are the material coordinates along unit vectors $\overline{b}_2$ and $\overline{b}_3$, respectively. The position vector of $\mathbf{P}$ in the deformed configuration can be written as

$$\underline{X}\,(\alpha_1, \alpha_2, \alpha_3) = \underline{X}_0 + w_1\overline{B}_1 + (w_2 + \alpha_2)\,\overline{B}_2 + (w_3 + \alpha_3)\,\overline{B}_3, \tag{2.2}$$

where the position of point $\mathbf{B}$ can be expressed as the sum of the initial position $\underline{x}_0(\alpha_1)$ and the displacement vector $\underline{u}\,(\alpha_1)$ as $\underline{X}_0\,(\alpha_1) = \underline{x}_0 + \underline{u}$. The orthonormal basis $\mathcal{B}(\alpha_1) = (\overline{B}_1, \overline{B}_2, \overline{B}_3)$ is attached to the point $\mathbf{B}$ in the deformed configuration. The samll warping field is expressed in the deformed configuration as $\underline{w}(\alpha_1, \alpha_2, \alpha_3) = w_1\overline{B}_1 + w_2\overline{B}_2 + w_3\overline{B}_3$.

The components of the rotation tensor that brings the reference frame $\mathcal{I}$ to the frame $\mathcal{B}_0$, expressed in basis $\mathcal{I}$, are denoted as $\underline{\underline{R}}_0\,(\alpha_1)$, and the components of the rotation tensor that brings the basis $\mathcal{B}_0$ to the frame $\mathcal{B}$, expressed in basis $\mathcal{I}$, are denoted as $\underline{\underline{R}}(\alpha_1)$. Since $\overline{B}_i = \underline{\underline{R}}\,\overline{b}_i = (\underline{\underline{R}}\,\underline{\underline{R}}_0)\,\overline{i}_i$, Eq. (2.2) can be rewritten as

$$\underline{X}(\alpha_1, \alpha_2, \alpha_3) = \underline{x}_0 + \underline{u} + (\underline{\underline{R}}\,\underline{\underline{R}}_0)(w_3 + \alpha_2\,\overline{i}_2 + \alpha_3\,\overline{i}_3). \tag{2.3}$$

Having the position vector defined, the inertial velocity vector of the point $\mathbf{P}$, ignoring the contribution from the warping field, can be found by taking the time derivative of the position vector in the inertial frame, $\mathcal{I}$, as

$$\begin{aligned} \underline{v} &= \dot{\underline{u}} + \dot{\underline{\underline{R}}}\,\underline{\underline{R}}_0\,\underline{s}^* \\ &= \dot{\underline{u}} + \underline{\underline{R}}\,\underline{\underline{R}}_0\,\widetilde{\omega}^*\underline{s}^* \\ &= \dot{\underline{u}} + \underline{\underline{R}}\,\underline{\underline{R}}_0\,\widetilde{s}^{*T}\underline{\omega}^*. \end{aligned} \tag{2.4}$$

Here, $\underline{\omega^*}$ is the angular velocity vector expressed in $\mathcal{B}$ farme, and $\dot{(\cdot)}$ denotes differen-

tiation with respect to time. Thus

$$\begin{aligned} \underline{v}^* &= (\underline{\underline{R}}\,\underline{\underline{R}}_0)^T \underline{v} \\ &= (\underline{\underline{R}}\,\underline{\underline{R}}_0)^T \dot{\underline{u}} + \widetilde{s}^{*T} \underline{\omega}^*. \end{aligned} \tag{2.5}$$

The sectional strain measures are defined as

$$\underline{e} = \left\{ \begin{array}{c} \underline{\epsilon} \\ \underline{\kappa} \end{array} \right\} = \left\{ \begin{array}{c} \underline{x}_0' + \underline{u}' - (\underline{\underline{R}}\,\underline{\underline{R}}_0)\,\bar{i}_1 \\ \underline{k} + \underline{\underline{R}}\,\underline{k}_i \end{array} \right\}, \tag{2.6}$$

where $\underline{k} = \text{axial}\left(\underline{\underline{R}}'\underline{\underline{R}}^T\right)$ is the sectional curvature vector expressed in $\mathcal{I}$ and $(\cdot)'$ denotes derivative with respect to α_1. The strain measures, consisting of axial and shear strains, are expressed in the deformed basis, $\mathcal{B}$, as $\underline{\epsilon}^* = (\underline{\underline{R}}\,\underline{\underline{R}}_0)^T \underline{\epsilon}$. The curvature components, consisting of twist and bending curvatures, are expressed in the deformed beam basis, $\mathcal{B}$, as $\underline{\kappa}^* = (\underline{\underline{R}}\,\underline{\underline{R}}_0)^T \underline{\kappa}$. For all tensors, the notation $(\cdot)^*$ denotes that the components of the tensor are expressed in the deformed basis, $\mathcal{B}$.

Cross sectional forces, $\underline{N}^*$, and moments, $\underline{M}^*$, are related to the generalized strain measures through the sectional constitutive law as

$$\left\{ \begin{array}{c} \underline{N}^* \\ \underline{M}^* \end{array} \right\} = \underline{\underline{\mathcal{C}}}^* \left\{ \begin{array}{c} \underline{\epsilon}^* \\ \underline{\kappa}^* \end{array} \right\}, \tag{2.7}$$

where $\underline{\underline{\mathcal{C}}}^*$ is the 6×6 sectional stiffness matrix which can be found from VABS. Potential energy, $\mathcal{U}$, consisting of strain energy of the beam can be expressed as

$$U = \frac{1}{2} \int_0^L \underline{e}^{*T} \underline{\underline{\mathcal{C}}}^* \underline{e}^* \, \mathrm{d}\alpha_1. \tag{2.8}$$

Using Eq. (2.5), the kinetic energy of the beam, K, is defined by the expression

$$\begin{aligned} K &= \frac{1}{2}\int_0^L \int_{\mathcal{A}} \rho\, \underline{v}^{*T}\underline{v}^*\, \mathrm{d}\mathcal{A}\, \mathrm{d}\alpha_1 \\ &= \frac{1}{2}\int_0^L \int_{\mathcal{A}} \rho\, \left[\underline{\dot{u}}^T(\underline{\underline{R}}\,\underline{\underline{R}}_0) + \underline{\omega}^{*T}\widetilde{s}^*\right]\left[(\underline{\underline{R}}\,\underline{\underline{R}}_0)^T\underline{\dot{u}} + \widetilde{s}^{*T}\underline{\omega}^*\right] \mathrm{d}\mathcal{A}\, \mathrm{d}\alpha_1. \end{aligned} \tag{2.9}$$

Integration over the cross section, $\mathcal{A}$, can be carried out to define the constant sectional inertia properties as

$$\begin{aligned} m &= \int_{\mathcal{A}} \rho\, \mathrm{d}\mathcal{A}, \\ \underline{\eta}^* &= \frac{1}{m}\int_{\mathcal{A}} \rho\, \underline{s}^*\, \mathrm{d}\mathcal{A}, \\ \underline{\underline{\varrho}}^* &= \frac{1}{m}\int_{\mathcal{A}} \rho\, \widetilde{s}^*\widetilde{s}^{*T}\, \mathrm{d}\mathcal{A}, \end{aligned} \tag{2.10}$$

where m is the mass per unit length of the beam, $\underline{\eta}^*$ is the mass center position of the section, and $\underline{\underline{\varrho}}^*$ is the sectional inertial tensor per unit length of the beam. The kinetic energy, therefore, can be expressed as

$$\begin{aligned} K &= \frac{1}{2}\int_0^L \left[m\underline{\dot{u}}^T\underline{\dot{u}} + 2m\underline{\dot{u}}^T\,(\underline{\underline{R}}\,\underline{\underline{R}}_0)\,\widetilde{\eta}^{*T}\underline{\omega}^* + \underline{\omega}^{*T}\underline{\underline{\varrho}}^*\underline{\omega}^*\right]\, \mathrm{d}\alpha_1 \\ &= \frac{1}{2}\int_0^L \int_{\mathcal{A}} \underline{\mathcal{V}}^{*T}\underline{\underline{\mathcal{M}}}^*\underline{\mathcal{V}}^*\, \mathrm{d}\alpha_1, \end{aligned} \tag{2.11}$$

where $\underline{\underline{\mathcal{M}}}^*$ is the 6×6 inertia matrix arranged as

$$\underline{\underline{\mathcal{M}}}^* = \begin{bmatrix} m\,\underline{\underline{I}} & m\,\widetilde{\eta}^{*T} \\ m\,\widetilde{\eta}^* & \underline{\underline{\varrho}}^* \end{bmatrix}, \tag{2.12}$$

and the velocities are cast into the vector $\underline{\mathcal{V}}^*$ as

$$\begin{aligned}\underline{\mathcal{V}}^* &= \begin{bmatrix} (\underline{\underline{R}}\,\underline{\underline{R}}_0) & \underline{\underline{0}} \\ \underline{\underline{0}} & (\underline{\underline{R}}\,\underline{\underline{R}}_0) \end{bmatrix} \begin{Bmatrix} \underline{\dot{u}} \\ \underline{\omega} \end{Bmatrix} \\ &= (\underline{\underline{\mathcal{R}}}\,\underline{\underline{\mathcal{R}}}_0)^T \underline{\mathcal{V}}.\end{aligned} \tag{2.13}$$

In Eq. (2.13), the inertial velocities of the cross section are defined as $\underline{\mathcal{V}}^T = \{\underline{u}^T, \underline{\omega}^T\}$. Therefore, if the sectional linear and angular momenta expressed in $\mathcal{B}$ are denoted as $\underline{h}^*$ and $\underline{g}^*$, respectively, then it can be said that

$$\underline{\mathcal{P}}^* = \begin{Bmatrix} \underline{h}^* \\ \underline{g}^* \end{Bmatrix} = \underline{\underline{\mathcal{M}}}^* \underline{\mathcal{V}}^*. \tag{2.14}$$

Having the kinetic and potential energies for the beam defined, the governing equations of a beam can be found from Hamilton's extended principle, which can be written as

$$\int_{t_1}^{t_2} \int_0^L \left[\delta(K - U) + \overline{\delta \mathcal{W}}\right] \mathrm{d}t \, \mathrm{d}\alpha_1, \tag{2.15}$$

where δ and $\overline{\delta \mathcal{W}}$ are the Lagrangian variation operator and the virtual work density of externally applied loads, respectively. Using Eq. (2.8), the variation of the potential energy can be found as

$$\delta U = \int_0^L \left(\delta \underline{\epsilon}^{*T} \underline{N}^* + \delta \underline{\kappa}^{*T} \underline{M}^*\right) \mathrm{d}\alpha_1. \tag{2.16}$$

Variations of generalized strain measures can be found by use of Eq. (2.6) as

$$\begin{aligned}\delta \underline{\epsilon}^* &= (\underline{\underline{R}}\,\underline{\underline{R}}_0)^T \left[\delta \underline{u}' + (\widetilde{x}_0' + \widetilde{u}') \underline{\delta \psi}\right], \\ \delta \underline{\kappa}^* &= (\underline{\underline{R}}\,\underline{\underline{R}}_0)^T \underline{\delta \psi}',\end{aligned} \tag{2.17}$$

in which $\underline{\delta \psi} = \text{axial}(\delta \underline{\underline{R}}\,\underline{\underline{R}}^T)$ is the virtual rotation vector.

In a similar manner, variation of the kinetic energy, δK, can be found from

$$\delta K = \int_0^L \delta \underline{\mathcal{V}}^{*T} \underline{\underline{\mathcal{M}}}^* \underline{\mathcal{V}}^* \mathrm{d}\alpha_1. \tag{2.18}$$

Variations of the velocities can be expressed as

$$\begin{aligned} \delta \left[\underline{\dot{u}}^T (\underline{\underline{R}}\, \underline{\underline{R}}_0) \right] &= (\delta \underline{\dot{u}}^T + \underline{\delta\psi}^T\, \tilde{\dot{u}}^T)(\underline{\underline{R}}\, \underline{\underline{R}}_0), \\ \delta \underline{\omega}^{*T} &= \underline{\delta\dot{\psi}}^T (\underline{\underline{R}}\, \underline{\underline{R}}_0). \end{aligned} \tag{2.19}$$

The kinetic energy, therefore, can be expressed as

$$\int_0^L \left[(\delta \underline{\dot{u}}^T + \underline{\delta\psi}^T\, \tilde{\dot{u}}^T)(\underline{\underline{R}}\, \underline{\underline{R}}_0) \underline{h}^* + \underline{\delta\dot{\psi}}^T (\underline{\underline{R}}\, \underline{\underline{R}}_0) \underline{g}^* \right] \mathrm{d}\alpha_1. \tag{2.20}$$

By expressing the linear and angular momenta in the inertial reference frame, $\mathcal{I}$, using

$$\underline{\mathcal{P}} = \left\{ \begin{array}{c} \underline{h} \\ \underline{g} \end{array} \right\} = (\underline{\underline{\mathcal{R}}}\, \underline{\underline{\mathcal{R}}}_0) \underline{\mathcal{P}}^*, \tag{2.21}$$

the kinetic energy expression can be simplified as

$$\int_0^L \left[(\delta \underline{\dot{u}}^T + \underline{\delta\psi}^T\, \tilde{\dot{u}}^T) \underline{h} + \underline{\delta\dot{\psi}}^T\, \underline{g} \right] \mathrm{d}\alpha_1. \tag{2.22}$$

Putting Eqs. (2.16) and (2.22) back into Eq. (2.15), Hamilton's extended principle results in

$$\begin{aligned} \int_{t_1}^{t_2} \int_0^L [&(\delta \underline{\dot{u}}^T + \underline{\delta\psi}^T\, \tilde{\dot{u}}^T) \underline{h} + \underline{\delta\dot{\psi}}^T\, \underline{g} - (\delta \underline{u}'^T + \underline{\delta\psi}^T\, \widetilde{E}_1^T) \underline{N} \\ &- \underline{\delta\psi}'^T \underline{M} + \delta \underline{u}^T\, \underline{f} + \underline{\delta\psi}^T\, \underline{m}] \, \mathrm{d}t \, \mathrm{d}\alpha_1 = 0, \end{aligned} \tag{2.23}$$

where $\underline{f}$ and $\underline{m}$ are the externally applied forces and moments on the beam, respectively. Finally, upon integrating by parts, the governing equations of flexible beam can be

found as

$$\begin{aligned} \dot{\underline{h}} - \underline{N}' &= \underline{f}, \\ \dot{\underline{g}} + \dot{\widetilde{u}}\,\underline{h} - \underline{M}' - (\widetilde{x}_0' + \widetilde{u}')\underline{N} &= \underline{m}. \end{aligned} \tag{2.24}$$

Eqs. (2.24) are highly nonlinear and must be solved using the finite element method. The set of all forces acting on the beam can be identified as elastic, inertial, dissipative, and external forces. From Eqs. (2.24) the inertial forces, $\underline{\mathcal{F}}^I$, can be shown to have the form

$$\underline{\mathcal{F}}^I = \dot{\underline{\mathcal{P}}} + \begin{bmatrix} \underline{\underline{0}} & \underline{\underline{0}} \\ \dot{\widetilde{u}} & \underline{\underline{0}} \end{bmatrix} \underline{\mathcal{P}}, \tag{2.25}$$

which, upon expanding the terms, can be cast in a compact form as

$$\underline{\mathcal{F}}^I = \begin{Bmatrix} m\ddot{\underline{u}} + (\dot{\widetilde{\omega}} + \widetilde{\omega}\widetilde{\omega})m\underline{\eta} \\ m\widetilde{\eta}\ddot{\underline{u}} + \underline{\underline{\varrho}}\dot{\underline{\omega}} + \widetilde{\omega}\underline{\underline{\varrho}}\underline{\omega} \end{Bmatrix}, \tag{2.26}$$

which can be linearized as

$$\Delta\underline{\mathcal{F}}^I = \underline{\underline{K}} \begin{Bmatrix} \Delta\underline{u} \\ \Delta\underline{\psi} \end{Bmatrix} + \underline{\underline{G}} \begin{Bmatrix} \Delta\dot{\underline{u}} \\ \Delta\underline{\omega} \end{Bmatrix} + \underline{\underline{M}} \begin{Bmatrix} \Delta\ddot{\underline{u}} \\ \Delta\dot{\underline{\omega}} \end{Bmatrix}. \tag{2.27}$$

Rotation is parametrized using Wiener-Milenković parameters [118] such that

$$\begin{aligned} \underline{\omega} &= \underline{\underline{H}}(\underline{\theta})\,\dot{\underline{\theta}}, \\ \underline{\kappa} &= \underline{\underline{H}}(\underline{\theta})\,\underline{\theta}', \end{aligned} \tag{2.28}$$

where $\underline{\theta}$ is the rotation vector and $\underline{\underline{H}}$ is the tangent tensor defined in [118]. Using Wiener-Milenković parameters, the displacement and rotation variables are grouped in the vector $\underline{q}^T = \{\underline{u}^T, \underline{\theta}^T\}$. Therefore, the inertial forces can be shown with the

compact form

$$\Delta\underline{\mathcal{F}}^I = \underline{\underline{\mathcal{K}}}\,\Delta\underline{q} + \underline{\underline{\mathcal{G}}}\,\Delta\underline{\dot{q}} + \underline{\underline{\mathcal{M}}}\,\Delta\underline{\ddot{q}}. \tag{2.29}$$

The contribution of the elastic and dissipative forces, denoted as $\underline{\mathcal{F}}^C$ and $\underline{\mathcal{F}}^D$, are defined as

$$\begin{aligned} \underline{\mathcal{F}}^C &= \begin{Bmatrix} \underline{N} \\ \underline{M} \end{Bmatrix}, \\ \underline{\mathcal{F}}^D &= \begin{Bmatrix} \underline{0} \\ (\widetilde{u}_0' + \widetilde{u}')^T \underline{N} \end{Bmatrix}, \end{aligned} \tag{2.30}$$

with the linearized forms as

$$\begin{aligned} \Delta\underline{\mathcal{F}}^C &= \underline{\underline{\mathcal{S}}}\,\Delta\underline{q}' + \underline{\underline{\mathcal{O}}}\,\Delta\underline{q}, \\ \Delta\underline{\mathcal{F}}^D &= \underline{\underline{\mathcal{T}}}\,\Delta\underline{q}' + \underline{\underline{\mathcal{Q}}}\,\Delta\underline{q}. \end{aligned} \tag{2.31}$$

The reader is advised to consult Ref. [118] for detailed expressions for the matrices $\underline{\underline{\mathcal{K}}}$, $\underline{\underline{\mathcal{G}}}$, $\underline{\underline{\mathcal{M}}}$, $\underline{\underline{\mathcal{S}}}$, $\underline{\underline{\mathcal{O}}}$, $\underline{\underline{\mathcal{T}}}$, and $\underline{\underline{\mathcal{Q}}}$.

Having the inertial, elastic, and dissipative forces described by Eqs. (2.26) and (2.30), the governing equation, Eqs. (2.24), can be recast in a compact form as

$$\underline{\mathcal{F}}^I - \underline{\mathcal{F}}^{C'} + \underline{\mathcal{F}}^D - \underline{\mathcal{F}}^{\text{ext}} = 0, \tag{2.32}$$

which is a description of dynamic equilibrium of the beam. In Eq. (2.32), the parameter $\underline{\mathcal{F}}^{\text{ext}}$ represents the vector of external forces. In this thesis, the external force vector is comprised of aerodynamic and control forces and moments acting on the beam, to be defined in the next chapters. In order to obtain a finite element formulation of the beam, a weighted residual formulation is adopted here. The weak form of the

dynamic equilibrium equation can be described as

$$\int_0^L \underline{\underline{N}}^T(\underline{\mathcal{F}}^I - \underline{\mathcal{F}}^{C\prime} + \underline{\mathcal{F}}^D - \underline{\mathcal{F}}^{\text{ext}})\,\mathrm{d}\alpha_1 = 0, \tag{2.33}$$

where $\underline{\underline{N}}$ is the matrix of test functions. Integrating by parts on the second term yields

$$\int_0^L (\underline{\underline{N}}^T\underline{\mathcal{F}}^I + \underline{\underline{N}}'^T\underline{\mathcal{F}}^C + \underline{\underline{N}}^T\underline{\mathcal{F}}^D - \underline{\underline{N}}^T\underline{\mathcal{F}}^{\text{ext}})\,\mathrm{d}\alpha_1 = 0, \tag{2.34}$$

which can be linearized recalling Eqs. (2.29) and (2.31) as

$$\begin{aligned}\int_0^L [\underline{\underline{N}}^T(\underline{\mathcal{F}}^I + \underline{\underline{\mathcal{K}}}\,\Delta\underline{q} + \underline{\underline{\mathcal{G}}}\,\Delta\underline{v} + \underline{\underline{\mathcal{M}}}\,\Delta\underline{a} + \underline{\mathcal{F}}^D + \underline{\underline{\mathcal{T}}}\,\Delta\underline{q}' + \underline{\underline{\mathcal{Q}}}\,\Delta\underline{q} - \underline{\mathcal{F}}^{\text{ext}}) \\ + \underline{\underline{N}}'^T(\underline{\mathcal{F}}^C + \underline{\underline{\mathcal{S}}}\,\Delta\underline{q}' + \underline{\underline{\mathcal{O}}}\,\Delta\underline{q})]\,\mathrm{d}\alpha_1 = 0.\end{aligned} \tag{2.35}$$

The assumed shape functions are exploited to interpolate the elemental displacement, $\underline{q}$, velocity, $\underline{v}$, and acceleration, $\underline{a}$, variables in terms of their nodal values, $\underline{\hat{q}}$, $\underline{\hat{v}}$, and $\underline{\hat{a}}$, respectively, as

$$\begin{aligned}\underline{q}(\alpha_1) &= \underline{\underline{N}}\,\underline{\hat{q}},\ \underline{q}'(\alpha_1) = \underline{\underline{N}}'\,\underline{\hat{q}}, \\ \underline{v}(\alpha_1) &= \underline{\underline{N}}\,\underline{\hat{v}},\ \underline{a}(\alpha_1) = \underline{\underline{N}}\,\underline{\hat{a}}.\end{aligned} \tag{2.36}$$

Accordingly, the weak form of the dynamic equilibrium can be described as

$$\underline{\underline{\hat{M}}}\,\Delta\underline{\hat{a}} + \underline{\underline{\hat{G}}}\,\Delta\underline{\hat{v}} + \underline{\underline{\hat{K}}}\,\Delta\underline{\hat{q}} = \underline{\hat{F}}^{\text{ext}} - \underline{\hat{F}}, \tag{2.37}$$

where the elemental mass, $\hat{\underline{\underline{M}}}$, gyroscopic, $\hat{\underline{\underline{G}}}$, and stiffness, $\hat{\underline{\underline{K}}}$, matrices are found as

$$\hat{\underline{\underline{M}}} = \int_0^L \underline{\underline{N}}^T \underline{\underline{\mathcal{M}}}\, \underline{\underline{N}}\, \mathrm{d}\alpha_1, \tag{2.38a}$$

$$\hat{\underline{\underline{G}}} = \int_0^L \underline{\underline{N}}^T \underline{\underline{\mathcal{G}}}\, \underline{\underline{N}}\, \mathrm{d}\alpha_1, \tag{2.38b}$$

$$\hat{\underline{\underline{M}}} = \int_0^L [\underline{\underline{N}}^T (\underline{\underline{\mathcal{K}}} + \underline{\underline{\mathcal{Q}}})\, \underline{\underline{N}} + \underline{\underline{N}}^T \underline{\underline{\mathcal{T}}}\, \underline{\underline{N}}' + \underline{\underline{N}}'^T \underline{\underline{\mathcal{S}}}\, \underline{\underline{N}}' + \underline{\underline{N}}'^T \underline{\underline{\mathcal{O}}}\, \underline{\underline{N}}]\, \mathrm{d}\alpha_1, \tag{2.38c}$$

respectively, and the force vectors $\hat{\underline{F}}^{\text{ext}}$ and $\hat{\underline{F}}$ are defined as

$$\hat{\underline{F}}^{\text{ext}} = \int_0^L \underline{\underline{N}}'^T \underline{\mathcal{F}}^{\text{ext}}\, \mathrm{d}\alpha_1, \tag{2.39a}$$

$$\hat{\underline{F}} = \int_0^L (\underline{\underline{N}}^T \underline{\mathcal{F}}^I + \underline{\underline{N}}^T \underline{\mathcal{F}}^D + \underline{\underline{N}}'^T \underline{\mathcal{F}}^C)\, \mathrm{d}\alpha_1, \tag{2.39b}$$

respectively. More details are provided in Ref. [118]. In the next section, the unsteady aerodynamic forces and moments acting along the beam, accounted for in $\hat{\underline{F}}^{\text{ext}}$, are derived.

2.3 Unsteady Aerodynamics

In order to compute aerodynamic loads acting on the wing of the aircraft, an airfoil is rigidly attached to each node of the beam element. To this end, it is assumed that the aerodynamic properties of the airfoil as well as the inertia forces remain unaffected by the warping of the cross-section. According to thin airfoil theory, the aerodynamic forces consist of lift and drag which are applied at the aerodynamic center of the beam. At low air speeds and incompressible flow regimes, which are typical of flight speeds of most HALE aircrafts, the location of the aerodynamic center remains constant at the quarter-chord of the airfoil. Since the airfoil is rigidly attached to the nodes of the beam element, its kinematic parameters are fully defined by those of the corresponding node. Configuration of an airfoil attached to a beam element and moving in an inertial

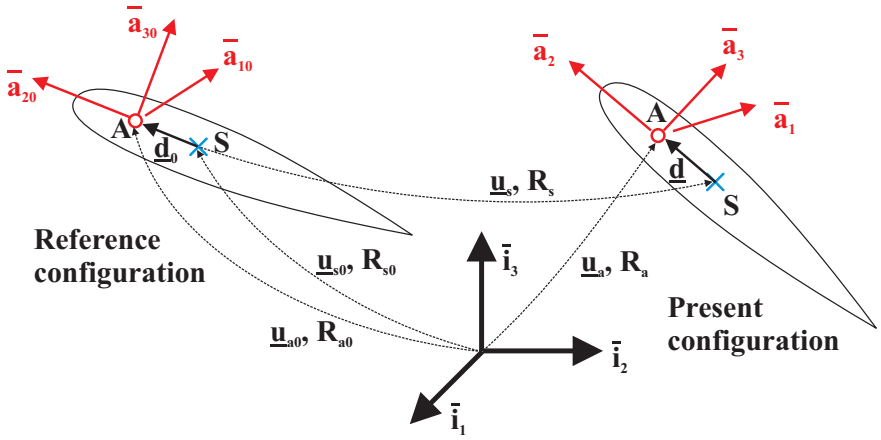

Figure 2.2: An airfoil in the reference and present configurations [119]

reference frame is shown in Fig. 2.2. The orientation of the airfoil is defined by an orthonormal basis $\mathcal{A} = (\overline{a}_1, \overline{a}_2, \overline{a}_3)$ attached to the quarter chord location of the airfoil. According to Fig. 2.2, if the nodal point is denoted as **s**, the inertial position of the aerodynamic center of the airfoil, $\underline{u}_a$, can be described as

$$\begin{aligned} \underline{u}_a &= \underline{u}_{s0} + \underline{u}_s + \underline{d} \\ &= \underline{u}_{s0} + \underline{u}_s + \underline{\underline{R}}_s \underline{d}_0, \end{aligned} \tag{2.40}$$

where $\underline{u}_{s0}$ and $\underline{u}_s$ are the inertial position of the node in the reference and deformed configurations, respectively, and $\underline{\underline{R}}_s$ defines the orientation of the beam at that cross section. The orientation tensor, $\underline{\underline{R}}_a$, of the basis $\mathcal{A}$ then can be found from

$$\underline{\underline{R}}_a = \underline{\underline{R}}_s \, \underline{\underline{R}}_{a0}. \tag{2.41}$$

The velocity of the aerodynamic center, $\underline{v}_a$, can be easily found as

$$\underline{v}_a = \underline{v}_s + \widetilde{\omega}_s \, \underline{d}. \tag{2.42}$$

The relative velocity of the flow with respect to the airfoil aerodynamic center, $\underline{\hat{v}}_a^{\mathrm{qc}}$, is defined as

$$\underline{\hat{v}}_a^{\mathrm{qc}} = \underline{V}_\infty + \underline{\lambda} - \underline{v}_a, \tag{2.43}$$

in which $\underline{V}_\infty$ and $\underline{\lambda}$ are the free-stream flow velocity and the average inflow velocity, respectively. Similarly, the rerelative velocity of the flow with respect to the airfoil mid-chord point, $\underline{\hat{v}}_a^{\mathrm{mc}}$, which is needed for the unsteady aerodynamic model of Peters *et al.* [57] is written as

$$\underline{\hat{v}}_a^{\mathrm{mc}} = \underline{V}_\infty + \underline{\lambda} - (\underline{\hat{v}}_a^{\mathrm{qc}} - \widetilde{\omega}_s\, \underline{\eta}), \tag{2.44}$$

where $\underline{\eta}$ is the relative position of aerodynamic center with respect to the mid-chord point. To facilitate the computation of aerodynamic forces and moments, the relative velocities are resolved in the airfoil basis, $\mathcal{A}$, as

$$\underline{\hat{v}}_a^{\mathrm{qc}\mathcal{A}} = \underline{\underline{R}}_a^T\, [\underline{V}_\infty + \underline{\lambda} - \underline{v}_a], \tag{2.45a}$$

$$\underline{\hat{v}}_a^{\mathrm{mc}\mathcal{A}} = \underline{\underline{R}}_a^T\, [\underline{V}_\infty + \underline{\lambda} - (\underline{\hat{v}}_a^{\mathrm{qc}} - \widetilde{\omega}_s\, \underline{\eta})] = \underline{\hat{v}}_a^{\mathrm{qc}\mathcal{A}} + \widetilde{\omega}_s^{\mathcal{A}}\, \underline{\eta}^{\mathcal{A}}. \tag{2.45b}$$

If the semi-chord length of the airfoil is represented by b, then

$$\underline{\eta}^{\mathcal{A}} = \left\{ \begin{array}{c} 0 \\ b/2 \\ 0 \end{array} \right\}. \tag{2.46}$$

Finally, the relative velocity components resolved in the basis $\mathcal{A}$ can be cast as

$$\underline{\hat{v}}_a^{\mathcal{A}} = \left\{ \begin{array}{c} U_1 \\ -U_2 \\ U3 \end{array} \right\}, \tag{2.47}$$

where the sign conventions are shown in Fig. 2.3. The span-wise component of the

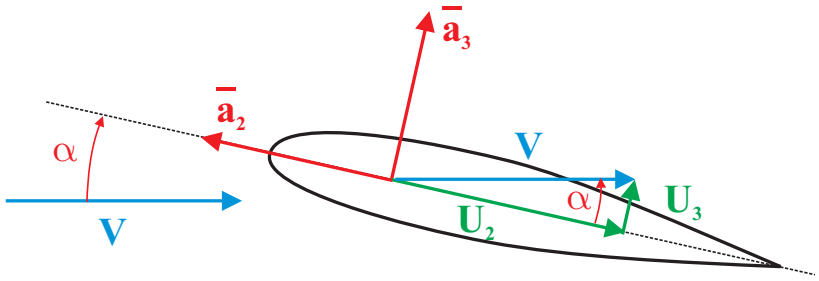

Figure 2.3: Relative air velocity with respect to the quarter-chord [119]

relative air velocity, U_1 is much smaller than the other two components and, therefore, ignored in 2D unsteady aerodynamic theory. The flow velocity, V, is then defined as

$$V^2 = U_2^2 + U_3^2, \tag{2.48}$$

which can be utilized to compute the angle of attack, α, as

$$\alpha = \tan^{-1} \frac{U_3}{U_2}. \tag{2.49}$$

The inflow velicity, $\underline{\lambda}$, can be found from finite-state induced flow theory of Peters *et al.* [57] by solving the following system of linear ordinary differential equations

$$\underline{\underline{A}}\, \underline{\dot{\mu}} + \frac{V}{b} \underline{\mu} = \dot{U}_3\, \underline{c}, \tag{2.50}$$

where $\underline{\mu}$ is the inflow states array. The system of equations (2.50) can be solved using a central difference scheme as

$$\underline{\underline{A}}\, \frac{\underline{\mu}_f - \underline{\mu}_i}{\Delta t} + \frac{V}{b} \frac{\underline{\mu}_f + \underline{\mu}_i}{2} = \frac{U_{3f} - U_{3i}}{\Delta t}\, \underline{c}, \tag{2.51}$$

where $(\cdot)_i$ and $(\cdot)_f$ denote the values of the variables computed at the beginning and the end of the time step, respectively. Therefore,

$$\underline{\mu}_f = \left(\underline{\underline{A}} + \frac{\Delta\tau}{2}\underline{\underline{I}}\right)^{-1} \left[(U_{3f} - U_{3i})\ \underline{c} + \left(\underline{\underline{A}} - \frac{\Delta\tau}{2}\underline{\underline{I}}\right)\underline{\mu}_i\right], \tag{2.52}$$

where $\underline{\underline{I}}$ and $\Delta\tau = V\Delta t/b$ are identity matrix and non-dimensional time step size, respectively.

The magnitude of the average inflow vector, λ_0, is then a linear combination of the inflow states as

$$\lambda_0 = \frac{1}{2}\underline{b}^T\,\underline{\mu}. \tag{2.53}$$

This average inflow acts along a unit vector, $\overline{a}_\lambda$, in the airfoil plane defined by

$$\overline{a}_\lambda = -\frac{\widetilde{V}_\infty \overline{a}_1}{\|\widetilde{V}_\infty \overline{a}_1\|}. \tag{2.54}$$

The average inflow vector, then, is

$$\underline{\lambda} = \lambda_0\,\overline{a}_\lambda. \tag{2.55}$$

The matrix $\underline{\underline{A}}$ is then defined as

$$\underline{\underline{A}} = \underline{\underline{D}} + \underline{d}\,\underline{b}^T + \underline{c}\,\underline{d}^T + \frac{1}{2}\underline{c}\,\underline{b}^T, \tag{2.56}$$

where

$$\begin{aligned} b_n &= (-1)^{n-1}\frac{(N+n)!}{(N-n)!}\frac{1}{(n!)^2}, \\ b_N &= (-1)^{N+1}, \end{aligned} \tag{2.57}$$

and

$$c_n = \frac{2}{n}. \tag{2.58}$$

Also

$$d_n = \begin{cases} 1/2 & \text{for} \quad n = 1, \\ 0 & \text{for} \quad n \neq 1, \end{cases} \tag{2.59}$$

and, finally

$$D_{mn} = \begin{cases} n/2 & \text{for} \quad n = m + 1, \\ -n/2 & \text{for} \quad n = m - 1, \\ 0 & \text{for} \quad n \neq m \pm 1. \end{cases} \tag{2.60}$$

For a thin airfoil, in 2D a inviscid, incompressible flow, the steady component of lift, drag, and moment are found from

$$L_{\mathrm{s}} = \rho_\infty b a_0 U_2 U_3, \tag{2.61a}$$

$$D_{\mathrm{s}} = \rho_\infty b a_0 U_3^2, \tag{2.61b}$$

$$M_{\mathrm{s}}^{\mathrm{qc}} = 0, \tag{2.61c}$$

where ρ_∞ is the density of air, b is the semi-chord length, and $a_0 = 2\pi$ is the lift curve slope. Also, the unsteady components of lift, drag, and moment are defined by

$$L_{\mathrm{us}} = \rho_\infty \frac{b^2}{2} a_0 (\dot{U}_3 + U_2 \omega_1), \tag{2.62a}$$

$$D_{\mathrm{us}} = 0, \tag{2.62b}$$

$$M_{\mathrm{us}}^{\mathrm{qc}} = -\rho_\infty \frac{b^4}{16} a_0 \dot{\omega}_1 - \frac{b}{2} L_{\mathrm{us}}. \tag{2.62c}$$

2.4 Formulating the Transformation Matrix

Figure 2.4 shows the schematic of a typical joined model. To enforce the continuity conditions at the interface between 1D and 3D parts, the variational asymptotic method is used to derive the transformation between the joint nodes. The details of the derivations are presented by Song and Hodges [26].

The three displacement and three rotational degrees of freedom of the single node

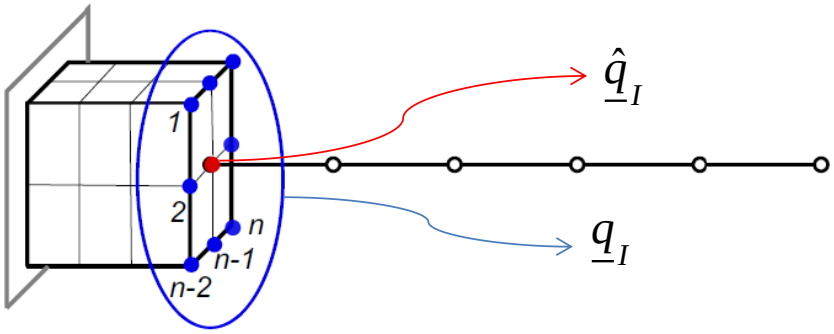

Figure 2.4: The schematic of a typical joined model

of the beam at the interface are defined as

$$\underline{\hat{q}}_I = \begin{bmatrix} \hat{u}_1 & \hat{u}_2 & \hat{u}_3 & \hat{\theta}_1 & \hat{\theta}_2 & \hat{\theta}_3 \end{bmatrix}^T, \tag{2.63}$$

while the $3n$ degrees of freedom of the n nodes at the joined section of the solid part are

$$\underline{q}_I = \begin{bmatrix} u_1^1 & u_2^1 & u_3^1 & \dots & u_1^n & u_2^n & u_3^n \end{bmatrix}^T. \tag{2.64}$$

Also, the sectional stress resultants at the beam interface are represented as

$$\underline{\hat{F}} = \begin{bmatrix} \hat{N}_1 & \hat{N}_2 & \hat{N}_3 & \hat{M}_1 & \hat{M}_2 & \hat{M}_3 \end{bmatrix}^T, \tag{2.65}$$

and the nodal forces at the solid interface are represented by

$$\underline{F} = \begin{bmatrix} F_1^1 & F_2^1 & F_3^1 & \dots & F_1^n & F_2^n & F_3^n \end{bmatrix}^T. \tag{2.66}$$

Therefore, the displacement and rotation continuity condition can be shown as

$$\underline{\underline{R}}\,\underline{q}_I = \underline{\hat{q}}_I, \tag{2.67}$$

and the load continuity condition is casted as

$$-\underline{\underline{S}}\,\underline{\hat{F}} = \underline{F}, \tag{2.68}$$

where, $\underline{\underline{R}}$ and $\underline{\underline{S}}$ are transformation matrices to be derived from VAM. Note that $\underline{\underline{S}}$ is a $3n\times6$ matrix. It is shown in Ref. [26] that

$$\underline{\underline{R}}^T = \underline{\underline{S}}, \tag{2.69}$$

and therefore they can be used interchangeably.

Sectional stress resultants can be related to the generalized strain measures as

$$\underline{\varepsilon} = \underline{\underline{\Phi}}\,\underline{\hat{F}}, \tag{2.70}$$

where $\underline{\varepsilon} = \begin{bmatrix} \gamma_{11} & 2\gamma_{12} & 2\gamma_{13} & \kappa_1 & \kappa_2 & \kappa_3 \end{bmatrix}^T$ consists of sectional stretch and shear strain measures as well as sectional curvatures obtained from a generalized Timoshenko beam analysis, and $\underline{\underline{\Phi}}$ the 6×6 cross-sectional flexibility matrix derived from VABS. Rewriting 1D strain measures for the generalized Timoshenko model as

$$\begin{aligned} \underline{\epsilon} &= \begin{bmatrix} \gamma_{11} & \kappa_1 & \kappa_2 & \kappa_3 \end{bmatrix}^T, \\ \underline{\gamma}_s &= \begin{bmatrix} 2\gamma_{12} & 2\gamma_{13} \end{bmatrix}^T, \end{aligned} \tag{2.71}$$

we can then relate $\underline{\epsilon}$ and $\underline{\gamma}_s$ in terms of classical strain measures, $\bar{\underline{\epsilon}}$, using

$$\begin{aligned} \bar{\underline{\epsilon}} &= \underline{\epsilon} + \underline{\underline{Q}}\,\underline{\gamma}_s' + \underline{\underline{P}}\,\underline{\gamma}_s, \\ \bar{\underline{\epsilon}}' &= \underline{\epsilon}' + \underline{\underline{Q}}\,\underline{\gamma}_s'' + \underline{\underline{P}}\,\underline{\gamma}_s', \\ \bar{\underline{\epsilon}}'' &= \underline{\epsilon}'' + \underline{\underline{Q}}\,\underline{\gamma}_s''' + \underline{\underline{P}}\,\underline{\gamma}_s''. \end{aligned} \tag{2.72}$$

Here $\underline{\underline{P}}$ and $\underline{\underline{Q}}$ are matrices defined as

$$\underline{\underline{P}} = \begin{bmatrix} 0 & 0 \\ k_2 & k_3 \\ -k_1 & 0 \\ 0 & -k_1 \end{bmatrix}, \qquad \underline{\underline{Q}} = \begin{bmatrix} 0 & 0 \\ 0 & 0 \\ 0 & -1 \\ 1 & 0 \end{bmatrix}, \tag{2.73}$$

where components of k_i are the initial twist and curvatures of the beam. The detailed derivation can be found in Hodges [1].

The 3D strain field is defined as a column matrix in the form of

$$\underline{\Gamma} = \begin{bmatrix} \Gamma_{11} & 2\Gamma_{12} & 2\Gamma_{13} & \Gamma_{22} & 2\Gamma_{23} & \Gamma_{33} \end{bmatrix}^T. \tag{2.74}$$

To recover the 3D strain field in the beam, asymptotically correct warping functions from VABS is used to cast the strain field as

$$\begin{aligned} \underline{\Gamma} = & \left[\left(\Gamma_a + \Gamma_R \right) \left(V_0 + V_{1R} \right) + \Gamma_\epsilon \right] \underline{\bar{\epsilon}} \\ & + \left[\left(\Gamma_a + \Gamma_R \right) V_{1S} + \Gamma_l \left(V_0 + V_{1R} \right) \right] \underline{\bar{\epsilon}}' \\ & + \Gamma_l V_{1S} \underline{\bar{\epsilon}}'', \end{aligned} \tag{2.75}$$

where V_0, V_{1R} and V_{1S} are the nodal values of the asymptotically correct warping functions for classical modeling, the correction from nonzero initial curvatures/twist and the correction from transverse shear deformation, respectively, which are found from VABS. Γ_a, Γ_R, Γ_ϵ and Γ_l, are differential and algebraic matrix operators containing

nodal coordinates and geometry information defined by Hodges [1] as

$$\Gamma_a = \begin{bmatrix} 0 & 0 & 0 \\ \frac{\partial}{\partial x_2} & 0 & 0 \\ \frac{\partial}{\partial x_3} & 0 & 0 \\ 0 & \frac{\partial}{\partial x_2} & 0 \\ 0 & \frac{\partial}{\partial x_3} & \frac{\partial}{\partial x_2} \\ 0 & 0 & \frac{\partial}{\partial x_3} \end{bmatrix}, \tag{2.76}$$

$$\Gamma_\epsilon = \frac{1}{\sqrt{g}} \begin{bmatrix} 1 & 0 & x_3 & -x_2 \\ 0 & -x_3 & 0 & 0 \\ 0 & x_2 & 0 & 0 \\ 0 & 0 & 0 & 0 \\ 0 & 0 & 0 & 0 \\ 0 & 0 & 0 & 0 \end{bmatrix}, \tag{2.77}$$

$$\Gamma_R = \frac{1}{\sqrt{g}} \begin{bmatrix} \widetilde{k} + \underline{\underline{\Delta}} k_1 \left(x_3 \frac{\partial}{\partial x_2} - x_2 \frac{\partial}{\partial x_3} \right) \\ \underline{\underline{O}} \end{bmatrix}, \tag{2.78}$$

$$\Gamma_l = \frac{1}{\sqrt{g}} \begin{bmatrix} \underline{\underline{\Delta}} \\ \underline{\underline{O}} \end{bmatrix}, \tag{2.79}$$

where x_i's are nodal coordinates, $\underline{\underline{\Delta}}$ is a 3×3 identity matrix, $\underline{\underline{O}}$ is a 3×3 matrix of zeros, the operator $\widetilde{(\ )}$ is defined such that $\widetilde{(\ )}_{ij} = -e_{ijk}(\ )_k$ and g is the determinant of the metric tensor for the undeformed state, with $\sqrt{g} = 1 - x_2 k_3 + x_3 k_2$.

Knowing the 3D strain field, we can find the 3D stress field through stress-strain relation

$$\underline{\sigma} = \underline{\underline{\mathcal{D}}}\,\underline{\Gamma}, \tag{2.80}$$

where $\underline{\underline{\mathcal{D}}}$ is the 6×6 material matrix, and $\underline{\sigma}$ is the 3D stress field that can be cast as

$$\underline{\sigma} = \begin{bmatrix} \sigma_{11} & \sigma_{12} & \sigma_{13} & \sigma_{22} & \sigma_{23} & \sigma_{33} \end{bmatrix}^T \tag{2.81}$$

According to Song and Hodges [26] the stress field can be recovered as

$$\underline{\sigma} = \underline{\underline{\mathcal{D}}}\, C_\Gamma\, \underline{\hat{F}}, \tag{2.82}$$

where C_Γ has the form

$$\begin{aligned} C_\Gamma = & \left[\left(\Gamma_a + \Gamma_R \right) \left(V_0 + V_{1R} \right) + \Gamma_\epsilon \right] C_{\bar{\epsilon}} \\ & + \left[\left(\Gamma_a + \Gamma_R \right) V_{1S} + \Gamma_l \left(V_0 + V_{1R} \right) \right] C_{\bar{\epsilon}'} \\ & + \Gamma_l V_{1S} C_{\bar{\epsilon}''}, \end{aligned} \tag{2.83}$$

and $C_{\bar{\epsilon}}$, $C_{\bar{\epsilon}'}$, and $C_{\bar{\epsilon}''}$ are operators defined in Song and Hodges [26].

After we obtain the 3D stress field on the interface, the stresses at each Gauss point can be calculated given its coordinates. The stresses on the Gauss points in each element are regarded as normal force distribution or shear force distribution on the interface. Therefore, we can integrate the distributed load over the area surrounding the corresponding Gauss point and lump this force to the nearest element node. Doing so, over all the elements on the interface, we can obtain the nodal forces for all the nodes on the interface. For the brick elements, there are six stress components at each Gauss point, shown in Fig. 2.5.

For an arbitrary element with four nodes, i, j, k, and l at the 2D interface we use four Gauss points shown as I, II, III, IV in Fig. 2.6. We can integrate stresses over the area around the Gauss point and find nodal forces for the corresponding Gauss point. For example at point I, the forces can be found by

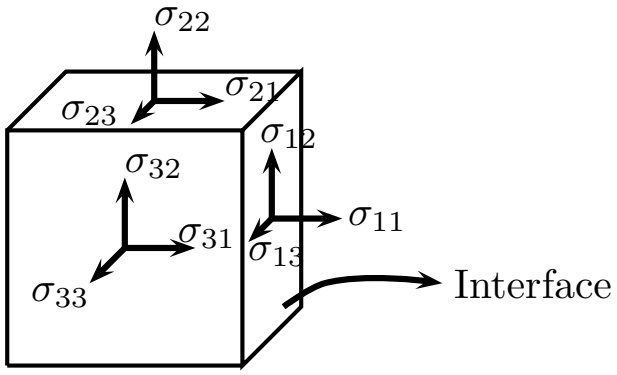

Figure 2.5: Stresses on an infinitesimal element at an arbitrary interface Gauss point

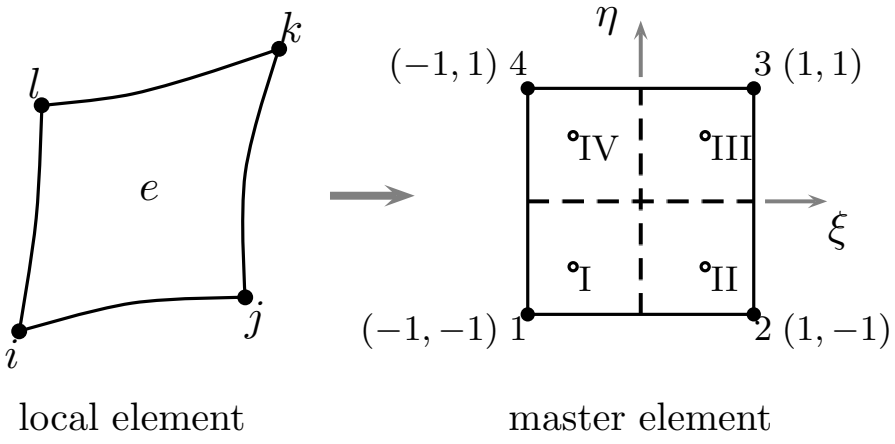

Figure 2.6: Gauss points on 2D four-node master element

$$
\begin{aligned}
F_1^I &= \int_{-1}^{0}\int_{-1}^{0} \sigma_{11}^I \, |J| \, d\xi d\eta = \sigma_{11}^I \, A^I, \\
F_2^I &= \int_{-1}^{0}\int_{-1}^{0} \sigma_{12}^I \, |J| \, d\xi d\eta = \sigma_{12}^I \, A^I, \\
F_3^I &= \int_{-1}^{0}\int_{-1}^{0} \sigma_{13}^I \, |J| \, d\xi d\eta = \sigma_{13}^I \, A^I,
\end{aligned} \tag{2.84}
$$

where $|J|$ is the determinant of the Jacobian matrix of the element, and A^I is the area surrounding the Gauss point I. The nodal forces can be obtained by extrapolation of the forces at the Gauss points, solving the linear system of equation

$$
\begin{bmatrix}
N_1(I) & N_2(I) & \cdots & N_n(I) \\
N_1(II) & N_2(II) & \cdots & N_n(II) \\
\vdots & \vdots & \vdots & \vdots \\
N_1(m) & N_2(m) & \cdots & N_n(m)
\end{bmatrix}
\begin{Bmatrix}
F_i^1 \\ F_i^2 \\ \vdots \\ F_i^n
\end{Bmatrix}
=
\begin{Bmatrix}
F_i^I \\ F_i^{II} \\ \vdots \\ F_i^m
\end{Bmatrix}
\qquad i = 1, 2, 3, \tag{2.85}
$$

with m Gauss points and n nodal points. N's are the shape functions at the Gauss point. Combining the elemental matrices we get

$$
\underline{F} = \underline{\underline{P}}_A \, \underline{\sigma}, \tag{2.86}
$$

where $\underline{\underline{P}}_A$ matrix contains the area information of the element and shape functions. Therefore, it is resulted from Eqn. (2.82) that

$$
\underline{F} = \underline{\underline{P}}_A \, \underline{\underline{\mathcal{D}}} \, C_\Gamma \, \underline{\hat{F}}. \tag{2.87}
$$

Thus, combining the matrices for all elements, the transformation matrix is found from Eq. (2.68) as

$$
\underline{\underline{S}} = -\underline{\underline{P}}_A \, \underline{\underline{\mathcal{D}}} \, C_\Gamma, \tag{2.88}
$$

which forms a linear system of constraints to be imposed at the interface.

2.5 Reduced Order Modeling

Systems of equations resulting from an FE discretization of the structure have a prohibitively large order which renders them unsuitable for control system design purposes. For control system design, a representative model of the system is desirable in which, while the most salient modes of the full order model are preserved, the order of equations is significantly smaller. Over the years many efficient ROM techniques have been developed by different researchers [82], which among them methods based on Galerkin projections have found numerous applications in structural dynamics problems.

Generic dynamical equations of a structural system acted upon by some time-dependent external loads can be described as

$$\underline{\underline{M}}\,\underline{\ddot{u}}(t) + \underline{\underline{G}}\,\underline{\dot{u}}(t) + \underline{\underline{K}}\,\underline{u}(t) = \underline{F}(t), \tag{2.89}$$

where $\underline{u} \in \mathbb{R}^n$ is the displacement vector, $\underline{\underline{M}}$ is the mass matrix, $\underline{\underline{G}}$ is the damping matrix, and $\underline{\underline{K}}$ is the stiffness matrix. Since the equation arising from FE discretization tend to have thousands of DOF, n is usually very large. However, in many cases, the trajectories of the full order model in a high dimensional space $\mathcal{H}$ are embedded in a lower dimensional subspace $\mathcal{S} \subset \mathcal{H}$ with dimension m where $m \ll n$. In fact, if

$$\underline{\underline{\Phi}} = \left[\underline{\phi}_1, \underline{\phi}_2, \ldots, \underline{\phi}_m\right], \tag{2.90}$$

is the matrix of m base vectors $\underline{\phi}_i$ spanning the subspace $\mathcal{S}$, then it can be said that

$$\underline{u}(t) \approx \underline{\underline{\Phi}}\,\underline{\breve{u}}(t), \tag{2.91}$$

where $\underline{\breve{u}} \in \mathbb{R}^m$ is the reduced set of coordinates. Substituting Eq. (2.91) into Eq. (2.89)

results in

$$\underline{\underline{M}}\,\underline{\underline{\Phi}}\,\ddot{\underline{\breve{u}}}(t) + \underline{\underline{G}}\,\underline{\underline{\Phi}}\,\dot{\underline{\breve{u}}}(t) + \underline{\underline{K}}\,\underline{\underline{\Phi}}\,\underline{\breve{u}}(t) \approx \underline{F}(t). \tag{2.92}$$

Galerkin projection techniques seek for a reduced order subspace $\mathcal{S}$ for which the residual vector of the approximation, $\underline{r}(t)$, defined as

$$\underline{r}(t) = \underline{F}(t) - \left(\underline{\underline{M}}\,\underline{\underline{\Phi}}\,\ddot{\underline{\breve{u}}}(t) + \underline{\underline{G}}\,\underline{\underline{\Phi}}\,\dot{\underline{\breve{u}}}(t) + \underline{\underline{K}}\,\underline{\underline{\Phi}}\,\underline{\breve{u}}(t)\right), \tag{2.93}$$

is orthogonal to the subspace, i.e.,

$$\underline{\underline{\Phi}}^T\,\underline{r} = \underline{0}. \tag{2.94}$$

Hence, the reduced order system is expressed as

$$\underline{\underline{\Phi}}^T\,\underline{\underline{M}}\,\underline{\underline{\Phi}}\,\ddot{\underline{\breve{u}}}(t) + \underline{\underline{\Phi}}^T\,\underline{\underline{G}}\,\underline{\underline{\Phi}}\,\dot{\underline{\breve{u}}}(t) + \underline{\underline{\Phi}}^T\,\underline{\underline{K}}\,\underline{\underline{\Phi}}\,\underline{\breve{u}}(t) = \underline{\underline{\Phi}}^T\,\underline{F}(t), \tag{2.95}$$

or, by grouping the terms, in a compact form as

$$\underline{\underline{\breve{M}}}\,\ddot{\underline{\breve{u}}}(t) + \underline{\underline{\breve{G}}}\,\dot{\underline{\breve{u}}}(t) + \underline{\underline{\breve{K}}}\,\underline{\breve{u}}(t) = \underline{\breve{F}}(t). \tag{2.96}$$

Being a projection based method, POD seeks an orthogonal projection of fixed rank m defined as

$$\Pi_{\mathcal{S}} = \mathcal{H} \rightarrow \mathcal{S}, \tag{2.97}$$

whereby minimizing the integrated projection error

$$\mathcal{J} = \int_0^{t_f} \|\underline{u}(t) - \Pi_{\mathcal{S}}\,\underline{u}(t)\|_2^2\,\mathrm{d}t = \int_0^{t_f} \|\underline{e}(t)\|_2^2\,\mathrm{d}t. \tag{2.98}$$

It can be shown that if the correlation matrix $\underline{\underline{\mathcal{K}}} \in \mathbb{R}^{n\times n}$ is defined by

$$\underline{\underline{\mathcal{K}}} = \int_0^{t_f} \underline{u}(t)\underline{u}(t)^T \mathrm{d}t, \tag{2.99}$$

and

$$\lambda_1 \geq \lambda_2 \geq \cdots \geq \lambda_n \geq 0, \tag{2.100}$$

are the eignevalues of $\underline{\underline{\mathcal{K}}}$, resulting from solving the equation,

$$\underline{\underline{\mathcal{K}}}\,\underline{\phi}_i = \lambda_i\,\underline{\phi}_i \qquad i = 1, \ldots, n, \tag{2.101}$$

such that $\lambda_m > \lambda_{m+1}$, then the subspace spanned by the eigenspace of $\underline{\underline{\mathcal{K}}}$ associated with $\lambda_1, \ldots, \lambda_m$ minimizes $\mathcal{J}$. However, because the dimension of $\underline{\underline{\mathcal{K}}}$ is large, solving the eigenvalue equation (2.101) is computationally expensive. Thus, the method of snapshots [120] is utilized. In the method of snapshots, the snapshot matrix, is formed by $N_{\text{snap}} = m$ discrete snapshots of the response of the system as

$$\underline{\underline{\mathcal{Y}}} = \left[\underline{u}(t_1),\, \underline{u}(t_2),\, \ldots,\, \underline{u}(t_{N_{\text{snap}}})\right]. \tag{2.102}$$

The new correlation matrix is constructed as

$$\underline{\underline{\mathcal{K}}} = \sum_{i=1}^{N_{\text{snap}}} \underline{u}(t_i)\,\underline{u}(t_i)^T = \underline{\underline{\mathcal{Y}}}\,\underline{\underline{\mathcal{Y}}}^T. \tag{2.103}$$

Since the nonzero eigenvalues of $\underline{\underline{\mathcal{Y}}}\,\underline{\underline{\mathcal{Y}}}^T \in \mathbb{R}^{n\times n}$ and $\underline{\underline{\mathcal{Y}}}^T\,\underline{\underline{\mathcal{Y}}} \in \mathbb{R}^{m\times m}$ are the same, instead of solving the eigenvalue equation (2.101), one may solve the equation

$$\underline{\underline{\mathcal{Y}}}^T\,\underline{\underline{\mathcal{Y}}}\,\underline{\psi}_i = \lambda_i\,\underline{\psi}_i \qquad i = 1, \ldots, N_{\text{snap}}. \tag{2.104}$$

Then, the first m POD modes are given as

$$\underline{\phi}_i = \frac{1}{\sqrt{\lambda_i}} \underline{\underline{\mathcal{Y}}}\, \underline{\psi}_i \qquad i = 1, \ldots, m. \tag{2.105}$$

For rectangular matrices, such as $\underline{\underline{\mathcal{Y}}}$, there is a close connection between POD and Singular Value Decomposition (SVD), as the SVD of $\underline{\underline{\mathcal{Y}}}$ is constructed as

$$\underline{\underline{\mathcal{Y}}} = \underline{\underline{\mathcal{U}}}\, \underline{\underline{\Sigma}}\, \underline{\underline{\mathcal{V}}}^T, \tag{2.106}$$

where $\underline{\underline{\mathcal{U}}} \in \mathbb{R}^{n \times n}$ and $\underline{\underline{\mathcal{V}}} \in \mathbb{R}^{m \times m}$ are unitary matrices

$$\underline{\underline{\Sigma}} = \begin{bmatrix} \underline{\underline{\Sigma}}_m & \underline{\underline{0}} \\ \underline{\underline{0}} & \underline{\underline{0}} \end{bmatrix}, \tag{2.107}$$

$$\underline{\underline{\Sigma}}_m = \mathrm{diag}(\sigma_1,\, \sigma_2,\, \ldots,\, \sigma_m),$$

where

$$\sigma_1 \geq \sigma_2 \geq \cdots \geq \sigma_m > 0, \tag{2.108}$$

are nonzero singular values of $\underline{\underline{\mathcal{Y}}}$. This offers a practical way of finding a basis, $\underline{\underline{\Phi}}$, as the first m columns of $\underline{\underline{\mathcal{U}}}$. Finally the ROM can be reconstructed using Eqs. (2.95) and (2.96).

2.6 Flutter Suppression System

Flutter can negatively impact the life cycle of the structure and, left unchecked, may compromise the structural integrity of the aircraft which potentially leads to catastrophic failure of the structure. Active flutter suppression systems have gained popularity among researchers. A properly designed active control system offers many advantages, including robustness with respect to system parameter changes and disturbance rejection, over passive controllers. The joined 1D/3D model, developed

in the previous sections, is used as the testbed for devising a feedback controller. Although the joined 1D/3D model drastically reduces the number of DOF vis-a-vis full 3D model, the system size is still very large for control design purpose. Hence, POD is used to extract from FOM, an ROM consisting of only a few dominant modes. The resulting ROM is an approximate model of the full nonlinear system linearized about an equilibrium condition. It can be used along with control design methods, including Linear Quadratic Regulator (LQR) and Linear Quadratic Gaussian (LQG). LQG method is particularly attractive because it provides a means for dealing with systems in which all of the states are not available for feedback. The LQG problem is formulated in this section.

Consider a Linear Time Invariant (LTI) system in state-space form as

$$\begin{aligned} \dot{\underline{x}}(t) &= \underline{\underline{A}}\,\underline{x}(t) + \underline{\underline{B}}\,\underline{u}(t) + \underline{\underline{W}}\,\underline{w}(t), \\ \underline{y}(t) &= \underline{\underline{C}}\,\underline{x}(t) + \underline{\underline{D}}\,\underline{u}(t) + \underline{\underline{V}}\,\underline{v}(t), \end{aligned} \tag{2.109}$$

where $\underline{x} \in \mathbb{R}^{n\times n}$, $\underline{y} \in \mathbb{R}^m$, and $\underline{u} \in \mathbb{R}^p$, are the state, output and control vectors, respectively. $\underline{w} \in \mathbb{R}^n$and $\underline{v} \in \mathbb{R}^m$ are process and measurement noise, respectively, with intensity matrices $\underline{\underline{W}} \geq 0$ and $\underline{\underline{V}} > 0$. The control problem is to find the control vector $\underline{u} \in \mathbb{R}^p$ that minimizes the cost functional

$$\mathcal{J} = E\left[\underline{x}^T \underline{\underline{Q}}\,\underline{x} + \underline{u}^T \underline{\underline{R}}\,\underline{u}\right], \tag{2.110}$$

with $\underline{\underline{Q}}$ and $\underline{\underline{R}}$ being semi-positive definite and positive definite, respectively. It can be shown [121] that, a control law as

$$\underline{u} = -\underline{\underline{G}}\,\underline{\hat{x}}, \tag{2.111}$$

can minimize Eq. (2.110) with $\underline{\underline{G}} \in \mathbb{R}^{m\times n}$ as the matrix of feedback gains and $\underline{\hat{x}}$ being

the estimated state vector evolving according to

$$\dot{\underline{\hat{x}}}(t) = \underline{\underline{A}}\,\underline{\hat{x}}(t) + \underline{\underline{B}}\,\underline{u}(t) + \underline{\underline{K}}\,(\underline{y} - \underline{\underline{C}}\,\underline{\hat{x}}). \tag{2.112}$$

In Eq. (2.112), $\underline{\underline{K}} \in \mathbb{R}^{n\times m}$ is the gain matrix of Kalman filter, having the form

$$\underline{\underline{K}} = \underline{\underline{P}}\,\underline{\underline{C}}^T\underline{\underline{V}}^{-1}, \tag{2.113}$$

where $\underline{\underline{P}}$ is the positive definite solution of the Algebraic Riccati Equation (ARE)

$$\underline{\underline{P}}\,\underline{\underline{A}}^T + \underline{\underline{A}}\,\underline{\underline{P}} - \underline{\underline{P}}\,\underline{\underline{C}}^T\underline{\underline{V}}^{-1}\underline{\underline{C}}\,\underline{\underline{P}} + \underline{\underline{W}} = \underline{\underline{0}}. \tag{2.114}$$

Feedback gain, $\underline{\underline{G}}$, is also found from

$$\underline{\underline{G}} = \underline{\underline{R}}^{-1}\underline{\underline{B}}^T\underline{\underline{P}}, \tag{2.115}$$

with $\underline{\underline{P}}$ being the positive definite solution of the ARE

$$\underline{\underline{P}}\,\underline{\underline{A}} + \underline{\underline{A}}^T\underline{\underline{P}} - \underline{\underline{P}}\,\underline{\underline{B}}\,\underline{\underline{R}}^{-1}\underline{\underline{B}}^T\,\underline{\underline{P}} + \underline{\underline{Q}} = \underline{\underline{0}}. \tag{2.116}$$

A backward difference scheme is used to discretize the estimator equation, Eq. (2.112), as

$$\frac{\underline{\hat{x}}_f - \underline{\hat{x}}_i}{\Delta t} = (\underline{\underline{A}} - \underline{\underline{B}}\,\underline{\underline{G}} - \underline{\underline{K}}\,\underline{\underline{C}})\underline{\hat{x}}_f + \underline{\underline{K}}\,\underline{y}, \tag{2.117}$$

which yields

$$\underline{\hat{x}}_f = \left[\underline{\underline{I}} - \Delta t\,(\underline{\underline{A}} - \underline{\underline{B}}\,\underline{\underline{G}} - \underline{\underline{K}}\,\underline{\underline{C}})\right]^{-1}\left(\underline{\underline{K}}\,\underline{y} + \Delta t\,\underline{\hat{x}}_i\right). \tag{2.118}$$

The measurement vector, $\underline{y}$, is only available at the end of the last time step which makes the procedure explicitly dependent on it.

CHAPTER III

STATIC STRESS ANALYSIS FOR COMPOSITE BEAM

3.1 Introduction

In this chapter the validity of the joined 3D/1D method for various static and dynamic analysis is examined. To this end, a layered composite beam, clamped at one end and loaded by a transverse tip load is considered as a test case. The beam has four layers, each layer made of an orthotropic material whose properties are listed in Table 3.1. First an undamaged structure is studied and different damage scenarios for that structure will be investigated in the subsequent sections. For all test cases, the results will be compared and contrasted with full 3D FEA.

3.2 Static and Frequency Analysis

3.2.1 Displacements and Stress Distribution

Figue 3.1 shows a schematic of both full 3D and joined 3D/1D model of the beam. The rectangular cross section has the dimensions of 0.02 m by 0.08 m and the beam

Table 3.1: Material properties and layup of anisotropic beam

Material properties
$E_t = 1.42 \times 10^{11}$ N/m^2
$\nu_{lt} = \nu_{tn} = 0.42$
$E_l = 9.8 \times 10^9$ N/m^2
$G_{lt} = G_{tn} = 6 \times 10^9$ N/m^2
$\rho = 1577$ kg/m^3
Layup
$[-45°/+45°/-45°/+45°]$

has a total length of 1 m. For the joined model, 0.2 m of the end of the beam is modeled as a 3D solid, and the rest of the beam is modeled with the 1D beam element introduced in the preceding chapter.

A transverse load with a magnitude of 400 N in the z direction is applied at the tip. The simulation results of the general nonlinear static analysis for the boundary block of the joined model and the comparison with the results for similar regions of the full 3D model are presented. Figure 3.2 shows the u_1 displacement for both full 3D and joined models. As it can be seen in the figure, no visible difference exists in the area of concern between the results for both models, and the maximum difference for u_1 is 0.20%. Therefore, both the amplitude and distribution of axial displacement are correctly predicted by the joined model. Figure 3.3 shows the u_2 displacement for both full 3D and joined model. As it can be seen in the figure, the difference between the results are quite negligible and the joined model agrees very well with the full 3D model, such that the error in the area of concern is not greater than 0.20%.

The same behavior is shown in Fig. 3.4 for u_3. Since the loading is in z direction, one might expect higher differences in u_3, however, the maximum error is 0.16% for this variable in that region. It should be mentioned that the final tip deflection in z direction is predicted as 0.119 m, which shows that the beam undergoes a moderate displacement, and the modeling is still capable of predicting the correct displacements.

The results for normal stress in x direction, σ_{11}, for the composite beam under consideration are shown in Fig. 3.5. As it was the case for the displacements, the joined model provides good estimates for σ_{11}, and no visible differences exist between the results for the area under consideration. The same behavior can be seen in Fig. 3.6 for transverse shear σ_{12}. Although the variations in shear stresses are high in composite beams, the joined model is capable of correctly predicting the shear stress. The converged results are very similar, and the maximum difference in σ_{12} does not exceed 0.30%.

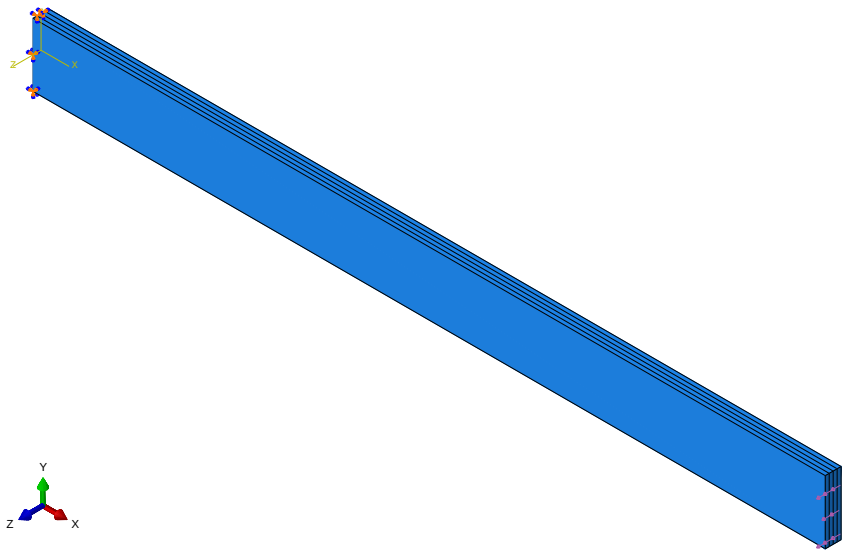

(a) Full 3D

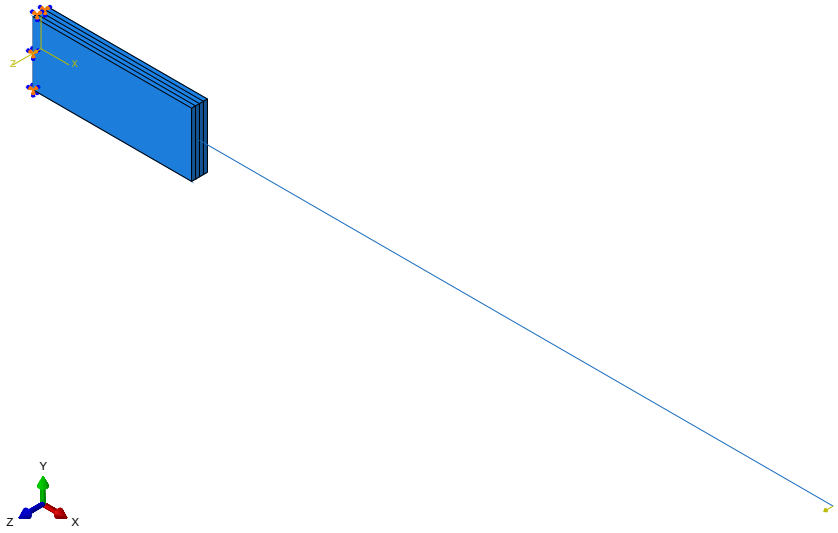

(b) Joined 3D/1D

Figure 3.1: Composite cantilevered beam loaded at the tip

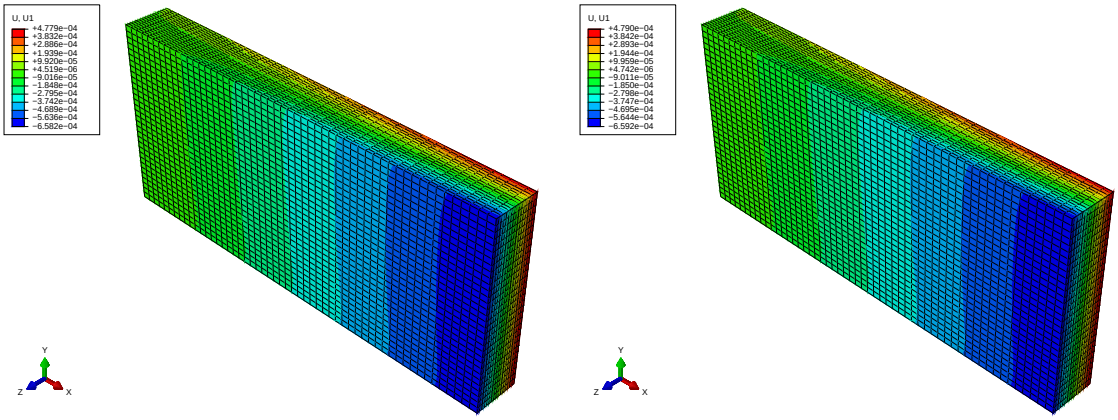

(a) Full 3D **(b)** Joined 3D/1D

Figure 3.2: Axial displacement, u_1; maximum difference difference in magnitude: 0.20%

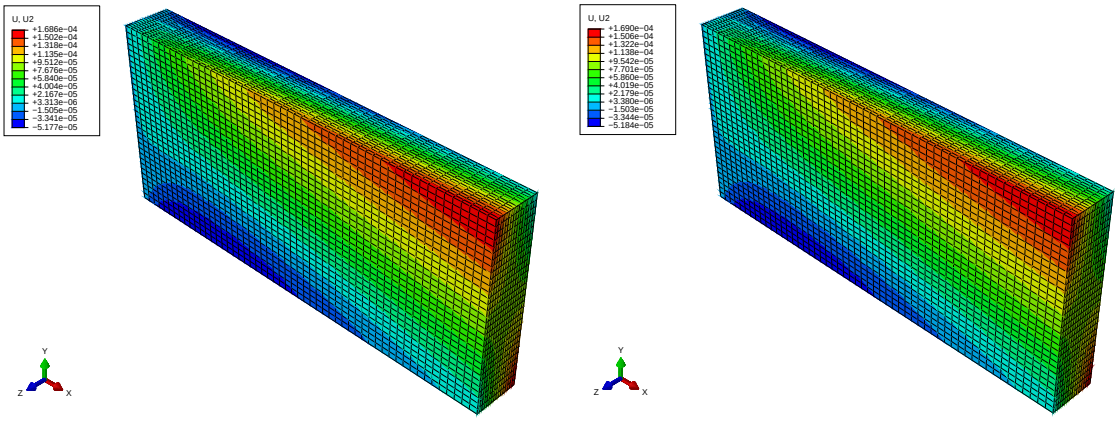

(a) Full 3D **(b)** Joined 3D/1D

Figure 3.3: Transverse displacement, u_2; maximum difference in magnitude: 0.20%

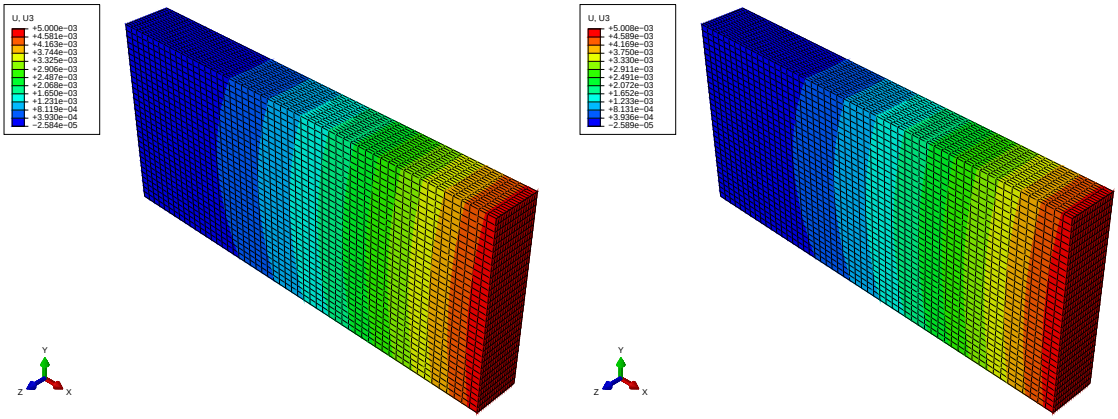

(a) Full 3D **(b)** Joined 3D/1D

Figure 3.4: Transverse displacement, u_3; maximum difference in magnitude: 0.16%

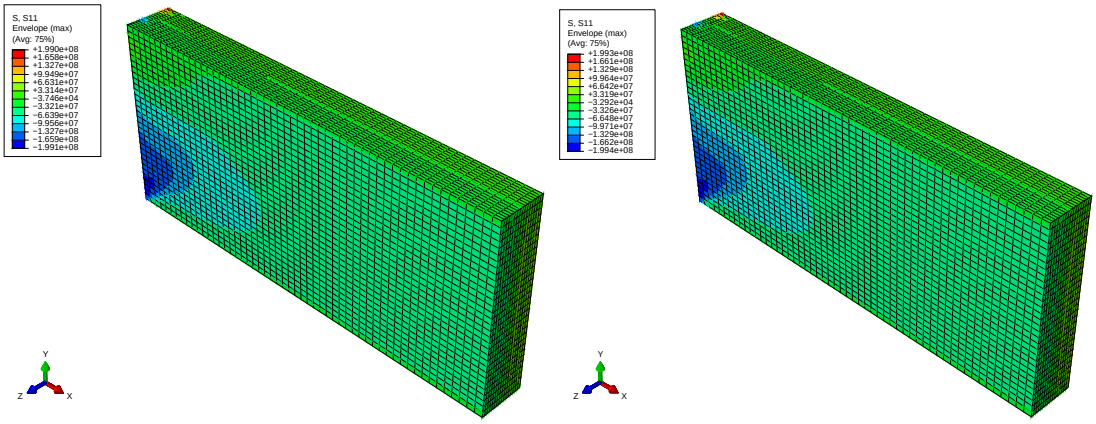

(a) Full 3D **(b)** Joined 3D/1D

Figure 3.5: Normal stress, σ_{11}; maximum difference in magnitude: 0.15%

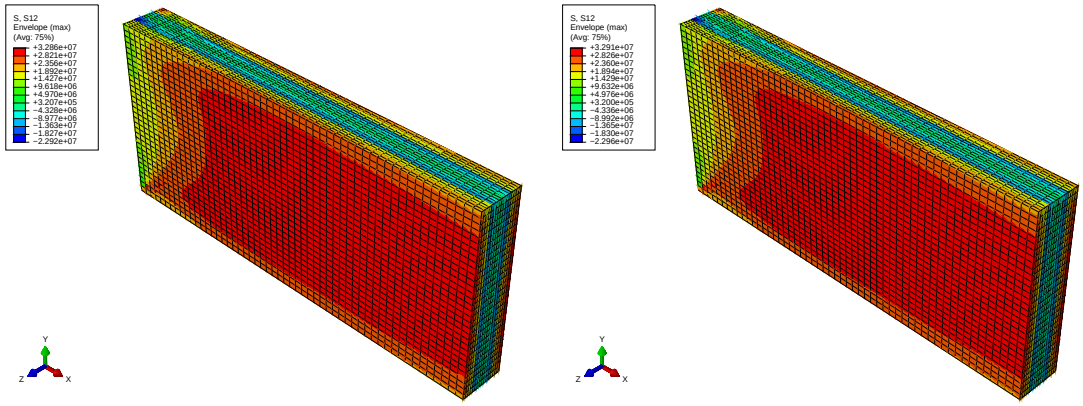

(a) Full 3D **(b)** Joined 3D/1D

Figure 3.6: Transverse shear stress, σ_{12}; maximum difference in magnitude: 0.30%

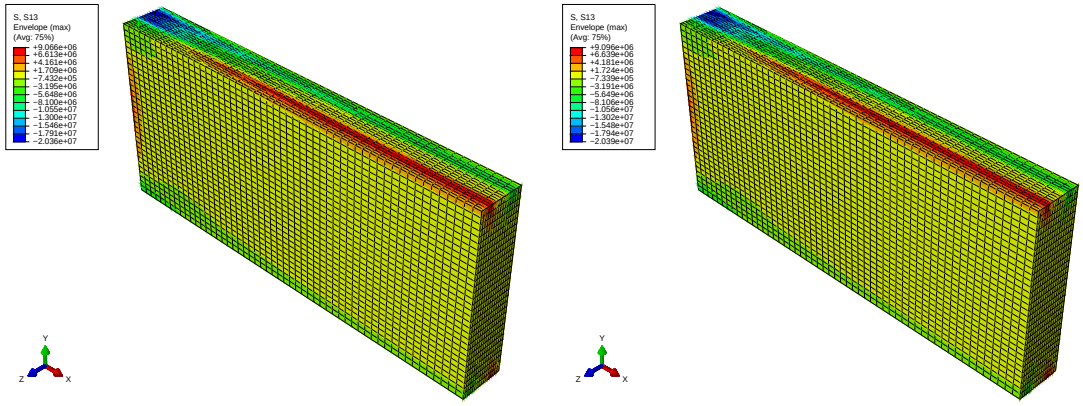

(a) Full 3D **(b)** Joined 3D/1D

Figure 3.7: Transverse shear stress, σ_{13}; maximum difference in magnitude: 0.30%

And lastly the results for shear stress, σ_{13}, are presented in Fig. 3.7. It can be verified from the figure that the joined model gives very good predictions for σ_{13}, and the error between these values and the results from full 3D analysis is very small.

3.2.2 Displacement Convergence

In order to study displacement convergence for the joined 3D/1D model and comparing it with that of full 3D FEA analysis, the same composite beams shown in Fig. 3.1 are considered in this section. Various mesh densities, from coarse to fine, are considered while both joined 3D/1D and full 3D models are loaded at the tip with a transverse shear force with a magnitude of 400 N in the z direction. In each case, mesh densities are the same in the 3D part of the joined model and the full 3D model. Also mesh density of the beam part is the same as the mesh density of the 3D part in the x direction.

Figures 3.9 and 3.10 present the tip displacement in x and z directions, respectively, versus number of elements in the 3D part. For the full 3D model, the displacements are evaluated at the center of the right end section of the beam. For the sake of clarity, the same results are presented on a logarithmic scale as well. It can be seen in the figures that the difference between the results decreases as the number of elements increases, such that for fine meshes the difference between the results becomes ignorable. This can be verified by inspecting Fig. 3.8 where the highest relative error between the joined 3D/1D and full 3D results is 0.4% corresponding to the displacement in the y direction, u_2. The largest displacement component corresponds to the z direction, u_3, where the difference is as low as 0.1%. The final displacement of the tip in that direction is equal to 0.119 m for both cases.

Although the results for the joined 3D/1D do not show significant differences, the simulation times for both cases differ drastically. Simulation times for both cases are presented in Table 3.2. It can be verified from the table that while the simulations

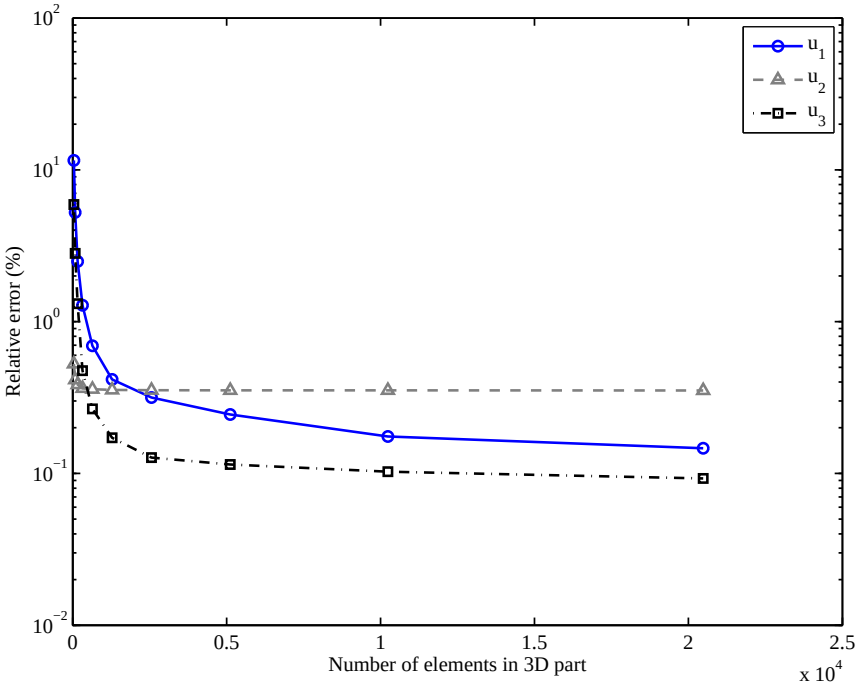

Figure 3.8: Relative error convergence for u_1, u_2, and u_3

for the full 3D model with a fine mesh takes 982 s to complete, the simulations for the joined 3D/1D model have been carried out in 182 s, which is 5.40 times as fast, without sacrificing too much accuracy, such that the final results for both cases are virtually the same. The time efficiency of the joined model should not come as a surprise as it is the direct result of having fewer DOF in the joined model; while, for the finest mesh, there are 102400 elements in the full 3D model, the joined 3D/1D model benefits form having only 20512 elements.

3.2.3 Eigenanalysis

Frequency analysis leads to a similar observation. The first 10 free-vibration frequencies of the beam are summarized in Table 3.3. Here, for the sake of brevity, only the final results for a fine mesh are presented. As can be seen in the table, results from the joined 3D/1D model are very close those of full 3D model. However, as in the case of static displacement analysis, the processing time required for the analysis is 5.74 times smaller for the joined model which is the direct result of smaller number of DOF for

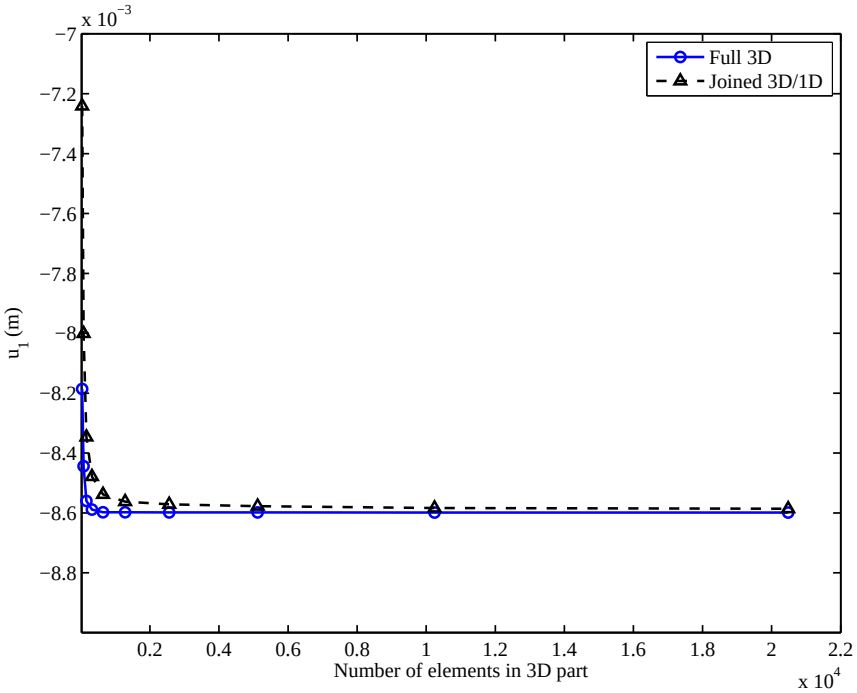

(a) Normal scale

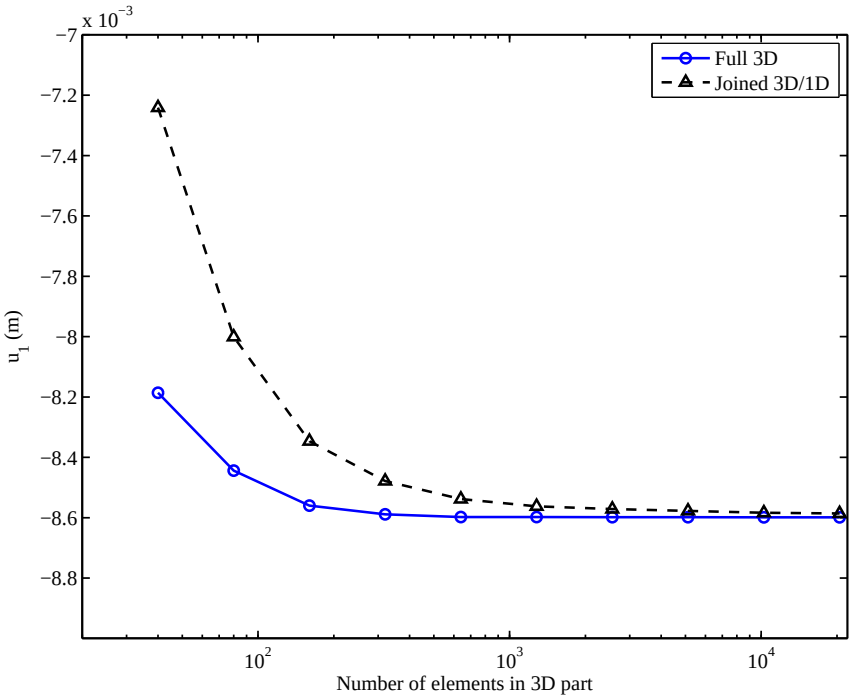

(b) Logarithmic scale

Figure 3.9: Displacement convergence for u_1

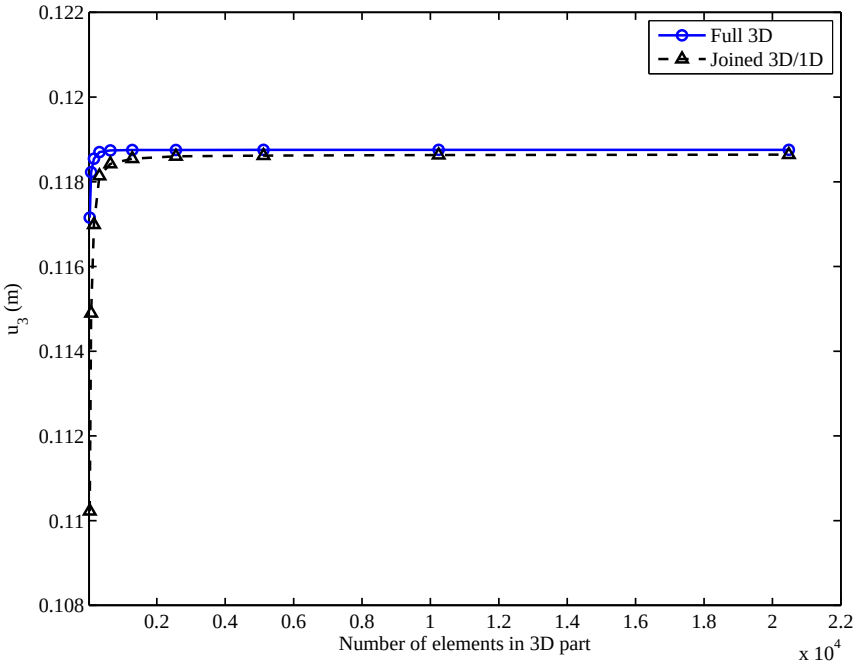

(a) Normal scale

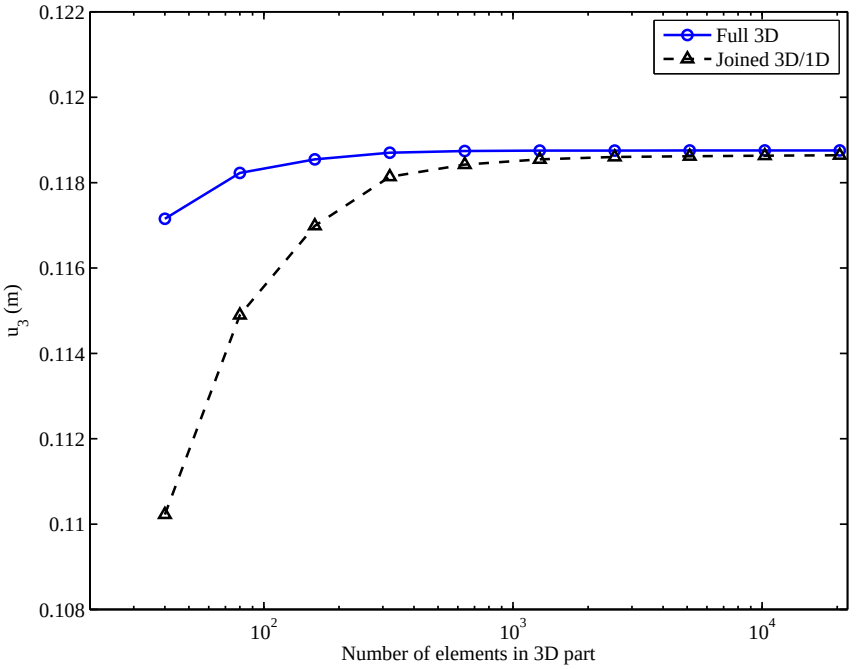

(b) Logarithmic scale

Figure 3.10: Displacement convergence for u_3

Table 3.2: Precessing times for the joined and full 3D models, same mesh density

Elements in 3D Part	Joined 3D/1D (s)	Full 3D (s)	Speedup factor
40	2	11	5.50
80	3	16	5.33
160	4	21	5.25
320	11	59	5.36
640	18	95	5.28
1280	33	172	5.21
2560	55	294	5.34
5120	88	446	5.07
10240	124	646	5.21
20480	182	982	5.40

the joined 3D/1D model.

3.3 Crack Growth Analysis Using XFEM

An important aspect, that determines the stress distribution, is how the crack is loaded. There are three different pure loading modes, opening in tension Mode I, in-plane shear Mode II and transverse shear Mode III. The different loading modes are illustrated in Figure 3.11.

Extended Finite Element Method (XFEM) allows the discontinuity in the FE solution by using enrichment functions [122]. It has gained popularity for crack growth analysis due to the ease of modeling since there is no need to predefine the crack growth path. Also it is not required to re-mesh the crack growth region during the analysis. In the present work, XFEM has been employed to model and analyze existing chord-wise cracks on the HALE aircraft wings.

In order to show the validity of an XFEM analysis using the joined 3D/1D method, an edge crack is embedded inside the 3D part of the beam structure studied in the previous section. As the loading increases, the crack was allowed to propagate and the results are obtained at the end of the load step. Figs. 3.12 to 3.17 compare

Table 3.3: Natural frequencies of the joined 3D/1D and full 3D models

Mode num.	Joined 3D/1D (rad/s)	Full 3D (rad/s)	Relative error (%)
1 M_y	73.96	73.94	0.03
2 M_z	288.65	288.51	0.05
3 M_y	463.24	462.64	0.14
4 M_y	1297.10	1295.90	0.09
5 M_z	1789.22	1787.90	0.07
6 M_y	2546.58	2543.32	0.13
7 M_x	2619.38	2617.74	0.06
8 M_y	4113.53	4111.08	0.06
9 M_z	4934.33	4923.49	0.21
10 M_x	5723.29	5717.71	0.10
	Joined 3D/1D (s)	Full 3D (s)	Speedup factor
Wallclock Time	38	219	5.74

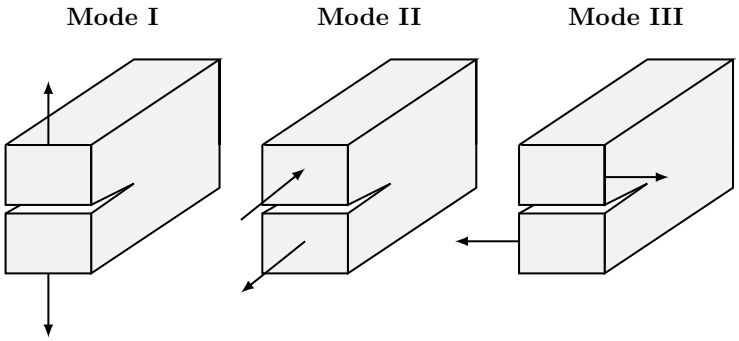

Figure 3.11: Crack opening modes

between both the joined 3D/1D model and full 3D model, the distributions of all stress components, $\sigma_{ij};\ i,j = 1,2,3$, around the crack region. It can be seen in the figures that, the difference between the 3D/1D results and full 3D results are quite negligible and the joined model has been able to predict the same crack growth pattern and stress distribution as the full 3D model. The simulation time, however, shows a marked difference. While the full 3D model requires 12232 s to carry out the simulation, the joined 3D/1D method can deliver similar results in 2308 s, which is about 5.3 times as fast.

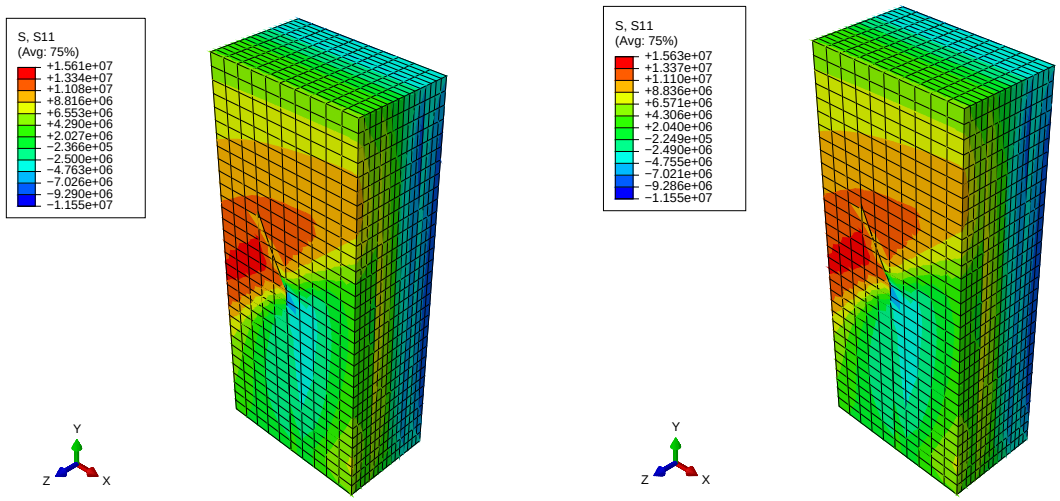

(a) Full 3D **(b)** Joined 3D/1D

Figure 3.12: Normal stress distribution, σ_{11}, around the crack

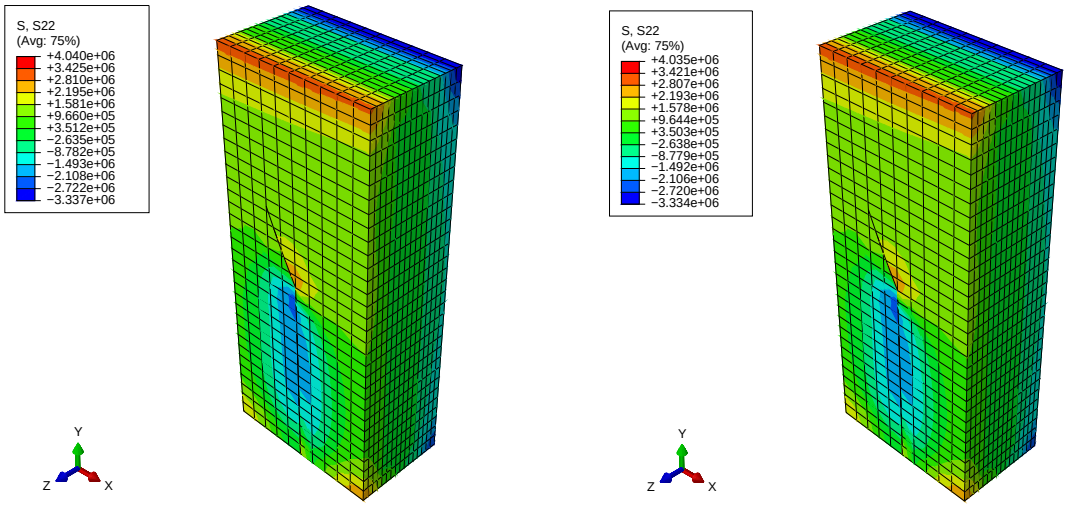

(a) Full 3D **(b)** Joined 3D/1D

Figure 3.13: Normal stress distribution, σ_{22}, around the crack

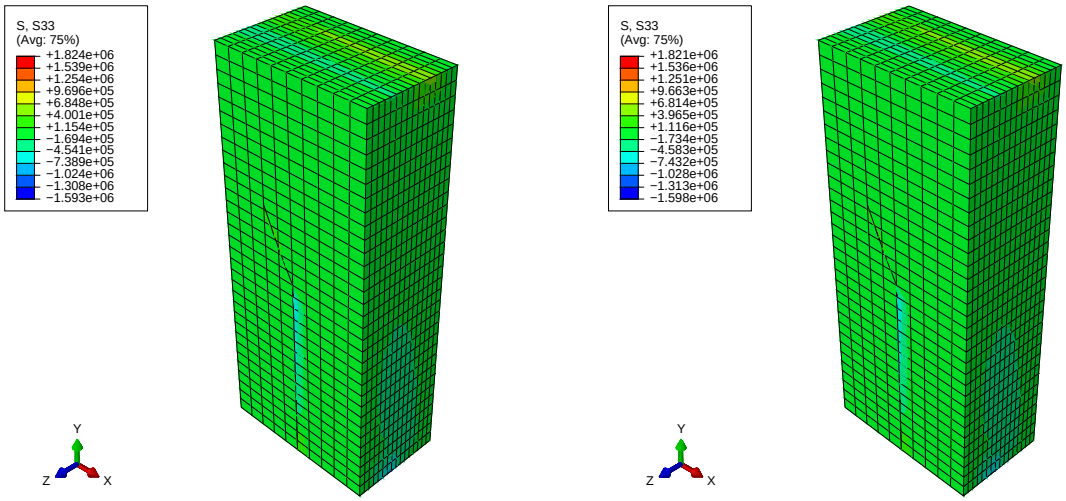

(a) Full 3D **(b)** Joined 3D/1D

Figure 3.14: Normal stress distribution, σ_{33}, around the crack

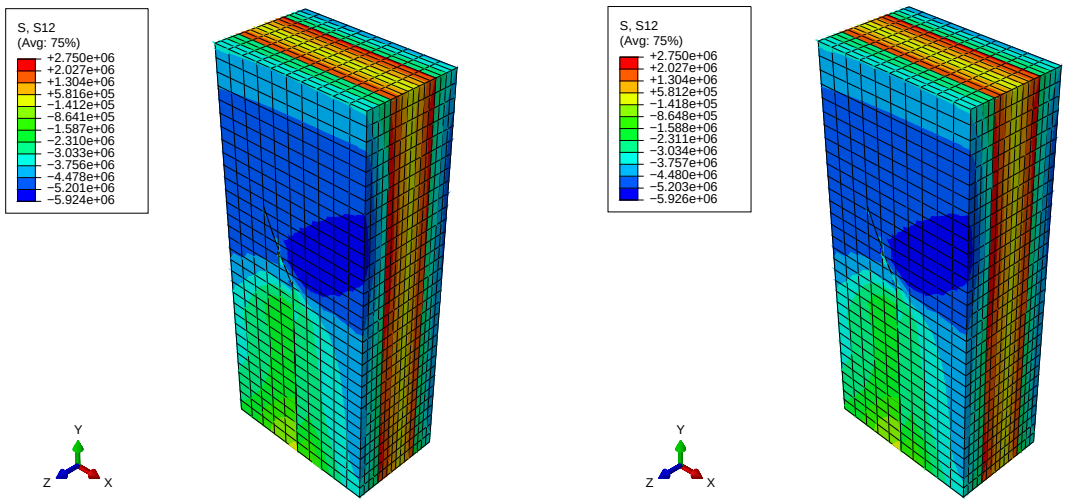

(a) Full 3D **(b)** Joined 3D/1D

Figure 3.15: Shear stress distribution, σ_{12}, around the crack

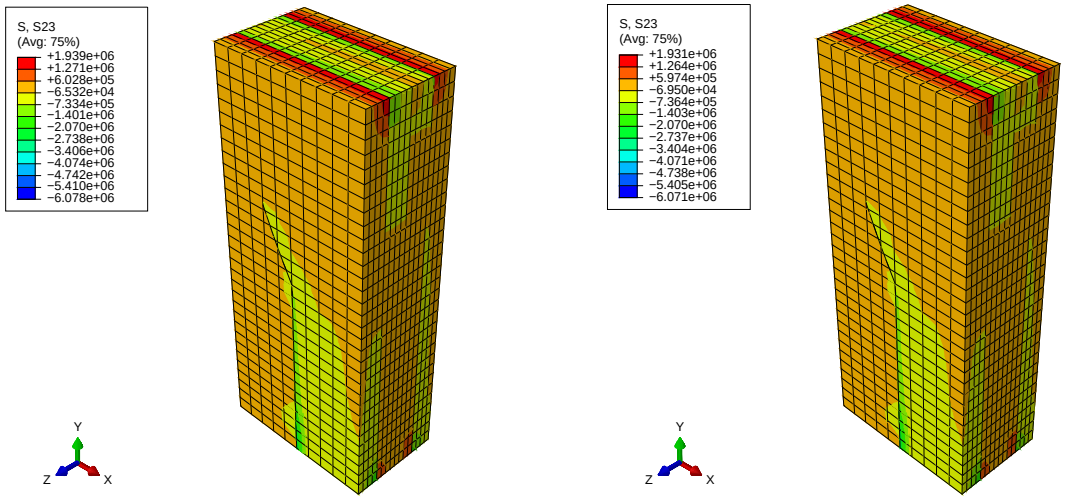

(a) Full 3D **(b)** Joined 3D/1D

Figure 3.16: Shear stress distribution, σ_{23}, around the crack

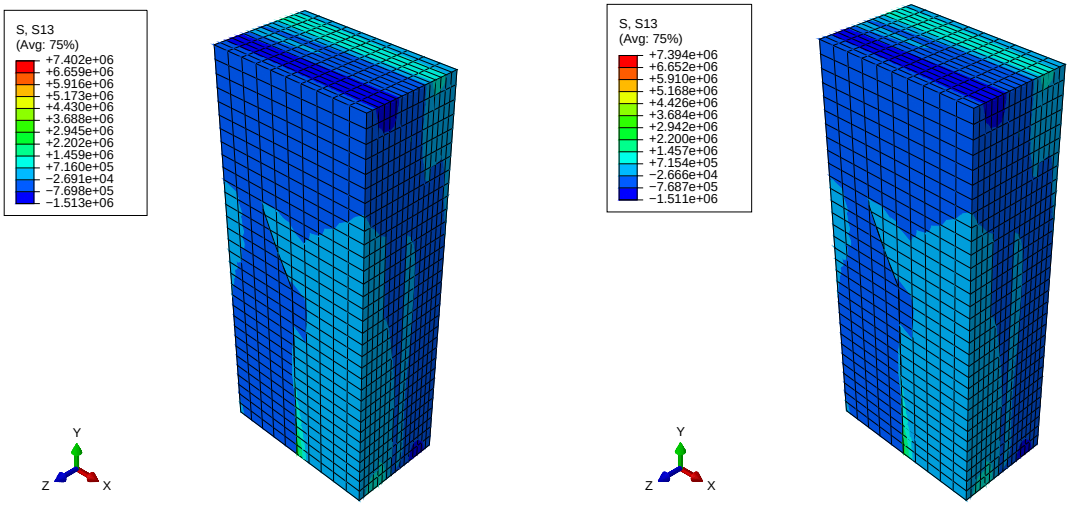

(a) Full 3D **(b)** Joined 3D/1D

Figure 3.17: Shear stress distribution, σ_{13}, around the crack

3.4 Delamination Analysis Using Cohesive Elements

Inter-laminar delaminations in composite wings can be properly modeled and analyzed using cohesive elements [123–125]. While they allow a detailed modeling of cohesive connections, they are not limited to crack propagation for existing cracks; crack initiation can also be modeled and analyzed. However, the crack can only propagate in a predefined direction, i.e., along the cohesive layer.

A layered composite beam, clamped at one end and loaded by a transverse tip load, with a skin attached to the beam near the root is chosen for the skin delamination analysis. The rectangular cross section has the dimensions of 0.02 m by 0.08 m and the beam has a total length of 1 m, of which only 0.2 m is modeled as 3D in the joined model. The full 3D and joined 1D/3D models are shown in Fig. 3.18. A thin cohesive layer between the skin and the body is modeled using the COH3D8 element. Damage initiation criterion is based on quadratic nominal stress as [124]

$$\left(\frac{\langle\sigma_I\rangle}{\sigma_{max_I}}\right)^2+\left(\frac{\sigma_{II}}{\sigma_{max_{II}}}\right)^2+\left(\frac{\sigma_{III}}{\sigma_{max_{III}}}\right)^2=1, \tag{3.1}$$

where σ_i $i=I,II,III$, are nominal stresses in the mode i, and

$$\langle\sigma_I\rangle=\begin{cases}\sigma_I & \text{for} \quad \sigma_I>0,\\ 0 & \text{for} \quad \sigma_I<0.\end{cases} \tag{3.2}$$

Constitutive behavior of the cohesive layer follows traction-separation rule, with the mixed-mode fracture obeying the power law [124]

$$\left(\frac{G_I}{G_{I_c}}\right)^\alpha+\left(\frac{G_{II}}{G_{II_c}}\right)^\alpha+\left(\frac{G_{III}}{G_{III_c}}\right)^\alpha=1, \tag{3.3}$$

where G_i $i=I,II,III$, are fracture energies for the mode i. The properties of the cohesive layer are listed in Table 3.4. It is assumed that no initial damage exists in

Table 3.4: Physical properties of the cohesive layer [123]

E	8.5×10^8 N/m^2
σ_{max_I}	3.3×10^6 N/m^2
$\sigma_{max_{II}} = \sigma_{max_{III}}$	7.0×10^6 N/m^2
G_{I_c}	330 N/m
$G_{II_c} = G_{III_c}$	800 N/m

the beam. However, the damage will initiate and propagate along the cohesive layer.

Figure 3.19 shows the maximum principal strain distribution in the cohesive layer after the damage was initiated. As it can be seen in the figures, for both models 7 elements failed and therefore no longer carry any load. With increasing the tip deflection and the resulting stress, more elements will fail such that at the end of the simulation, 447 elements failed in both models, shown in Fig. 3.20. The same is true about mid and minimum principal strains distributions, depicted in Figs. 3.21 through 3.24. It should be noted from Figs. 3.21 and 3.22 that the mid principal strains would indeed vanish, which demonstrates the state of plane strain for the cohesive layer. This is anticipated as the cohesive layer is very thin.

Moreover, the principal strain components for the skin are presented in Figs. 3.25 through 3.27 which associates with the onset of damage formation. The figures also show very good agreement between the results for the full 3D model and the joined 3D/1D model. However, the simulation times are drastically different. While for the full 3D model the simulation takes 4848 sec to complete, the required time for the joined model is only 865 sec which is more than 5.6 times faster. The simulation for the joined model can be made even faster, compared with the full 3D model, were a smaller area chosen for the solid part in the joined model.

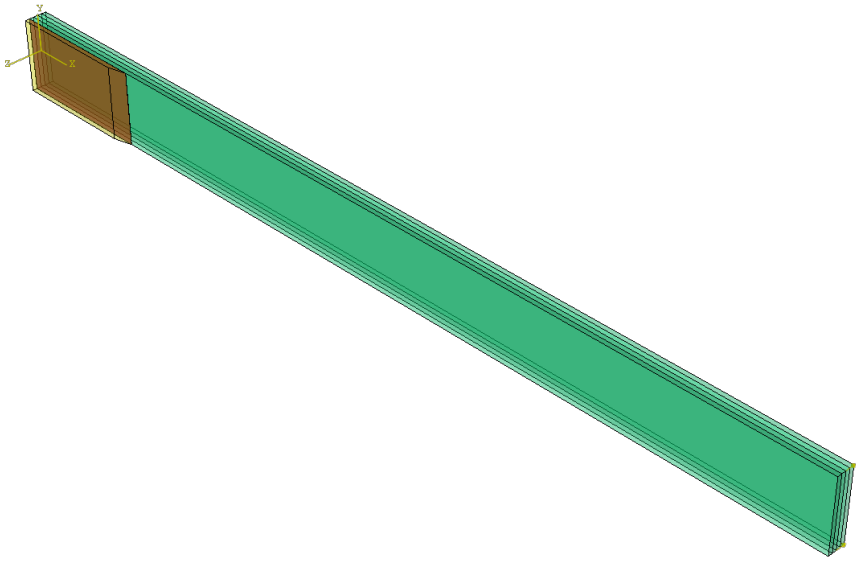

(a) Full 3D

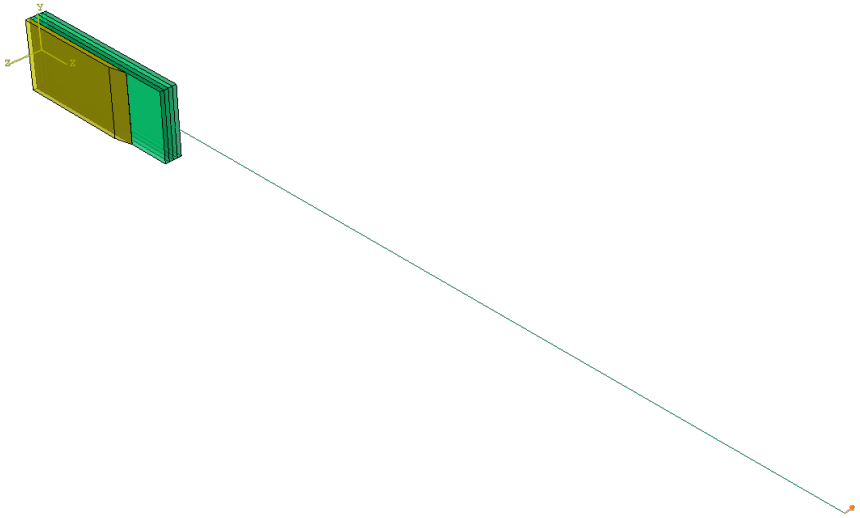

(b) Joined 3D/1D

Figure 3.18: Cantilever composite beam for skin delamination

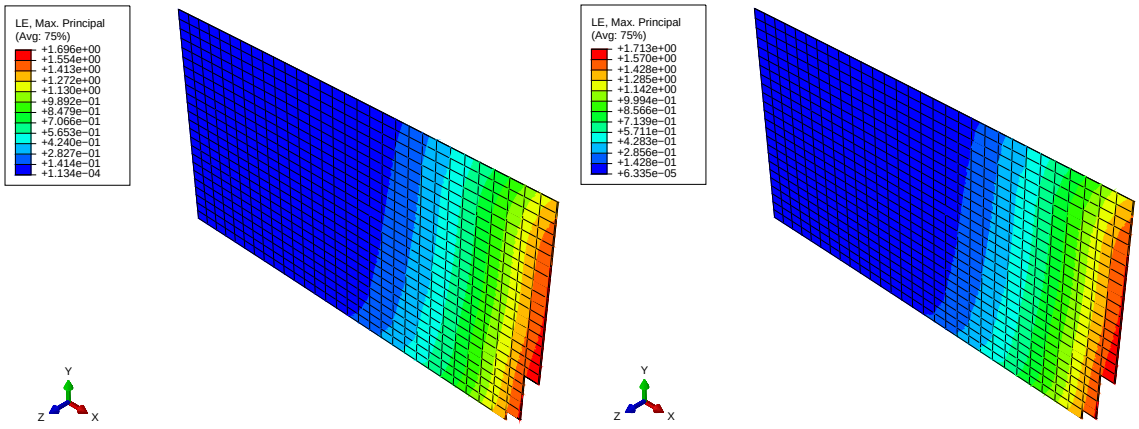

(a) Full 3D **(b)** Joined 3D/1D

Figure 3.19: Maximum principal strain in the cohesive layer after damage initiation

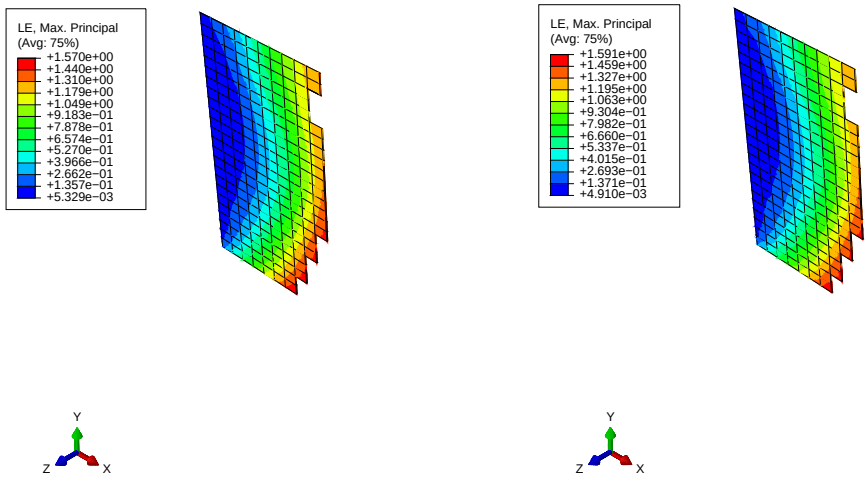

(a) Full 3D **(b)** Joined 3D/1D

Figure 3.20: Maximum principal strain in the cohesive layer at the end of load step

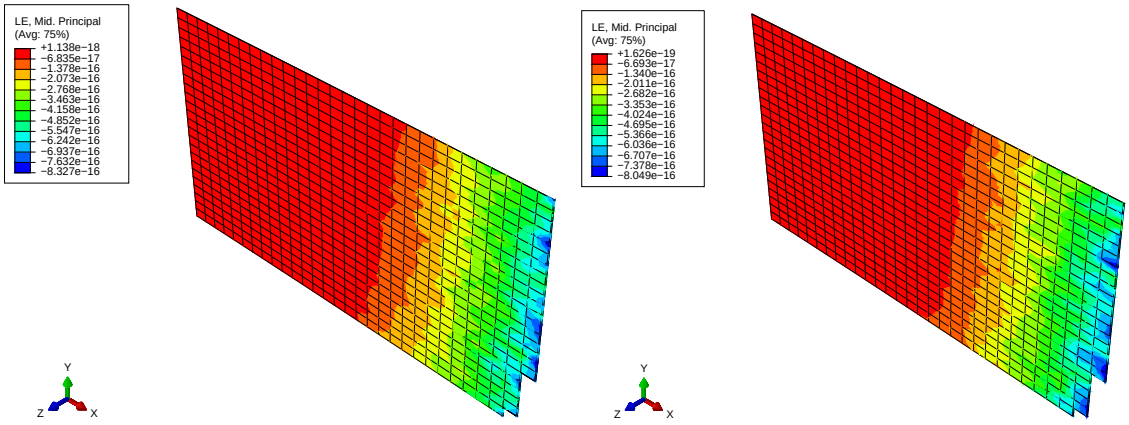

(a) Full 3D **(b)** Joined 3D/1D

Figure 3.21: Mid principal strain in the cohesive layer after damage initiation

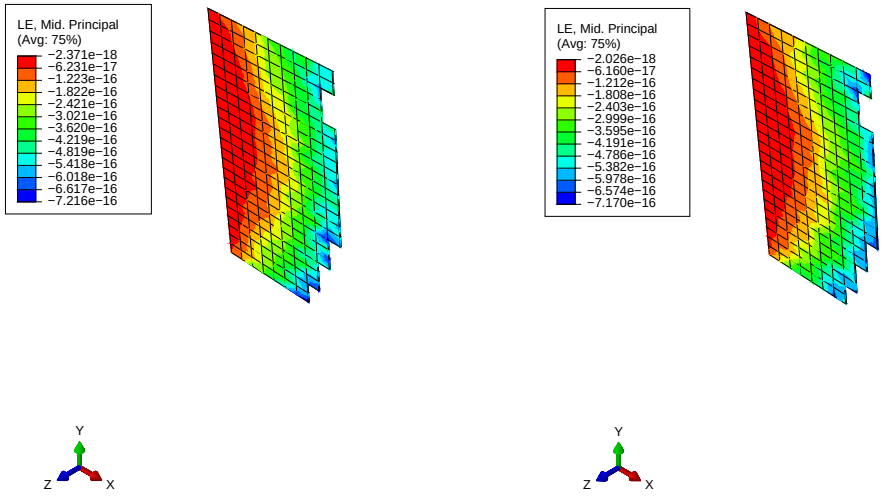

(a) Full 3D **(b)** Joined 3D/1D

Figure 3.22: Mid principal strain in the cohesive layer at the end of load step

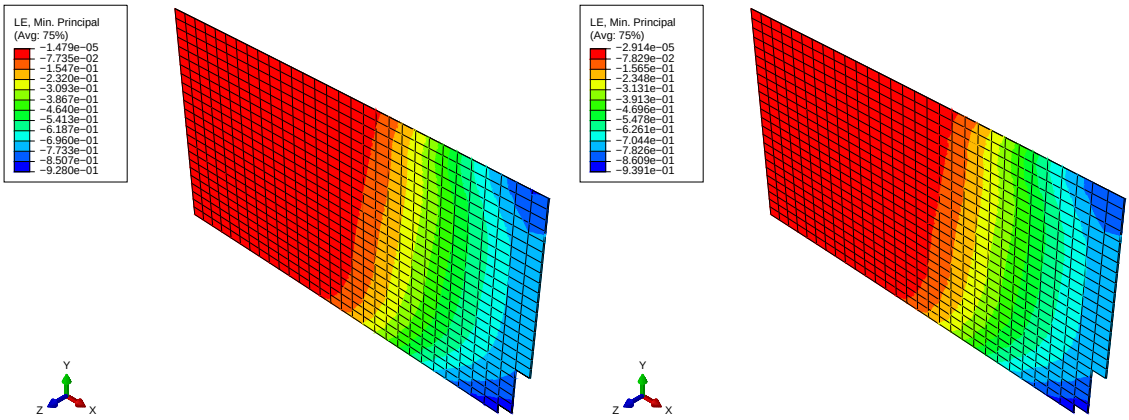

(a) Full 3D **(b)** Joined 3D/1D

Figure 3.23: Minimum principal strain in the cohesive layer after damage initiation

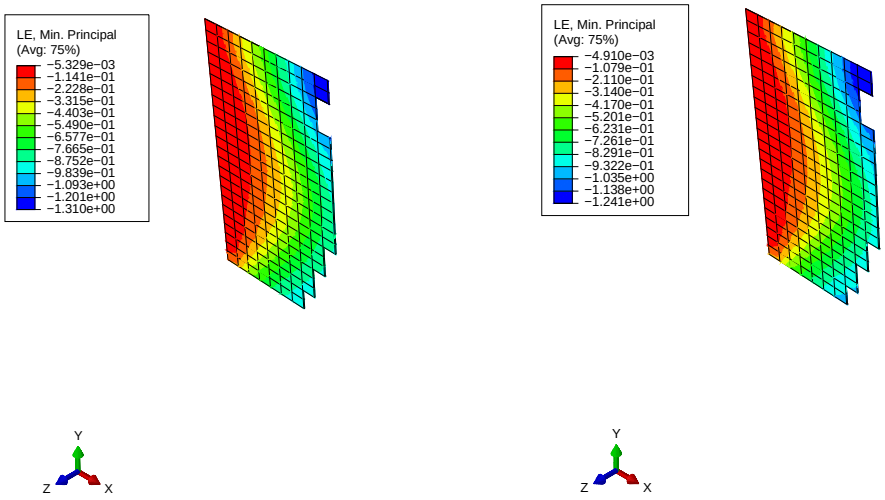

(a) Full 3D **(b)** Joined 3D/1D

Figure 3.24: Minimum principal strain in the cohesive layer at the end of load step

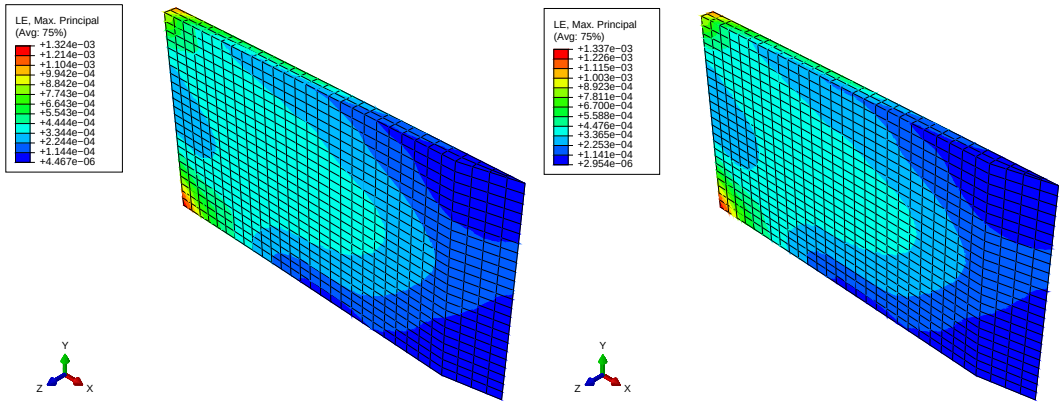

(a) Full 3D **(b)** Joined 3D/1D

Figure 3.25: Maximum principal strain in the skin after damage initiation

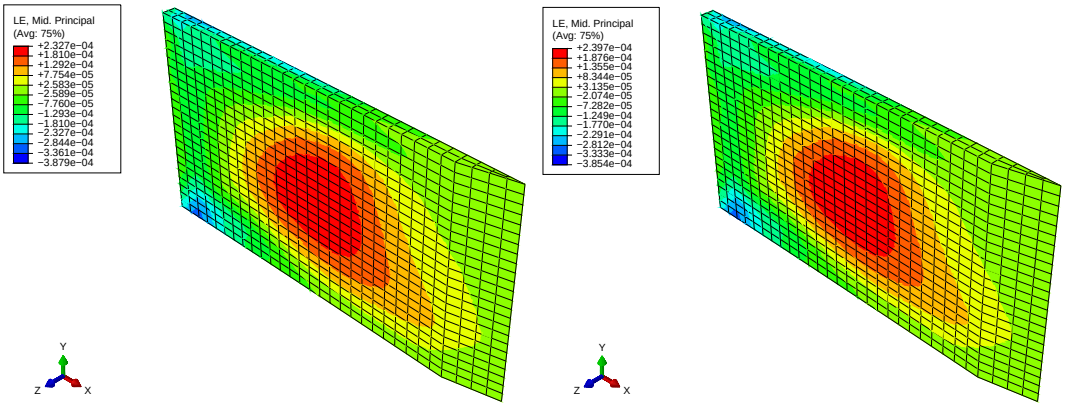

(a) Full 3D **(b)** Joined 3D/1D

Figure 3.26: Mid principal strain in the skin after damage initiation

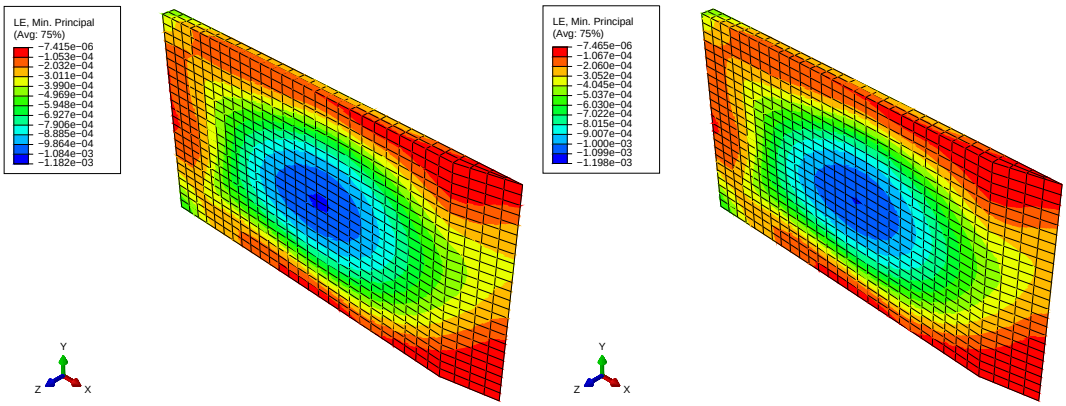

(a) Full 3D **(b)** Joined 3D/1D

Figure 3.27: Minimum principal strain in the skin after damage initiation

CHAPTER IV

AEROELASTIC ANALYSIS OF HIGH $\mathcal{AR}$ WINGS

4.1 Introduction

In order to use the solving and post-processing capabilities of commercial software and expand the applicability of the method, the geometrically exact beam model is coupled with Peters' unsteady aerodynamic theory, summarized in the section 2.2, and has been coded with C++ programing language into a nonlinear user element. The element was integrated to a commercial FEA tool, namely, ABAQUS. Therefore, ABAQUS users can utilize the model for nonlinear static analysis as well as eigen-analysis and nonlinear time marching. Here, all simulations are carried out on a Windows-7 machine with Core-i5, 3.4 GHz CPU and 8 GB of RAM.

In this study, the structure is cantilevered at one end with no rigid body motion to represent a wind-tunnel model of the wing. Therefore, the far-field air flows at a steady angle of attack with a certain velocity with respect to the wing. The user element receives as its input the flow velocity and root angle of attack. In order to study the nonlinear aeroelastic behavior of a wing, multiple time simulations are performed. For a given altitude and steady angle of attack, the simulation starts with a fairly low airspeed, with the wing at rest. If after a few seconds of time simulation the resulting oscillations are damped and wing achieves steady-state condition, then the simulation restarts with a higher flow velocity. The procedure continues until the perturbations are not damped. The flutter boundary is characterized as the lowest velocity at which the wing oscillations are not damped any more. In this situation, the velocity corresponds to the nonlinear flutter velocity, and the frequency of the oscillation defines the nonlinear flutter frequency.

Table 4.1: Aerodynamic and structural properties of Goland wing [93]

Length	20 ft
Aerodynamic chord, $\overline{c}$	6 ft
Mass	0.746 slugs/ft
Radius of gyration about c.g.	0.25 $\overline{c}$
c.g. location	0.43 $\overline{c}$
a.c. location	0.25 $\overline{c}$
Bending stiffness	2.36×10^7 lb-ft^2
Torsional stiffness	2.39×10^6 lb-ft^2
Elastic axis location	0.33 $\overline{c}$
Lift-curve slope	2π
Air density	2.188×10^{-3} slugs/ft^3

4.2 Validation of the Nonlinear Aeroelastic Element

In order to validate the aeroelastic element, two different wings have been studied. The first case is the classical Goland wing [28] which has a moderate $\mathcal{AR}$ and stiffness, making it suitable for linear aeroelastic analysis. The aerodynamic and structural properties of the wing are given in Table 4.1. Twenty linear elements are used to spatially discretize the wing. The time histories of the wing-tip displacement and twist for Goland wing at different flow velocities are shown in Figure 4.1. As it can be seen in the figure, for a velocity of 440 ft/s the oscillations are damped out which is in contrast with that of the velocity of 450 ft/s. The undamped response, at $V_\infty = 446$ ft/s, specifies the flutter condition. The flutter characteristics for the Goland wing are summarized in Table 4.2 and compared with the results available in the literature. It can be verified that both the flutter velocity and the flutter frequency agree well with the published literature and the difference between the results are negligible.

The second case considered is a HALE wing presented by Patil [93]. The properties of the wing are listed in Table 4.3. Unlike the Goland wing, this wing is a slender, high $\mathcal{AR}$ wing which can undergo large deformation. This would enable us to perform nonlinear time-marching and post-flutter analysis. The wing's structure is discretized

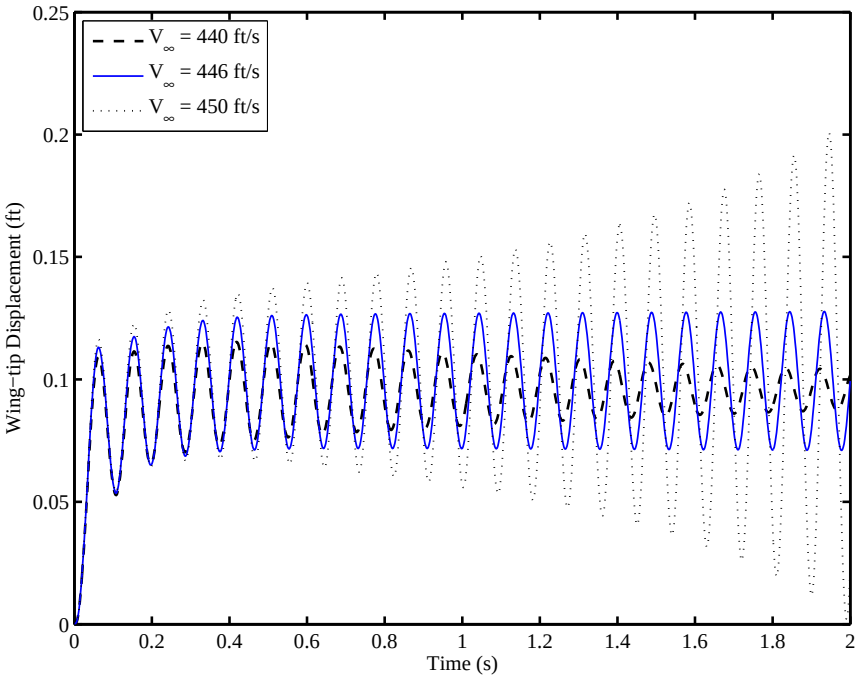

(a) Wing-tip displacement

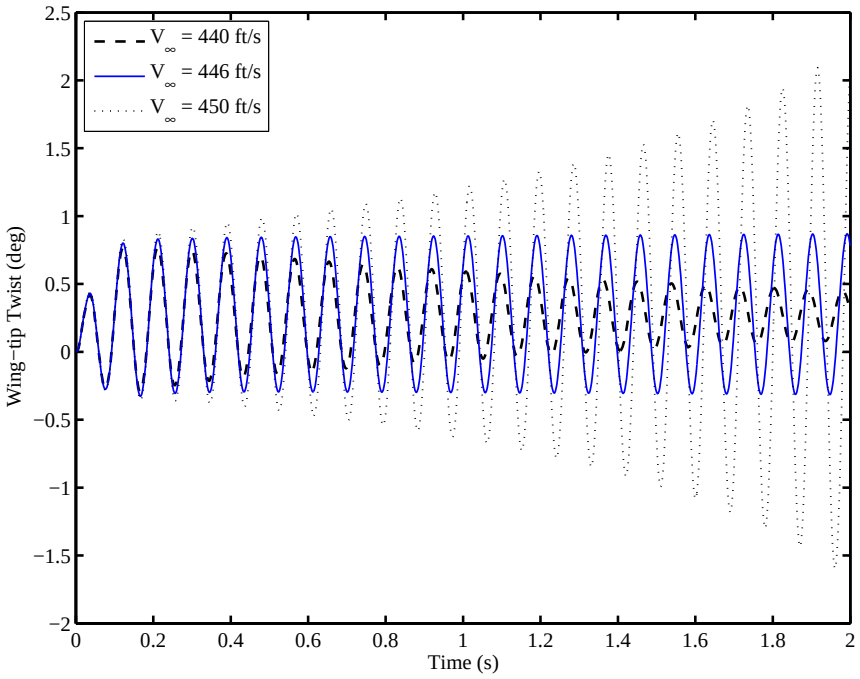

(b) Wing-tip twist

Figure 4.1: Wing-tip displacement and twist for Goland wing

Table 4.2: Flutter boundaries of Goland wing

	Present analysis	Goland and Luke [28]	Patil [93]
Flutter velocity	446 ft/s	445 ft/s	445 ft/s
Flutter frequency	69.8 rad/s	70.7 rad/s	70.2 rad/s

Table 4.3: Aerodynamic and structural properties of HALE wing [93]

Length	16 m
Mass	0.75 kg/m
Mass polar moment of inertia	0.1 kg.m^2/m
Torsional stiffness	1.0×10^4 N.m^2
Flapwise bending stiffness	2.0×10^4 N.m^2
Chordwise bending stiffness	4.0×10^6 N.m^2
Elastic axis location	0.5 $\bar{c}$
c.g. offset from elastic axis	0.25 $\bar{c}$
a.c. offset from elastic axis	0.25 $\bar{c}$
Aerodynamic chord, $\bar{c}$	1 m
Lift-curve slope	2π
Air density	0.0889 kg/m^3

in space using sixteen element. Proceeding similar to the Goland wing, the nonlinear time-marching starts with a low flow velocity with the wing at rest. After a few runs, at a certain velocity, the oscillations were not damped anymore. Beyond the flutter speed, however, the large deformations and the resulting geometric stiffness effects do not allow the oscillation to grow and the oscillations settle into a stable limit cycle. The wing-tip displacement and twist are shown in Figure 4.2 for $V_\infty = 25.0$ m/s, highlighting the post-flutter response of the HALE wing. To demonstrate the validity of the results, the same analysis has been done using DYMORE software and the results are compared in the same figure. Very similar behavior can be observed for $V_\infty = 25.2$ m/s. Large displacements are noticeable as the wing-tip oscillates between 1.88 m and 2.62 m, more than 16% of the wing length.

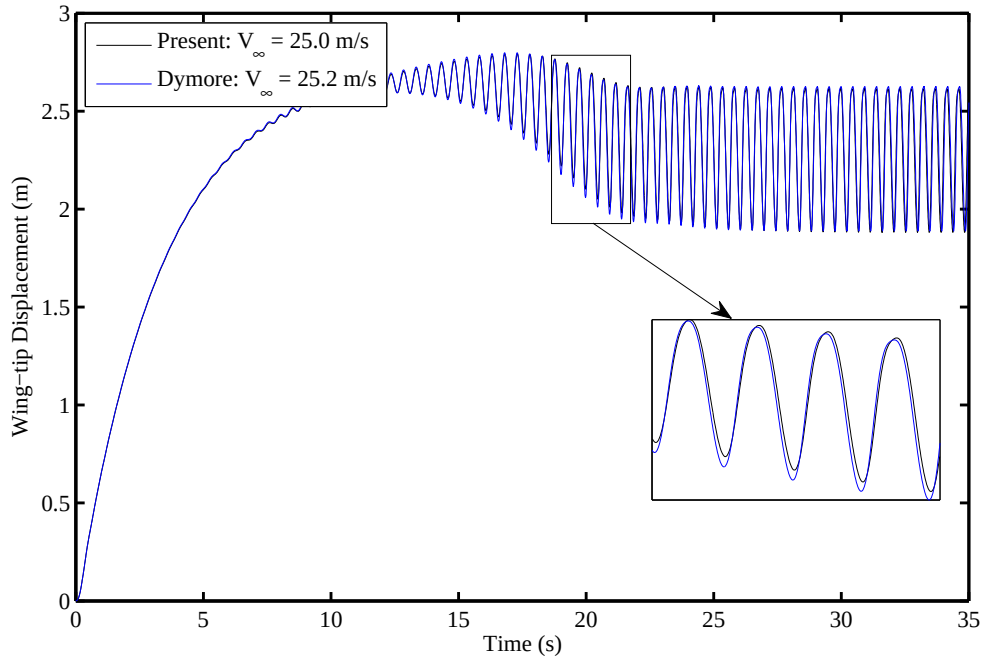

(a) Wing-tip displacement

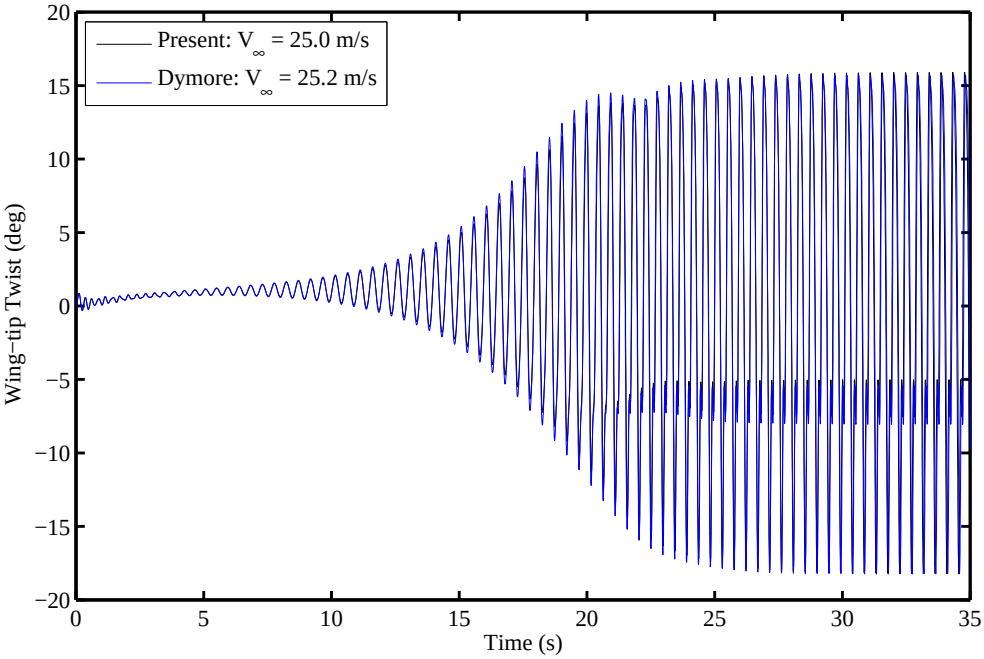

(b) Wing-tip twist

Figure 4.2: Wing-tip displacement and twist for HALE wing

4.3 Linear Aeroelastic Analysis Using Joined 3D/1D Model

For the joined 1D/3D analysis, a layered composite beam with a rectangular cross-section is considered. The dimensions and aerodynamic properties of the wing are the same as those listed in the Table 4.3. However, the cross sectional properties, found from VABS, are different. The beam section is made of three graphite-epoxy layers the material properties of which are listed in Table 4.4 [30].

Table 4.4: Properties of Laminates

Material properties	
E_1	2.06×10^{11} N/m^2
$E_2 = E_3$	5.17×10^{9} N/m^2
G_{12}	3.10×10^{9} N/m^2
$G_{13} = G_{23}$	2.55×10^{9} N/m^2
$\nu_{12} = \nu_{23} = \nu_{13}$	0.25
Layup	
Symmetric	[β°/0°/β°]
Antisymmetric	[β°/0°/-β°]

Figure 4.3 shows the layup arrangement for the composite wing. Each of the top and the bottom layers have 15 mm thickness, and the thickness of the mid layer is 10 mm. The symmetric 6×6 sectional stiffness matrix, $S = S_{ij};\ i, j = 1, 2, \ldots, 6$, is diagonal for an isotropic, prismatic beam with the beam axis located at the shear center. However, for anisotropic and layered composite beams, depending on the layering pattern, different stiffness coupling terms will appear in the stiffness matrix. Layered cross sections may be categorized in two major groups: *i)* symmetric layup and *ii)* antisymmetric layup. Stiffness matrices for both categories are no longer diagonal. For the antisymmetric layup the major stiffness couplings are extension-twist coupling and shear-bending coupling. On the other hand, a symmetric layup results in coupling between twist and bending. Normalized sectional stiffness properties

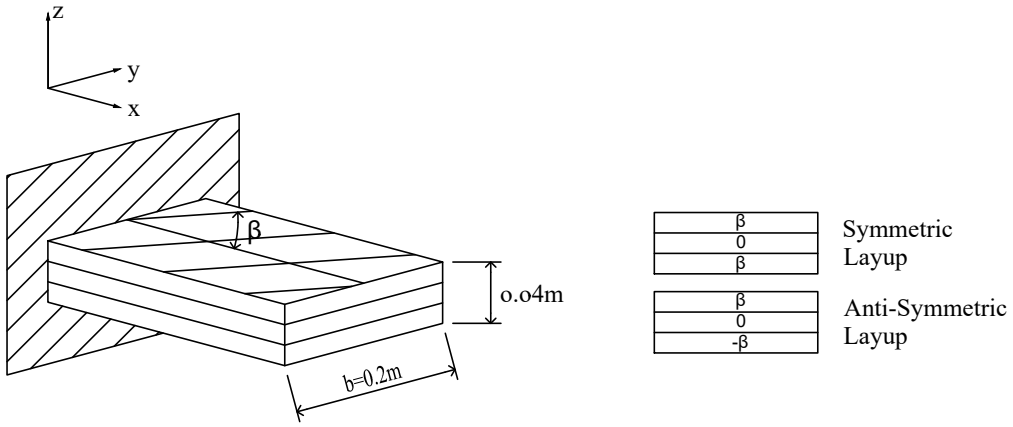

Figure 4.3: Composite wing layup

for both symmetric and antisymmetric layups with layup angle, β, between -90° and +90° are found using VABS and shown in Figs. 4.4 and 4.5, respectively. Each stiffness value is normalized with respect to the maximum of the prospective property, listed in Table 4.5. Other values that are not listed in the table would vanish for all layups.

Table 4.5: Maximum value of sectional properties, N-m^2

	Symmetric layups	Antisymmetric layups
S_{11}	1.65×10^9	1.65×10^9
S_{22}	7.80×10^7	1.20×10^8
S_{33}	1.72×10^7	1.74×10^7
S_{44}	4.61×10^4	5.30×10^4
S_{55}	2.20×10^4	2.18×10^4
S_{66}	5.49×10^6	5.49×10^6
S_{41}	0.00	4.22×10^6
S_{52}	0.00	2.87×10^6
S_{63}	0.00	1.11×10^4
S_{46}	5.82×10^4	0.00

4.3.1 Linear Divergence Analysis

To study the effect of crack location on the divergence boundaries, a wing with orthotropic layup, i.e., $\beta = 0°$, is considered in this section. The chord-wise crack extends from the leading edge with three different crack to chord length ratios, a/b,

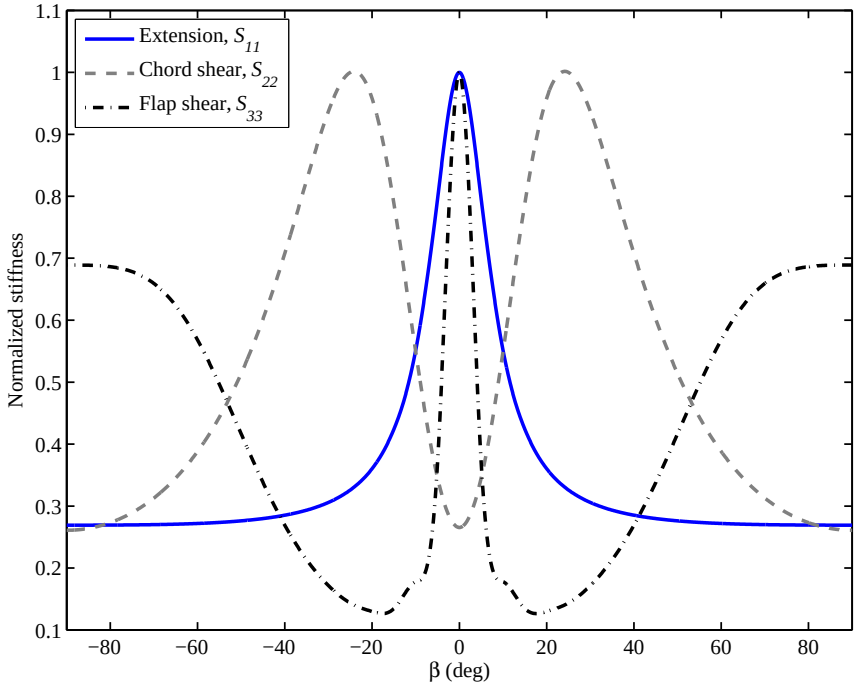

(a) Extension and shear

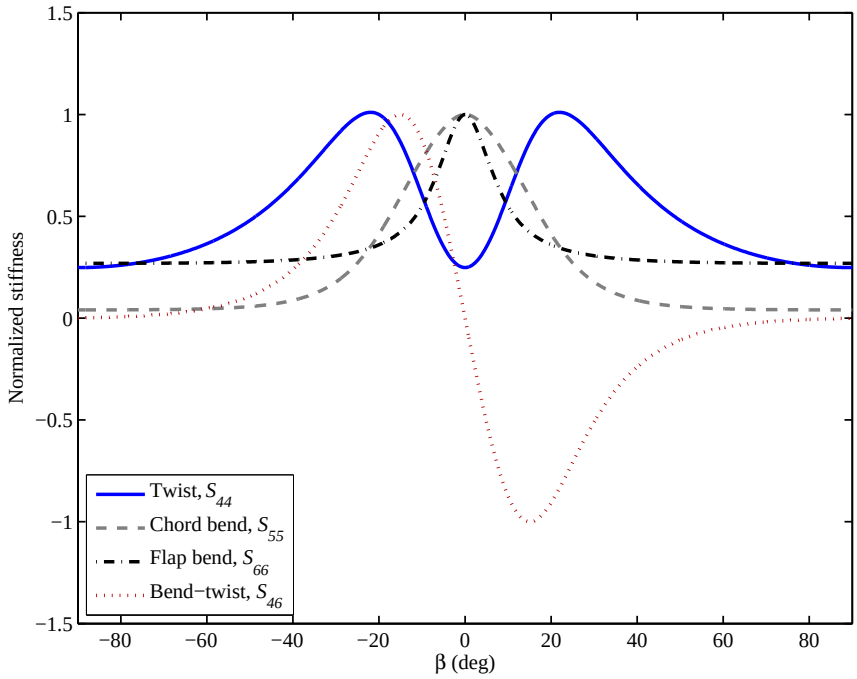

(b) Bending, twist, and couplings

Figure 4.4: Sectional stiffness properties for various symmetric layups

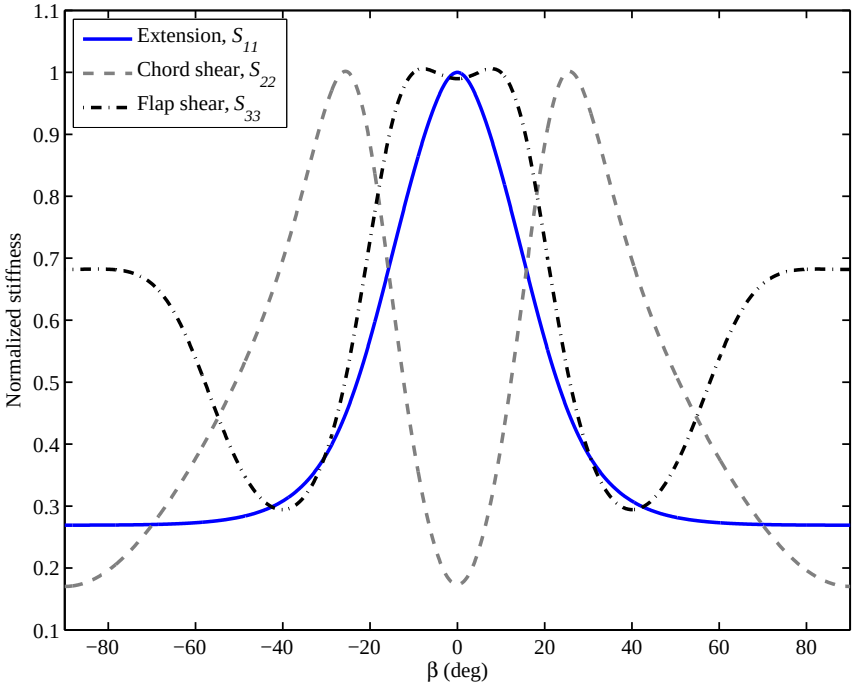

(a) Extension and shear

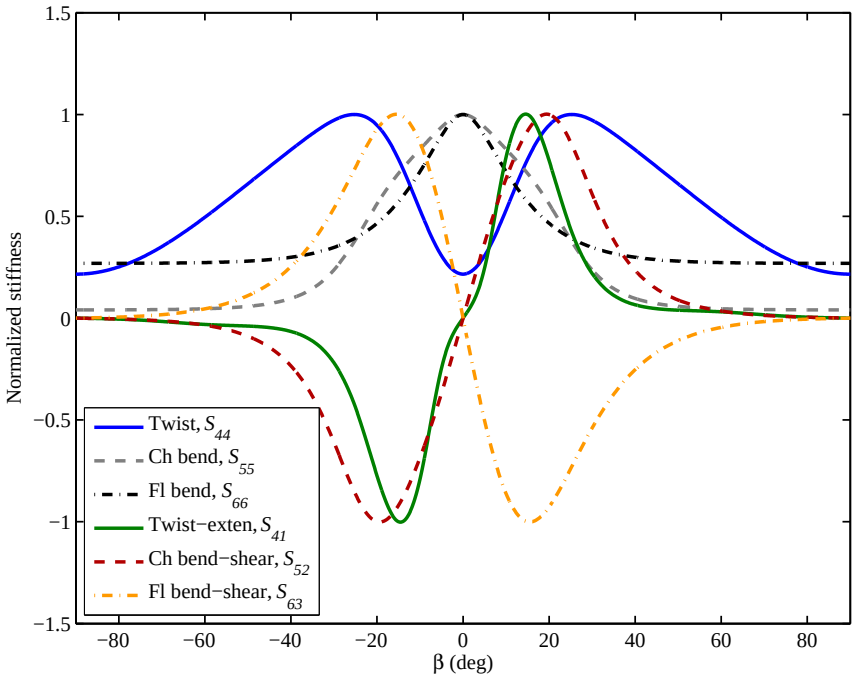

(b) Bending, twist, and couplings

Figure 4.5: Sectional stiffness properties for various antisymmetric layups

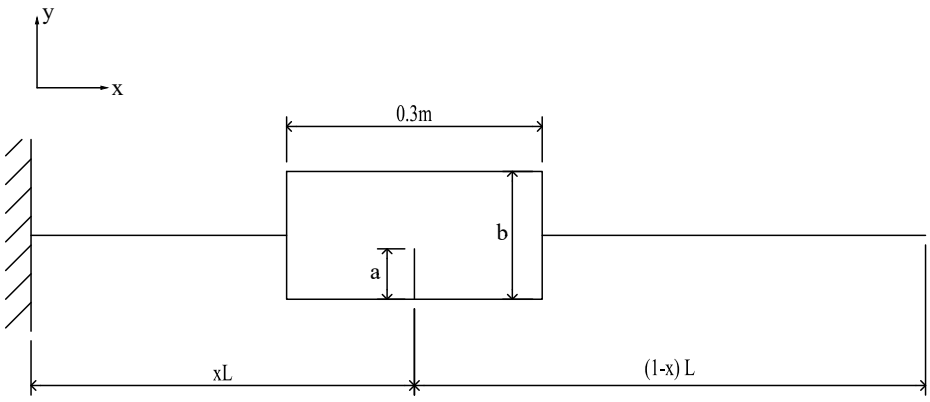

Figure 4.6: Chord-wise crack location along the span; side view

equal to 0.1, 0.2, and 0.3. The crack location varies along the span from $0.05L$ to $0.95L$, as shown in Fig. 4.6. Of the 16 m of the wing span, only 0.5 m of the wing surrounding the crack is modeled using full 3D solid elements, and the rest of the beam is modeled with 1D elements. The divergence boundary is then found by solving an eigenvalue problem whose lowest eigenvalue gives the divergence dynamic pressure. The results of the analysis for chord-wise cracks at the leading edge of the wing, with varying location along the span, are presented in Fig. 4.7. The results are normalized with respect to the divergence dynamic pressure of the undamaged wing, which is found to be equal to 70.14 $\mathrm{N/m^2}$.

Figure 4.7 shows that the larger cracks near the wing-root have a more significant effect on the divergence. It can be seen from the figure that a crack with $a/b = 0.3$ located at $0.05L$ will decrease the divergence dynamic pressure by about 10.1%, whereas the crack with $a/b = 0.1$ will reduce it by 4.5%. The effect of the intermediate case, $a/b = 0.2$, lies between those of the other two. The figure also shows that the effect of a crack on the divergence boundary fades away as the crack moves towards the wing-tip such that for the cracks located at $0.90L$ the divergence dynamic pressures for all three cases are very close to that of the undamaged wing. A similar analysis for trailing edge cracks was carried out which ended up with the same results.

A parametric study of the effects of damage on the divergence boundary of the

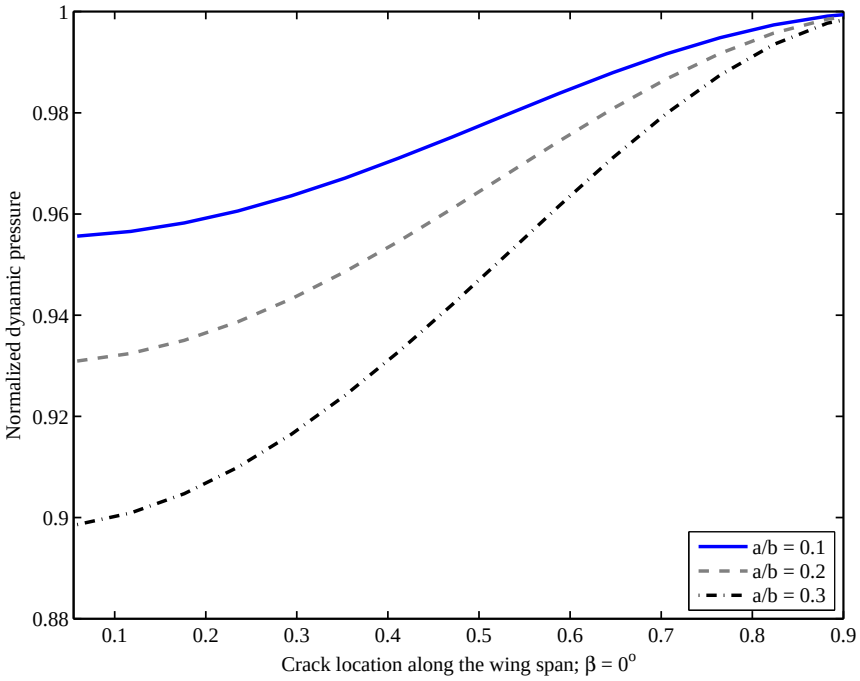

Figure 4.7: Divergence boundaries for varying crack locations along the span

wing with different layup arrangement is also instrumental. Normalized divergence and flutter dynamic pressures with respect to the laminate angles for both antisymmetric and symmetric layups are shown in Figs. 4.8 and 4.9, respectively. All chord-wise cracks at the leading edge are located at $0.05L$ which, based on the Fig. 4.7, reduces the divergence dynamic pressure the most. The dynamic pressures are normalized with respect to that of the baseline layup, i.e., $\beta = 0°$.

Figure 4.8 shows that the divergence dynamic pressure exhibits symmetry about $\beta = 0°$. This is in agreement with the results reported in Ref. [126]. It can be seen in the figure that arranging the layup antisymmetrically can significantly expand the divergence boundary such that when β is equal to $\pm 35°$, the divergence dynamic pressure is 3.82 times as high as that of the baseline wing with $\beta = 0°$. It can be explained by the help of Figure 4.5 where the ratio between the normalized twist stiffness and flap-wise bending stiffness, S_{44}/S_{66}, is the highest and equal to 2.85. The coupling terms, especially extension-twist coupling S_{44}, also contribute in expanding

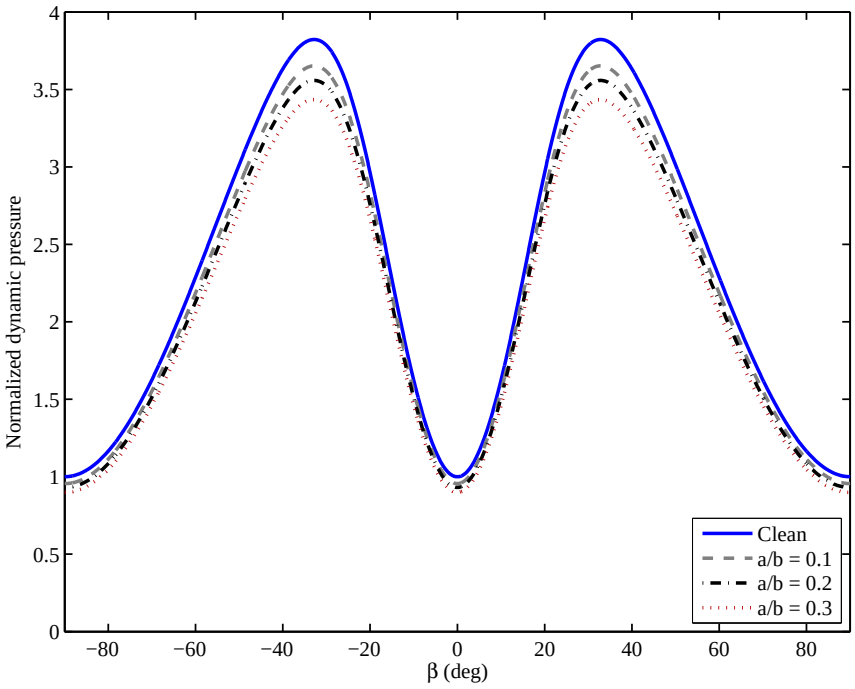

Figure 4.8: Divergence boundaries for wing with antisymmetric layup; Crack location: $0.02L$

the divergence boundary [93], though are of secondary importance for an antisymmetric layup. Figure 4.8 also suggests that the effects of a crack on the divergence speed are the highest for the layup with the maximum divergence speed such that for $\beta = \pm 35°$, the divergence dynamic pressure for a damaged wing with $a/b = 0.3$ is 13.2% lower that that of the clean wing. It is evident from the figure that, increasing the crack length decreases the divergence speed.

A symmetric layup arrangement results in a different aeroelastic behavior. Inspecting Figure 4.9 reveals that for a negative β the divergence dynamic pressure will significantly decrease such that when β is equal to -25° the divergence occurs at a dynamic pressure 84.5% lower than that of $\beta = 0°$. However, even a slightly positive β significantly enhances the divergence stability such that for β between 5° and 80°, the divergence dynamic pressure will be orders of magnitude higher than the baseline case of $\beta = 0°$, should divergence occur at all. Figure 4.4 provides the explanation. As depicted in Figure 4.4, a nonzero bending-twist coupling term, S_{46}, exists for a

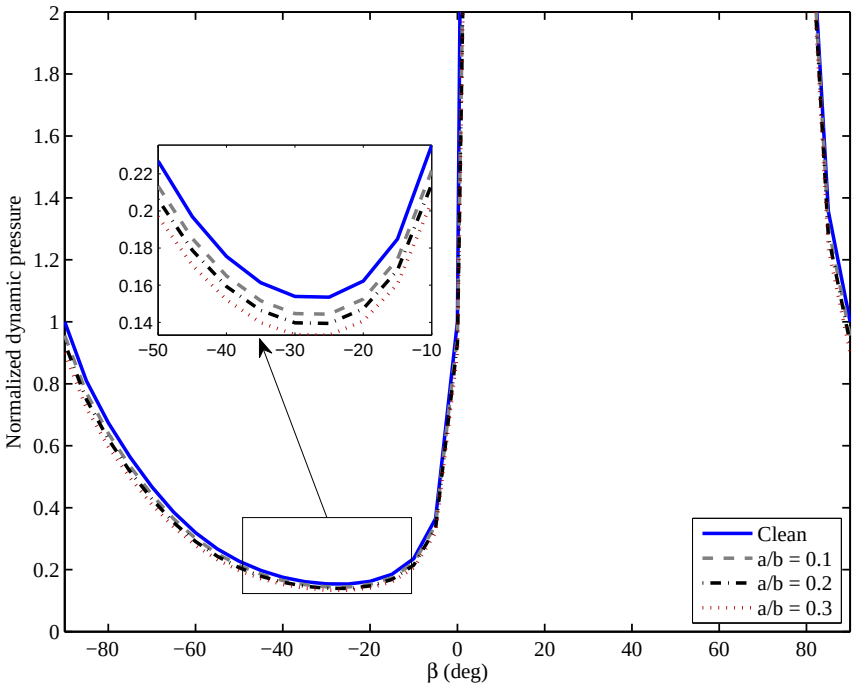

Figure 4.9: Divergence boundaries for wing with symmetric layup; Crack location: $0.02L$

symmetric layup configuration. A coupling factor parameter is defined in Ref. [93] as $\psi = S_{46}/\sqrt{S_{44} \cdot S_{66}}$. A positive symmetric β (i.e., negative ψ), will result in a favorable bending-twist coupling, which in turn significantly enhances the aeroelastic divergence characteristic. A negative β, on the other hand, will drastically reduce the divergence dynamic pressure, and hence must be avoided. For the considered configuration, a maximum ψ equal to -0.19 can be achieved with a symmetric ply angle, β, of $+15°$. In these cases, the divergence speed is so high that comparing it for the clean and damaged wings does not provide much information.

4.3.2 Linear Flutter Analysis

Unlike divergence, which is essentially static and associates with stiffness while mass does not play a role, flutter is a more complicated phenomenon and requires dynamic analysis. Therefore, characterization of flutter is also necessary for a safe design to avoid catastrophic failure of the structure. To this end, the same wing as the one

presented in the previous section is considered and a linear flutter analysis has been carried out for different scenarios. Flutter boundaries are determined by solving a generalized eigenvalue problem. For air velocities below the flutter speed, all eigenvalues have negative real parts. The flutter speed, then, is characterized as the lowest air speed for which one or more eigenvalues cross the imaginary axis to the right half plane, thus making the real part negative. The frequency at which flutter occurs represents the flutter frequency.

To study the effect of crack location on the flutter boundaries, a wing with orthotropic layup, i.e. $\beta = 0°$, is considered in this section. The chord-wise crack extends from the leading edge with three different crack to chord length ratios, a/b, equal to 0.1, 0.2, and 0.3. Of the 16 m of the wing span, only 0.5 m of the wing surrounding the crack is modeled with full 3D solid elements, and the rest of the beam is modeled with 1D elements. The flutter speeds and frequencies are normalized with respect to those of orthotropic layup, i.e., $\beta = 0°$, which are found to be equal to 37.12 m/s and 19.87 rad/s, respectively. Looking at Figs. 4.7 and 4.10 reveals that, compared with divergence, flutter is less affected by the presence of a crack. It can be explained by noting that the overall mass of the wing remains largely the same for clean and cracked wings. It can be observed from the figure that a crack with $a/b = 0.3$ located at $0.05L$ will decrease the divergence dynamic pressure by about 5.5%, whereas the crack with $a/b = 0.1$ will reduce it by 2.0%. The effect of the intermediate case, $a/b = 0.2$, lies between those of the other two. The figure also shows that the effect of a crack on the flutter boundary weakens as the crack gets closer to the wing-tip such that for the cracks located at $0.90L$ the flutter speed for all three cases are very close to that of the undamaged wing. The same is true about the flutter frequency, shown in Fig. 4.10 (b), where a small decrease in the overall stiffness of the wing would cause a slightly lower flutter frequency.

The flutter analysis has also been done for wings with cracks located at the trailing

edge and the result are presented in Fig. 4.11, for the sake of completeness. As can be seen in the figure, the results for both flutter speed and flutter frequency are very close to those of the wing with leading edge cracks, and the differences are negligible for this case.

A parametric study on the effects of damage on the flutter boundary of the wing with different layup arrangement has been carried out. Normalized flutter speeds and frequencies with respect to the laminate angles for both antisymmetric and symmetric layups are shown in Figs. 4.12 and 4.13, respectively. All chord-wise crack at the leading edge are located at $0.02L$ which, according to Fig. 4.10, has the most detrimental effect on the flutter boundary. The flutter speeds and frequencies are normalized with respect to that of the baseline layup with $\beta = 0°$. For the antisymmetric layup configuration, Fig. 4.12 shows a symmetry about $\beta = 0°$, previously observed in Fig. 4.8 for aeroelsatic divergence instability. This is true for both flutter speed and flutter frequency. Also, the existence of a crack has the greatest negative effect on the flutter speed for the case where the flutter speed and frequency are maximum, i.e., when β is equal to $\pm 35°$. For this layup angle, cracks with a/b equal to 0.1 and 0.3 will reduce the flutter speed by 5.3% and 12.7%, respectively. However, a symmetric layup improves the flutter condition by 70%, at most, which is smaller than the factor of 3.82 obtained for the divergence.

Examining Fig. 4.13, on the other hand, reveals that symmetric layup does not exhibit any symmetry about $\beta = 0°$, which was also the case for the divergence instability. However, while a negative symmetric layup angle would drastically decrease the divergence boundary, it will not have a similar effect on the flutter condition and a negative layup will also increases the flutter speed, though not as much as a positive angle. The lack of symmetry is more profound in the case of flutter frequency. It can be observed that the flutter frequency will decrease for β greater than zero and attains a minimum at $\beta = 20°$. There is a sharp increase in the flutter frequency

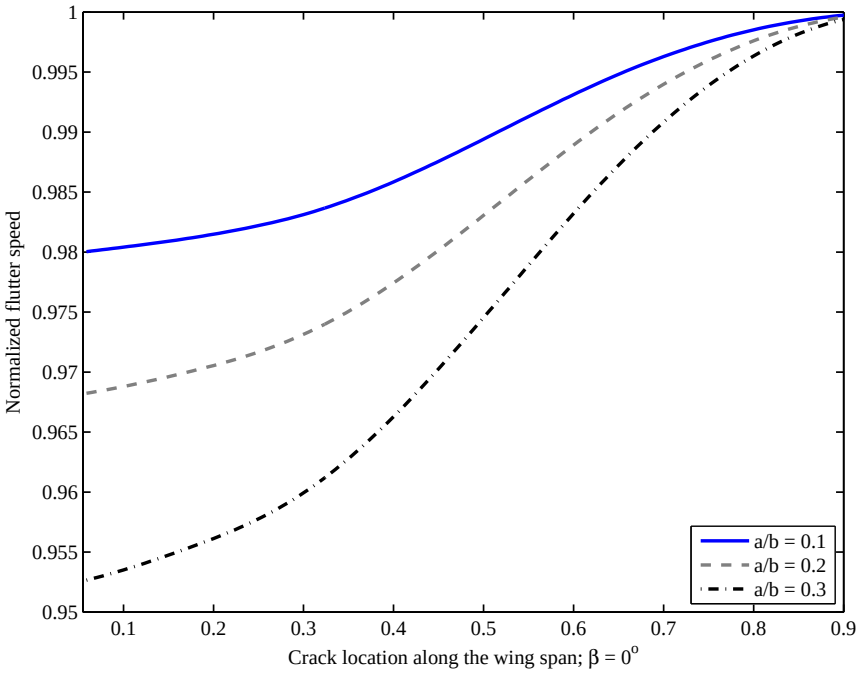

(a) Flutter speed

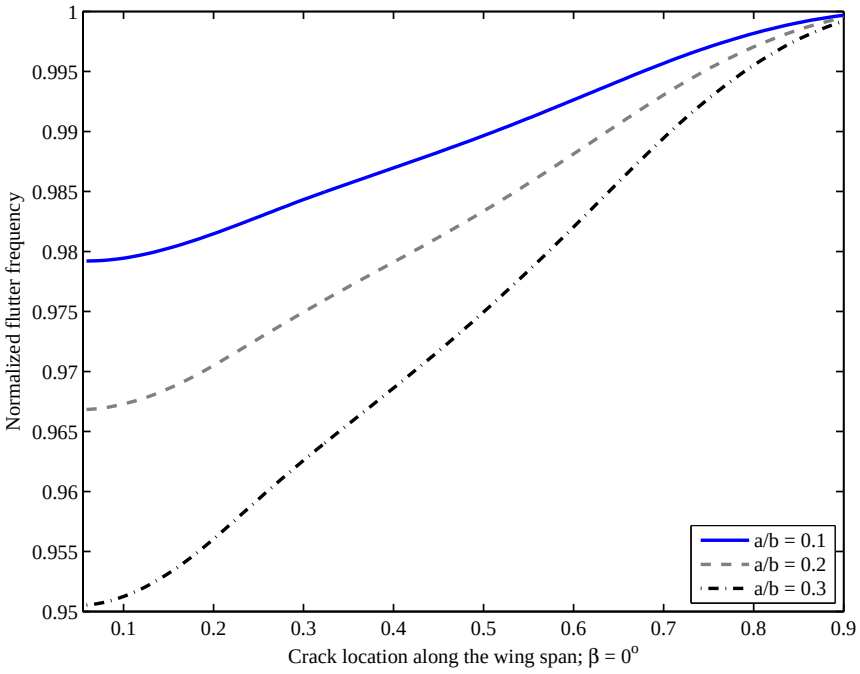

(b) Flutter frequency

Figure 4.10: Flutter boundaries for leading edge cracks varied along the span

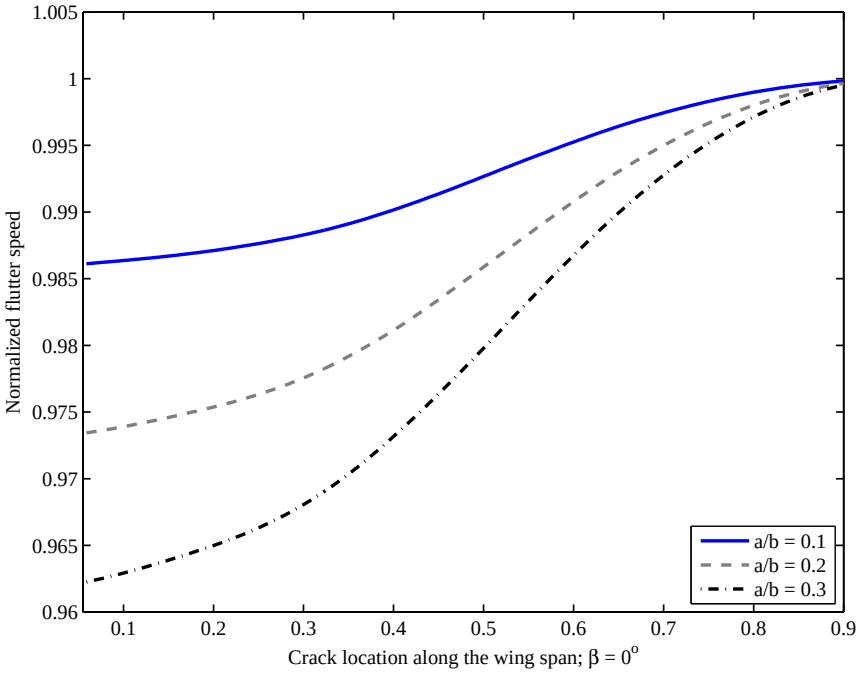

(a) Flutter speed

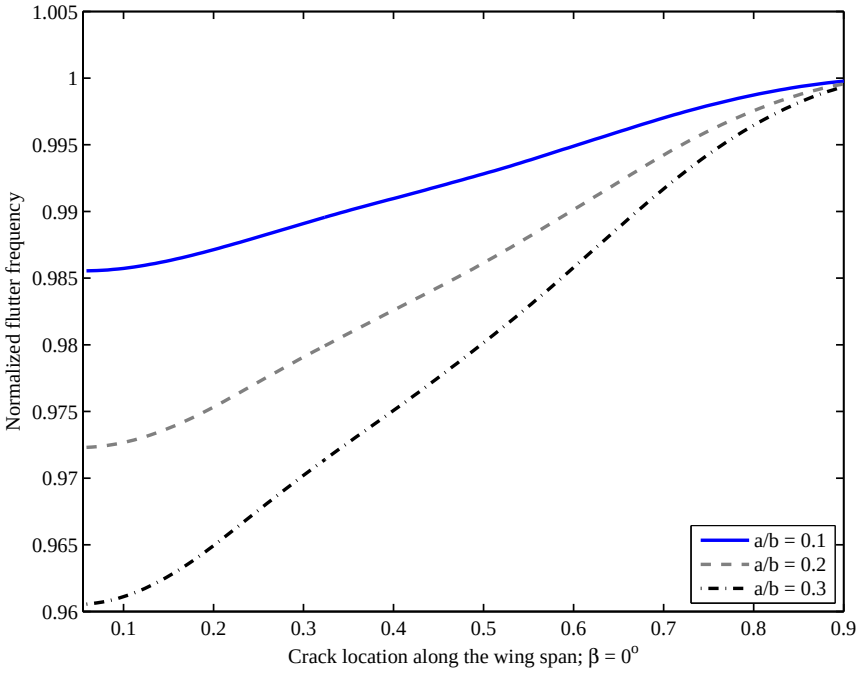

(b) Flutter frequency

Figure 4.11: Flutter boundaries for trailing edge cracks varied along the span

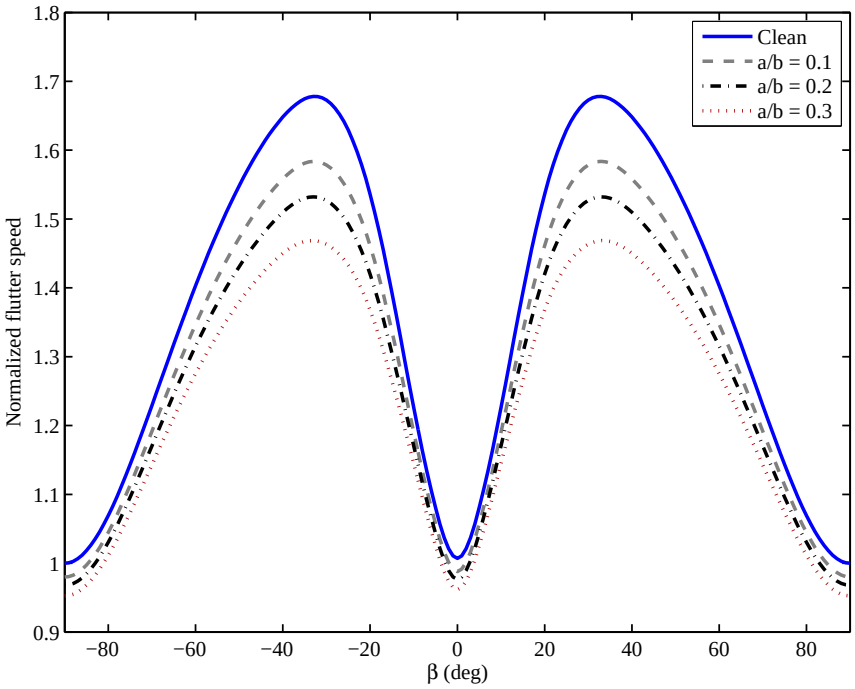

(a) Flutter speed

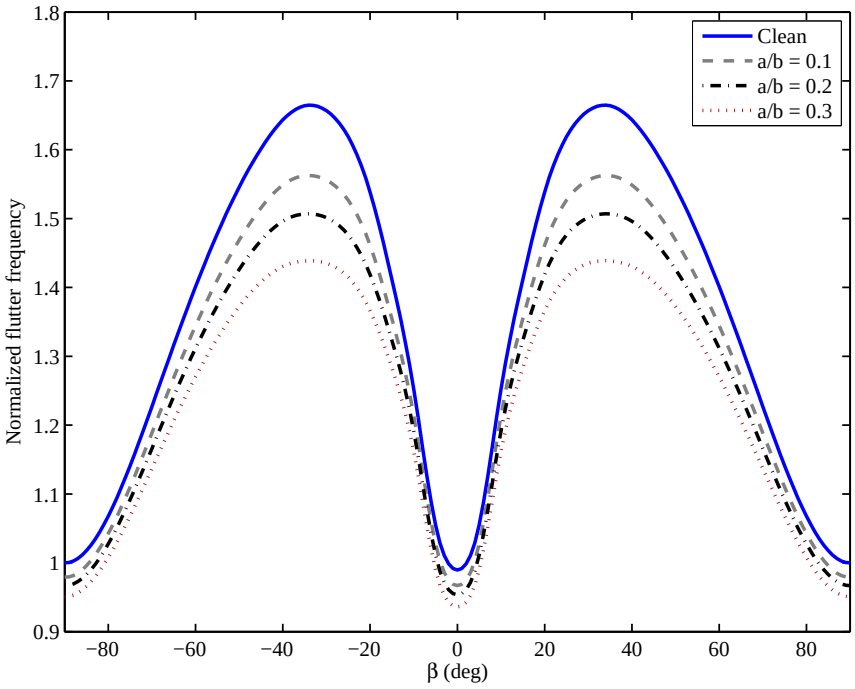

(b) Flutter frequency

Figure 4.12: Flutter boundaries for clean and damaged wings; Crack location: 0.02L

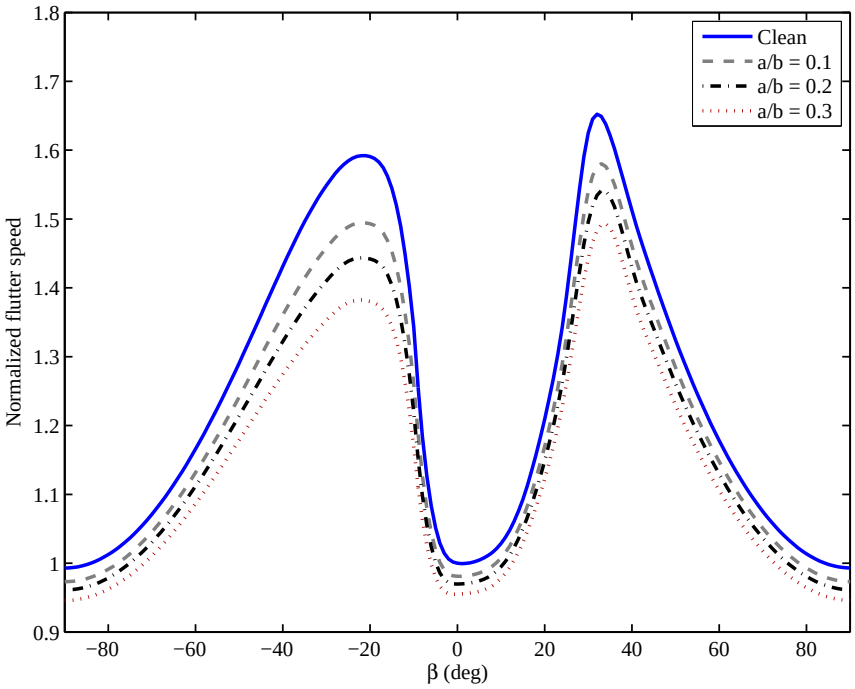

(a) Flutter speed

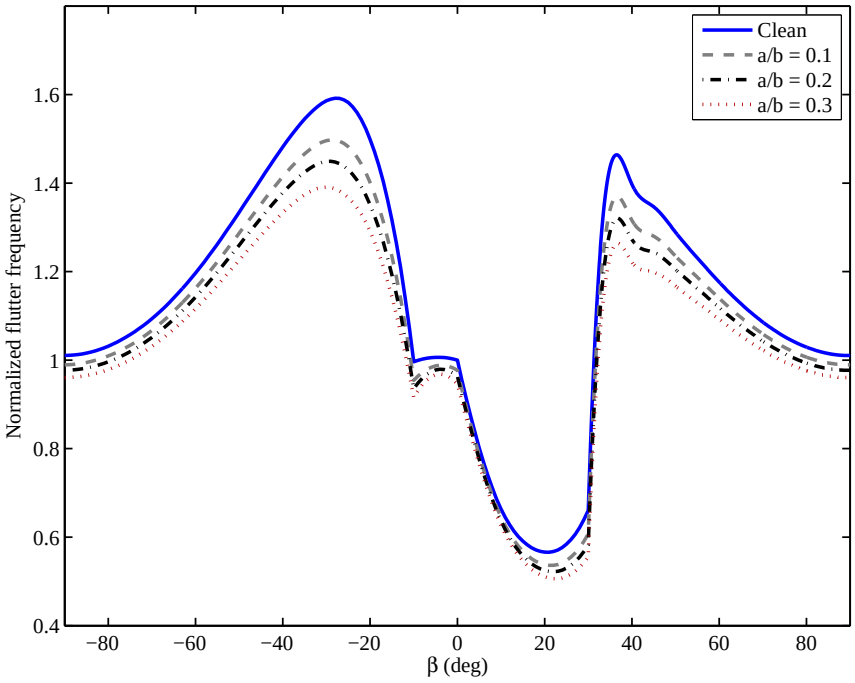

(b) Flutter frequency

Figure 4.13: Flutter boundaries for clean and damaged wings; Crack location: $0.02L$

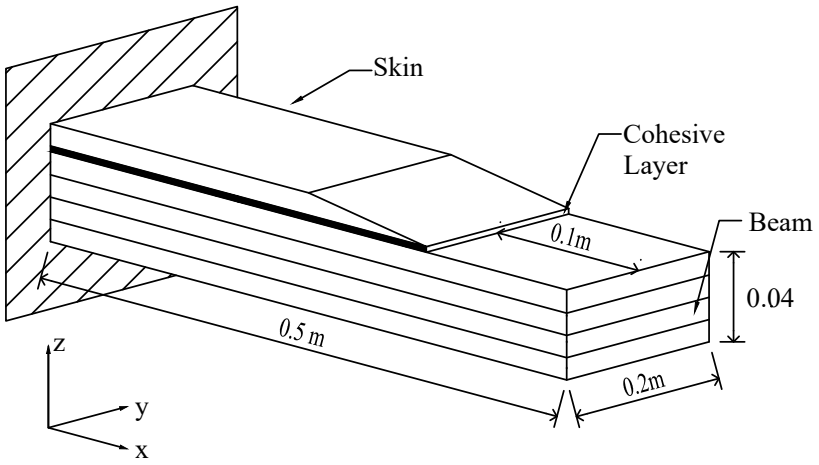

Figure 4.14: Wing reinforced near the root

between $\beta = 30°$ and $\beta = 35°$ before it start to decrease again. The sharp change can be explained by the fact that different flutter modes with different frequencies exist and changing the layup will cause a different mode to go unstable at the same flutter speed while other modes remain stable. Other observations made about effects of a crack, already made for antisymmetric layup also hold true for the symmetric layup.

A different damage scenario, namely skin delamination near the wing-root, has also been considered here. The same wing depicted in Fig. 4.3 has been reinforced near the root with a skin made of the same material as the wing, which is depicted in Fig. 4.14. However, instead of a leading edge or trailing edge crack, the skin has been partially detached from the wing along the span (Figure 4.15). Two different cases with delamination to chord ratios, a/b, equal to 0.5 and 1.0 are considered. The flutter characteristics for delaminated cases are compared with those of a clean, reinforced wing, and the analysis results for both antisymmetric and symmetric layup are presented in Figs. 4.16 and 4.17, respectively. The reinforcement slightly increases both the flutter speed and frequency such that for an undamaged wing with $\beta = 0°$ the flutter speed and frequency will be 38.21 m/s and 20.04 rad/s, respectively. These findings are used for normalizing the results shown in Figs. 4.16 and 4.17.

Close examination of the figures shows that, compared with crack, delamination

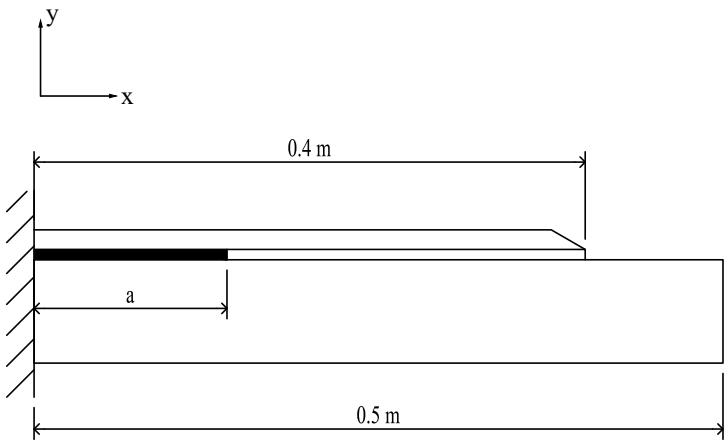

Figure 4.15: Delamination in the wing

has even a smaller effect on the flutter boundary, especially when the stiffness couplings are small. Other qualitative observations already made for the crack cases, either for symmetric or antisymmetric layups, remain valid for the delamination case.

4.4 Nonlinear Aeroelastic Analysis

Ease of computations come especially handy for parametric studies, such those presented in Section 4.3. Linear aeroelastic analysis methods, very useful and powerful in their own right, suffer from their own limitations and shortcomings. In the case of HALE aircraft, where nonlinearities stemming from large deformations and aerodynamic effects are omnipresent, nonlinear aeroelastic analysis becomes a necessity. While both static and dynamic analyses carried out in the previous chapter were solely linear, meaning that large deformations were not present, nonlinear aeroelasticity can be approached from two different directions. The first approach, applicable to both static and dynamic cases, consists of finding the static equilibrium solution, or trim, at a specific flight condition and then linearizing equations of motion about that equilibrium. In this case, nonlinear effects will manifest themselves in the equilibrium solution and small perturbations about that nonlinear equilibrium, which are linear in nature, will be studied. An eigenvalue analysis, similar to those undertaken before,

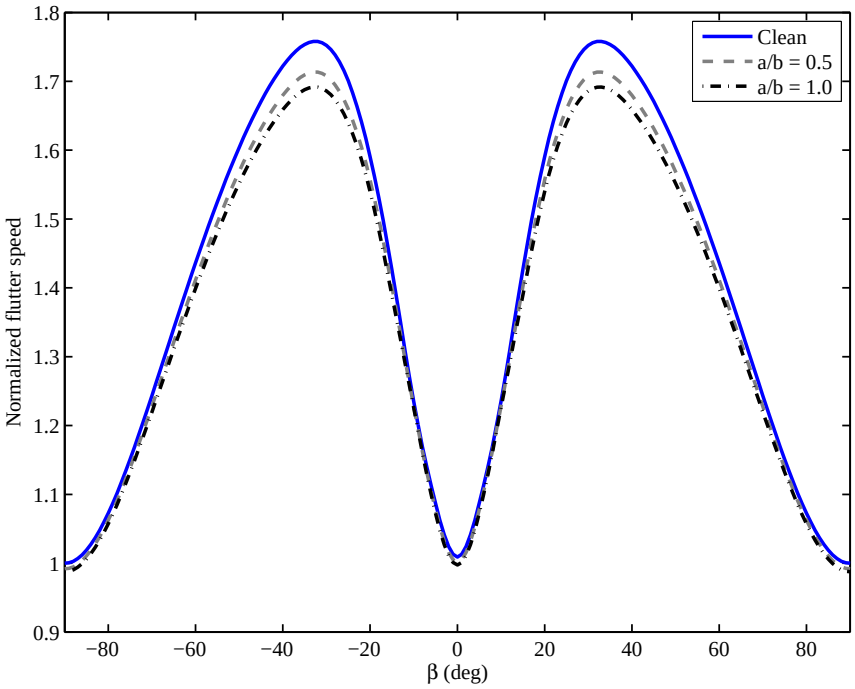

(a) Flutter speed

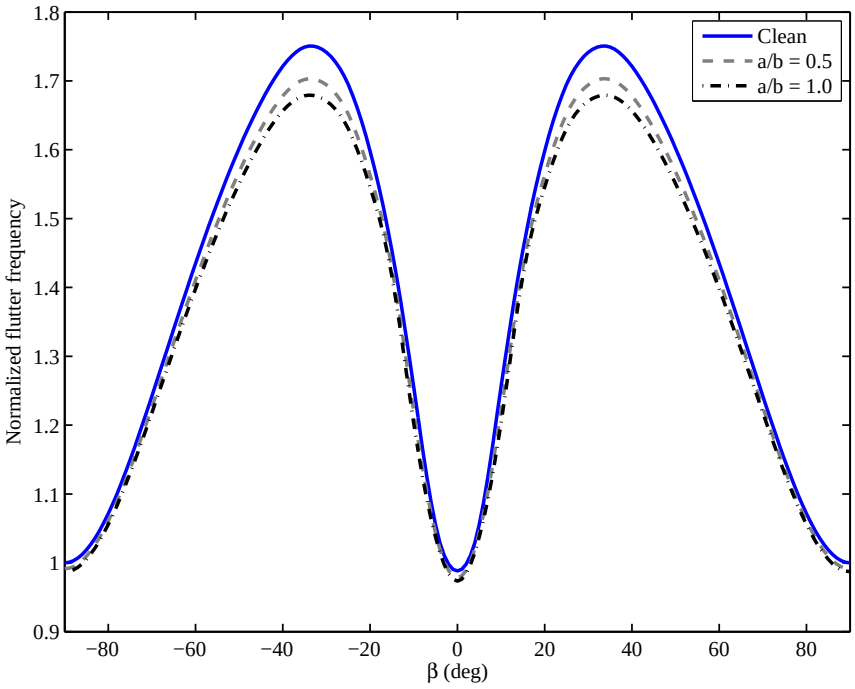

(b) Flutter frequency

Figure 4.16: Flutter boundaries for delamination; antisymmetric layup

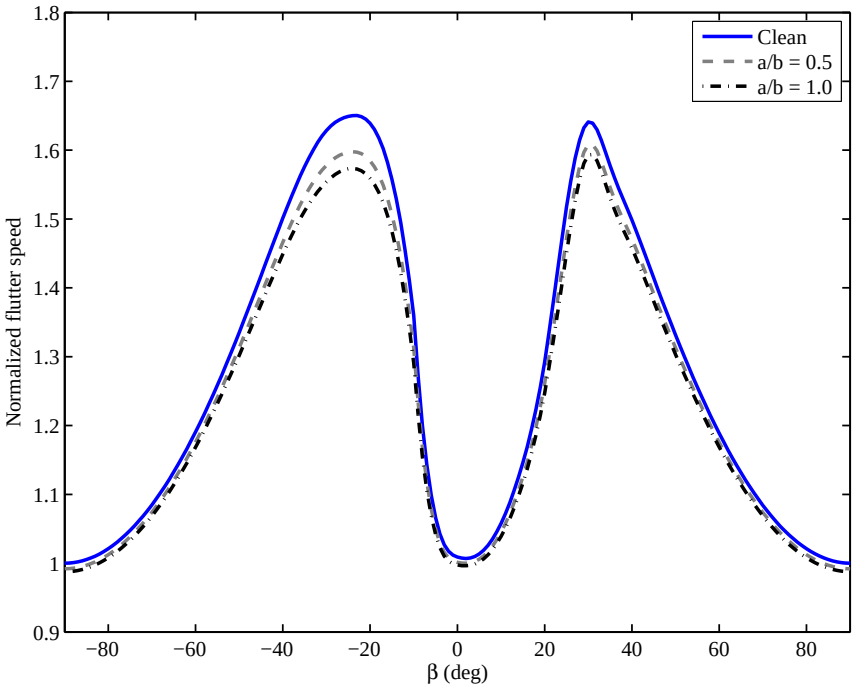

(a) Flutter speed

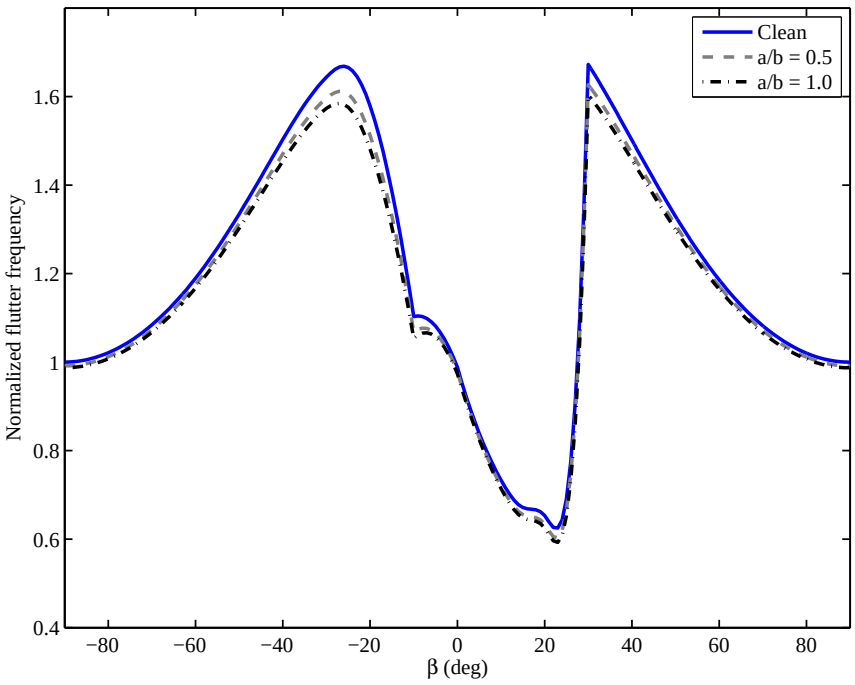

(b) Flutter frequency

Figure 4.17: Flutter boundaries for delamination; symmetric layup

will then be carried out to determine the stability characteristics.

For the case of damaged wings, material failure and crack growth can also be investigated as a nonlinear quasi-static problem, meaning that the arbitrarily large deformations are taking place slowly enough that the inertial effects can be neglected. As shown in Chapter III, the joined 3D/1D approach will deliver an accurate stress distribution around the damage area. Therefore, the evolution of damage can be monitored during the simulation and any possible crack growth can be detected.

Nonlinear aeroelastic behavior of the wing can be investigated beyond the stability and quasi-static analysis. Although linear analysis can be invoked to predict stability boundaries and the onset of instabilities, it fails to provide much information beyond that point. A linear dynamic analysis would claim that for a flexible wing at the flutter condition and beyond, the amplitude of perturbations would grow unboundedly, whereas nonlinear geometric and aerodynamic effects will bound the growth and in most cases the perturbations will eventually end up in an LCO [44, 45]. This has far-reaching consequences, making a nonlinear dynamic analysis necessary. Here, a nonlinear time-marching can be performed to study post-flutter behavior and LCO. In a stable LCO the deformations are bounded. However, depending on the amplitude of oscillations, it may put excessive structural loads on the wing which not only can reduce the life-cycle of the airframe, but may also compromise the structural integrity and result to a catastrophic failure of the structure. When dealing with damaged wings, being able to characterize the causes and mechanisms of forming and sustaining LCO is of paramount importance, as the structure is more prone to failure. Nonlinear time-marching for a full 3D FE model is a computationally intensive task. In this case, the joined 3D/1D approach offers a computationally economical alternative in early stages of the design and analysis.

It was already demonstrated in Figs. 4.7 and 4.10 that, for a fixed crack to chord ratio a/b, damage near the wing-root has the most significant effects on the

divergence and flutter speeds and its effect will diminish by getting closer to the wing-tip. Therefore, in what follows, only cases with a crack located at $0.02L$ are considered for LCO analysis.

4.4.1 Nonlinear Aeroelastic Divergence

In Subsection 4.3.1, the divergence was studied for undeformed wings. However, as the dynamic pressure increases the wing deforms and the equilibrium condition would change. For HALE aircraft wings, most notably, the deformed configuration can be drastically different from the undeformed one. Therefore, new divergence instability conditions may be found for the new deformed equilibrium. Figure 4.18 shows the difference in the divergence conditions due to the loading for various subcritical dynamic pressures. It can be seen in the figure that, before the ratio between the loading dynamic pressure and the linear divergence dynamic pressure, q/q_{div}, reaches 0.5, the difference between linear and nonlinear divergence conditions is negligible. However, after that the difference increases such that when q/q_{div} is equal to 0.7, a linear analysis results for the divergence instability would differ from a nonlinear analysis by 3.8%. The difference increases to 6.9% for $q/q_{\text{div}} = 0.8$. This clearly demonstrates the importance of including geometric nonlinearities in the determination of aeroelastic divergence of HALE aircraft wings.

Also shown in Fig. 4.18 is the difference in divergence dynamic pressure for the damaged wing. According to the figure, the same qualitative behavior can also be seen when a crack exists near the root of the wing, which seems plausible considering the overall stiffness degradation of the structure due to damage. As can be verified from the figure, before the ratio between the loading dynamic pressure and the linear divergence dynamic pressure, q/q_{div}, reaches to 50% the difference between linear and nonlinear divergence conditions is negligible. However, after that the difference increases such that when q/q_{div} is equal to 0.8, a linear analysis results for the divergence instability

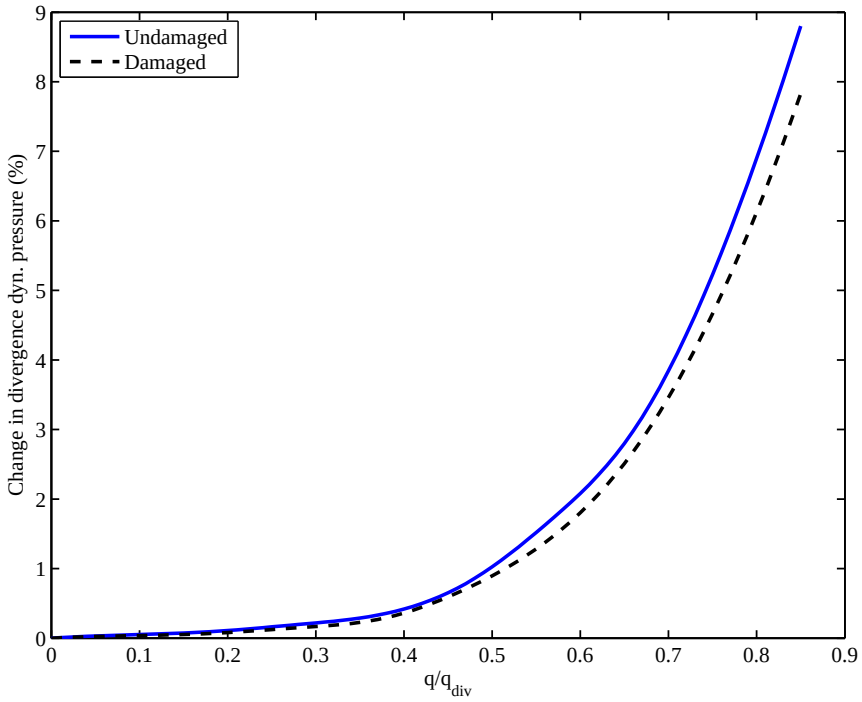

Figure 4.18: Change in divergence dynamic pressure with nonlinear equilibrium

would differ from a nonlinear analysis by 6.2%. Very similar results are found for the case of delamination. Therefore, the results are labeled as *Damaged* in the figure.

Another interesting finding of nonlinear analysis is the difference between the crack growth in a wing with a leading edge crack and a trailing edge crack. Figure 4.19 shows the area around the crack at the leading edge when the $q/q_{\text{div}} = 0.83$. It can be seen that the crack has started to grow, marked as STATUSXFEM around 0.5. Although the linear analysis did not show any difference between a crack located at the leading edge as opposed to the trailing edge, Fig. 4.19 shows that the crack at the trailing edge does not grow for a similar loading condition. This can be explained by the fact that while for a leading edge crack, displacement in y direction, leads to the opening of a Mode I crack, a trailing edge crack would be closing instead so that the crack growth is delayed.

A damage growth has also been detected for the case of delamination. However, the simulation shows that it only occurs when the delaminated area is very large, a/b

greater than unity, which is an extreme condition.

The results obtained in this section cannot be attained using a pure 1D analysis, and a full 3D FEM analysis requires a lot of computational power. The joined 3D/1D method, in contrast, offers a relatively inexpensive alternative for that, which could be expedient at the early stages of aeroelastic design and analysis of HALE aircraft wings.

4.4.2 Nonlinear Flutter Analysis

In Subsec. 4.3.2 linear flutter analysis was carried out for damaged and undamaged wings. However, it has been known that geometric and aerdynamic nonlinearities would affect flutter characteristics of wings. The linear analysis does not take into account the fact that the structure will deform under aerodynamic loading. Therefore, in this section, the flutter conditions are calculated based on the linearized equation about a nonlinear equilibrium configuration. After the static equilibrium solution is found and equations are linearized about that solution, the rest of the procedure will be similar to what was done before, namely by increasing the air velocity and looking for the velocity at which one or more eigenvalues have positive real parts.

Figure 4.20 shows the flutter speed and frequency with the root angle of attack for a baseline wing with a leading edge chord-wise crack near the root. Also depicted in the figure are the flutter boundaries for the undamaged wing as well as the reinforced wing near the root with a partially delaminated skin. It can be clearly seen in the figure that both the flutter speed and flutter frequency are affected by root angle of attack. This is due to the fact that by increasing the angle of attack, the static equilibrium would alter and the wing will move further away from the unloaded and undeformed reference configuration.

The damaged wings, however, are more affected by increasing the root angle of attack as the static deformation will be larger for them as a result of lower overall

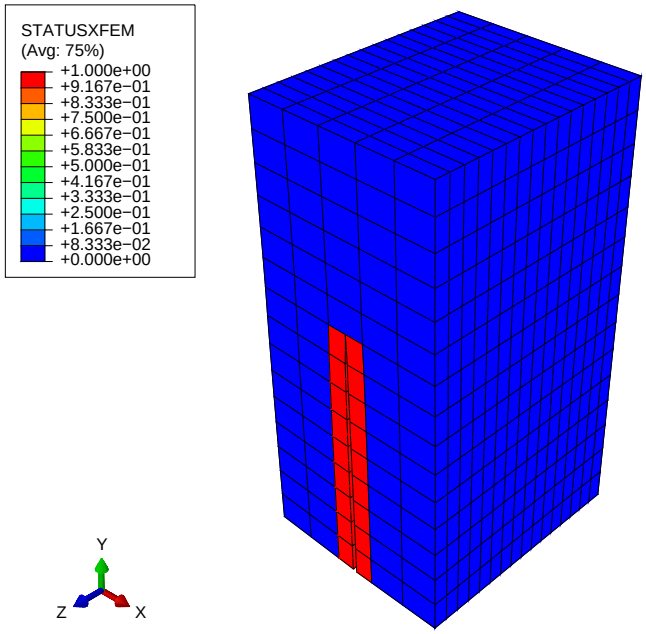

(a) Before crack propagation

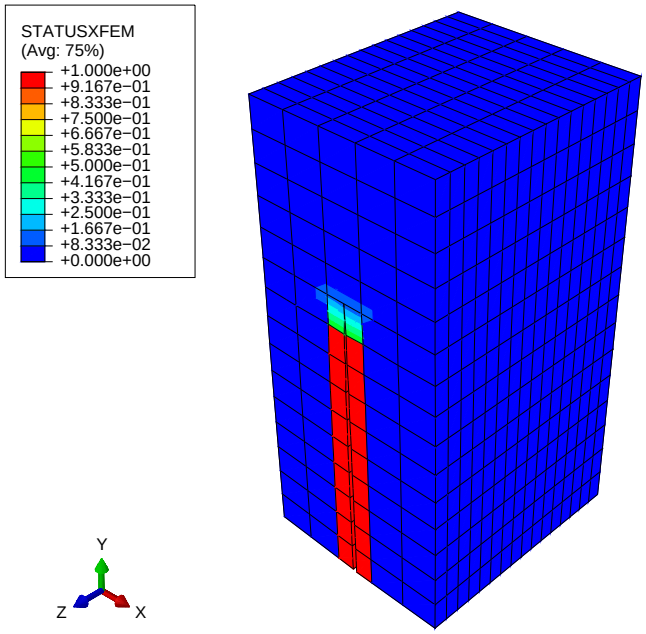

(b) After crack propagation

Figure 4.19: Crack growth for nonlinear static aeroelasticity

stiffness of the structure. It can be seen from the figure that the flutter speed at the zero angle of attack, which is the same as a linear flutter speed, is higher than the one associated with an angle of attack equal to 4 deg. The difference is more than 2.6 m/s for damaged cases as opposed to 1.5 m/s for the undamaged wing. The flutter frequency also changes in a similar fashion. The analysis highlights the importance of a nonlinear analysis for high $\mathcal{AR}$ wings.

4.4.3 Limit Cycle Oscillations

Evolution of LCO is investigated in this section for two different layups; a baseline wing without stiffness coupling (i.e., $\beta = 0°$), and one with bending-twist coupling which is a result of a symmetric layup arrangement. It was shown in Figs. 4.9 and 4.17 that a layup with positive β will substantially enhance divergence and flutter stabilities. Hence, here a positive layup with $\beta = 45°$, resulting in a negative coupling factor ψ, is considered. The analysis proceeds as follows.

For the undamaged baseline wing, i.e., $\beta = 0°$, the simulation was first done for an air velocity close to the linear flutter speed, namely $V_\infty = 37$ m/s. The time histories of tip vertical displacement and twist at this velocity are shown in Figure 4.21. As can be seen in the figure, at the beginning the oscillations grow exponentially and reach 1.26 m at 5.96 s. However, due to geometric stiffness, the oscillations cannot grow beyond that point and start to subside in amplitude and eventually settle in a stable LCO in which the wing tip oscillates almost harmonically between 0.54 and 1.20 m. The same observation is made for the tip twist, where the wing oscillates between -10 deg and 21 deg. In that figure, the existence of LCO is verified by the phase portrait of the wing-tip displacement. FFT plot shows that two harmonics exist where the frequency of 17.18 rad/s is dominant. It is worth mentioning that, according to Fig. 4.22, during the stable phase of the LCO, the tip displacement and twist oscillations are almost out of phase such that the upper limit of the tip displacement, 1.20 m,

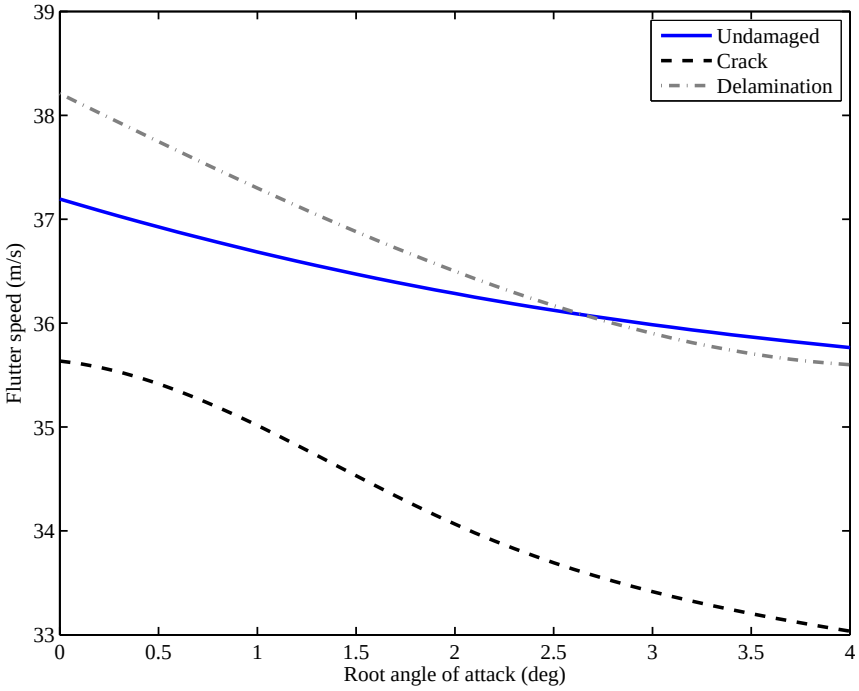

(a) Flutter speed

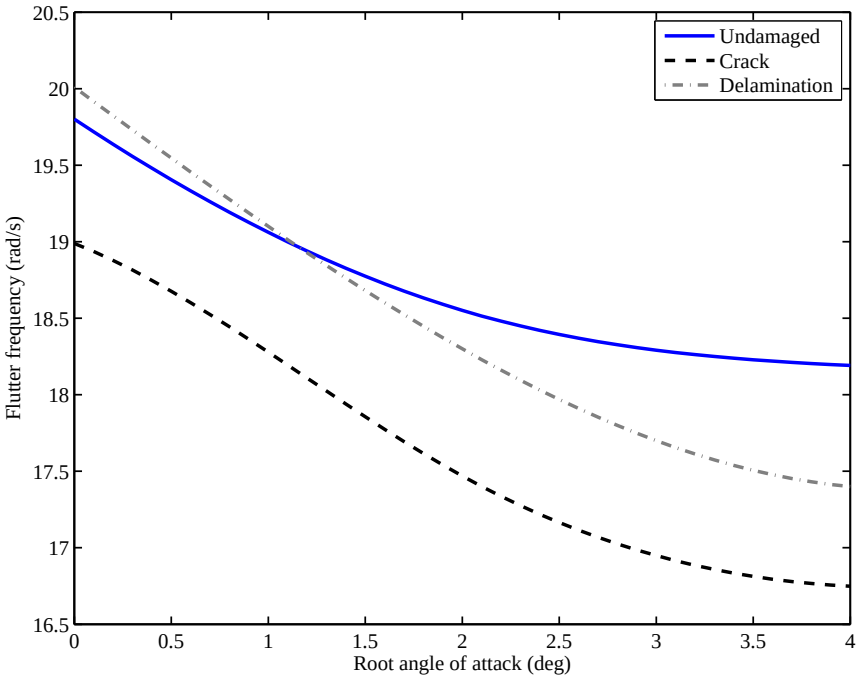

(b) Flutter frequency

Figure 4.20: Nonlinear flutter boundaries for undamaged and damaged wings

corresponds to the lower limit of the tip twist, -10 deg. This would appear to be the limiting mechanism by which the aerodynamic lift and pitching moment, along with geometric stiffness, would sustain a bounded LCO. The simulation results for the damaged wing at the same air velocity, namely $V_\infty = 37$ m/s, are presented in Figs. 4.23 and 4.24. Comparing these figures with Figs. 4.21 and 4.22 shows that although LCO for the damaged and clean wings are qualitatively very similar, there are still differences between the nonlinear time responses such that a second harmonic appears to start forming for the damaged wing. The upper limits for both tip displacement and twist are slightly higher for the damaged wing and found to be 1.32 m and 23 deg, respectively.

As the air velocity increases to 39 m/s, both the amplitude and frequency of the oscillations are noticeably altered. For the clean wing, the time histories of tip vertical displacement and twist at this velocity are shown in Figure 4.25. Similar to the previous case, the oscillations start to grow exponentially and the tip displacement reaches to 1.61 m at 2.74 s. At this point the geometric stiffness arising from the large deformations hinders the growth of oscillations and instead drives them into an LCO. The difference between the upper and lower bounds of the amplitudes is higher in this case. While the tip displacement varies between 0.33 m and 1.61 m, the tip twist oscillates between -16.5 deg and 24.5 deg. The LCO for this case, however, is different from the one at 37 m/s. Whereas for the 37 m/s case only one harmonic existed, the phase plot for 39 m/s case, Fig. 4.26, reveals that there are three harmonics present in this case, and the dominant harmonic has slightly increased to 17.8 rad/s.

For the damaged wing the differences are more noticeable. It can be seen from Figs. 4.27 and 4.28 that the frequency spectrum is broader for the damaged wing and more harmonics exist for this case. Effects of nonlinear aerodynamics start to become more significant as the angle of attack increases and its interaction with the flexible structure causes larger deformations. Both displacement and twist are still bounded,

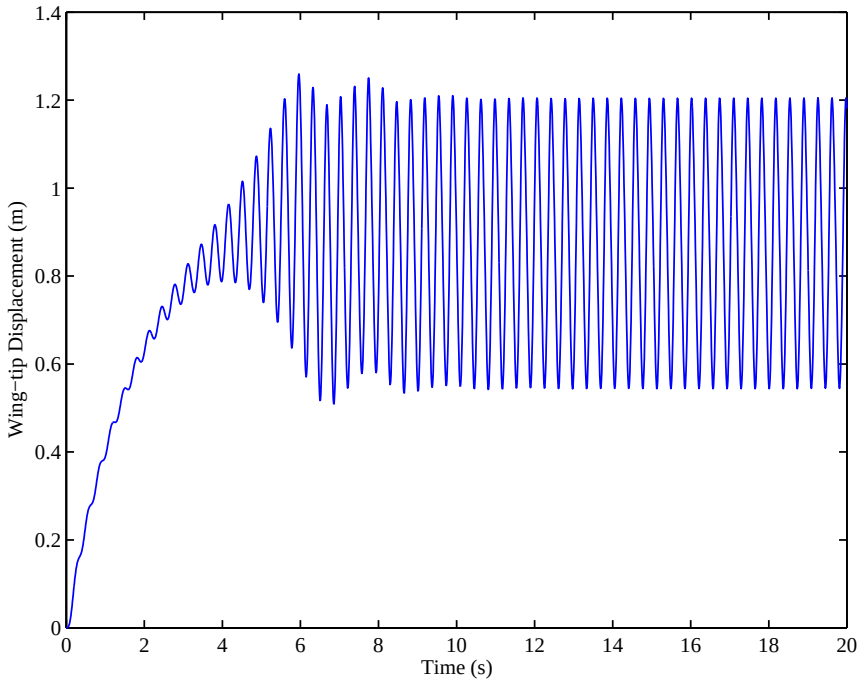

(a) Displacement

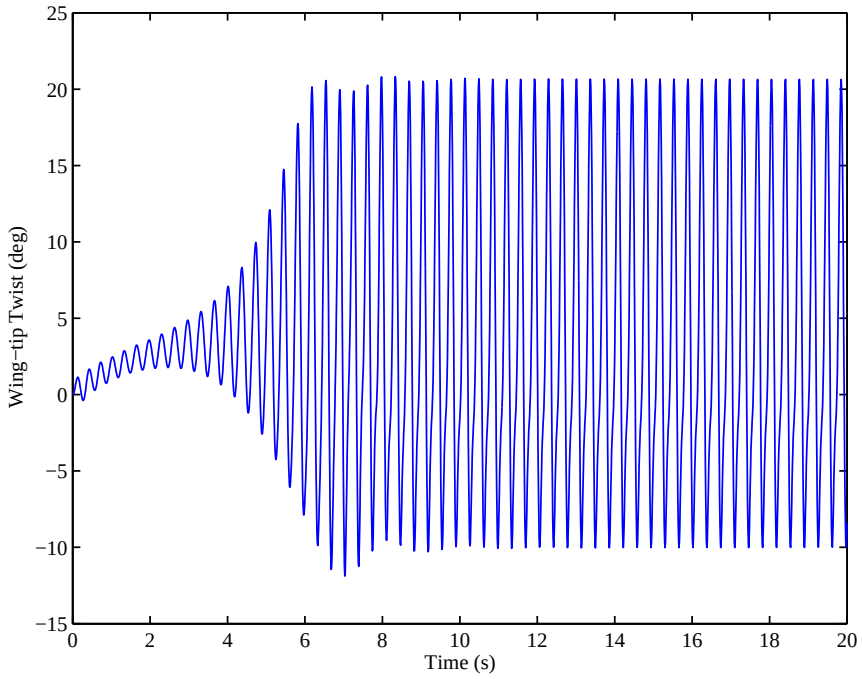

(b) Twist

Figure 4.21: Wing-tip displacement and twist, $V_\infty = 37$ m/s

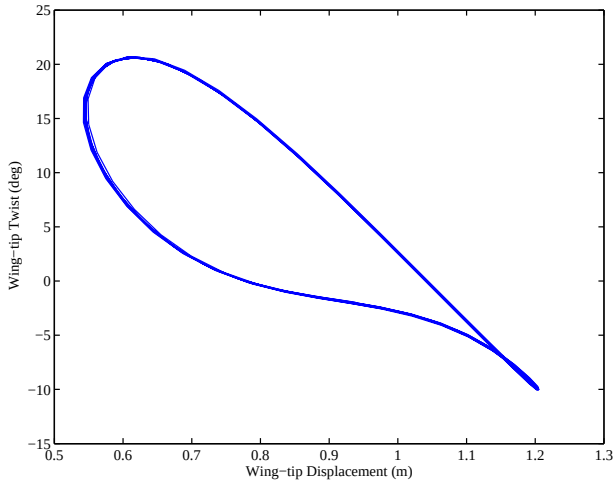

(a) Twist-displacement

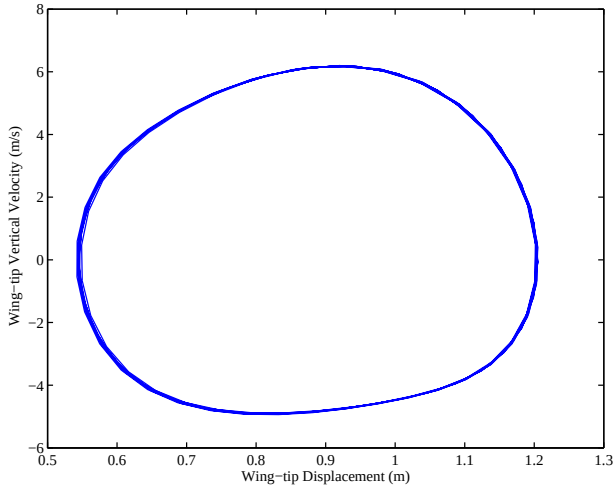

(b) Phase portrait

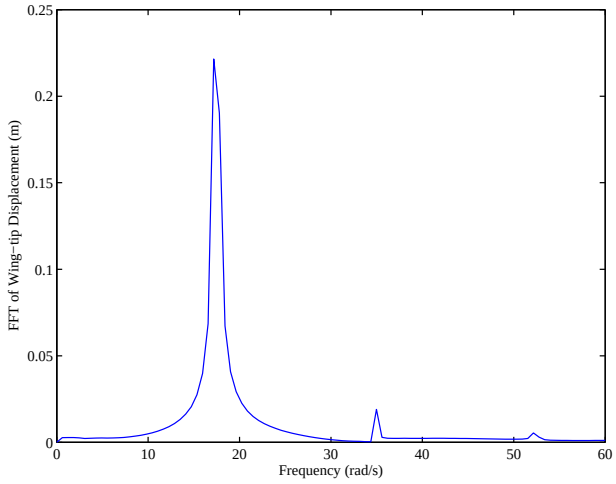

(c) Displacement

Figure 4.22: Phase portraits and FFT, $V_\infty = 37$ m/s

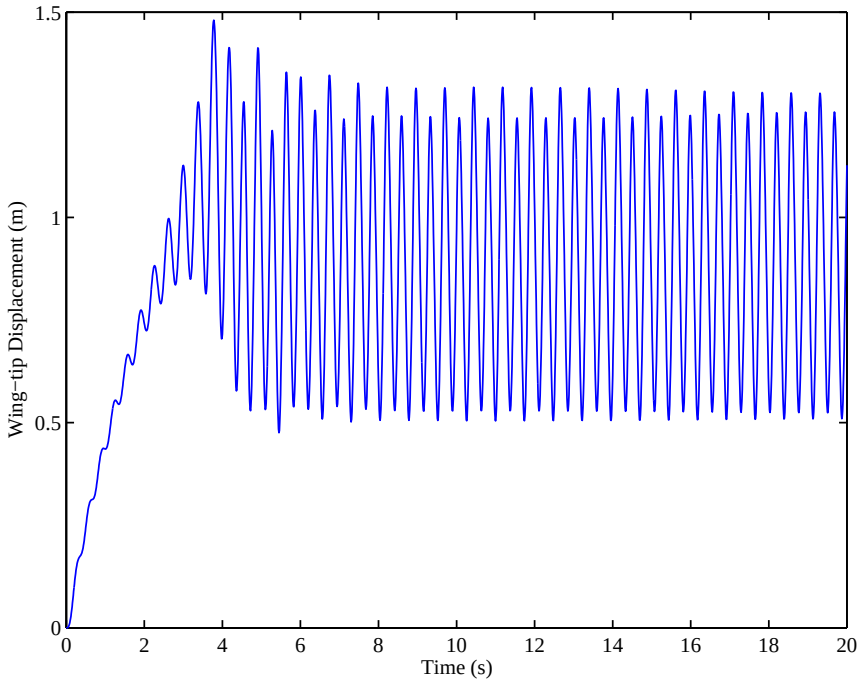

(a) Displacement

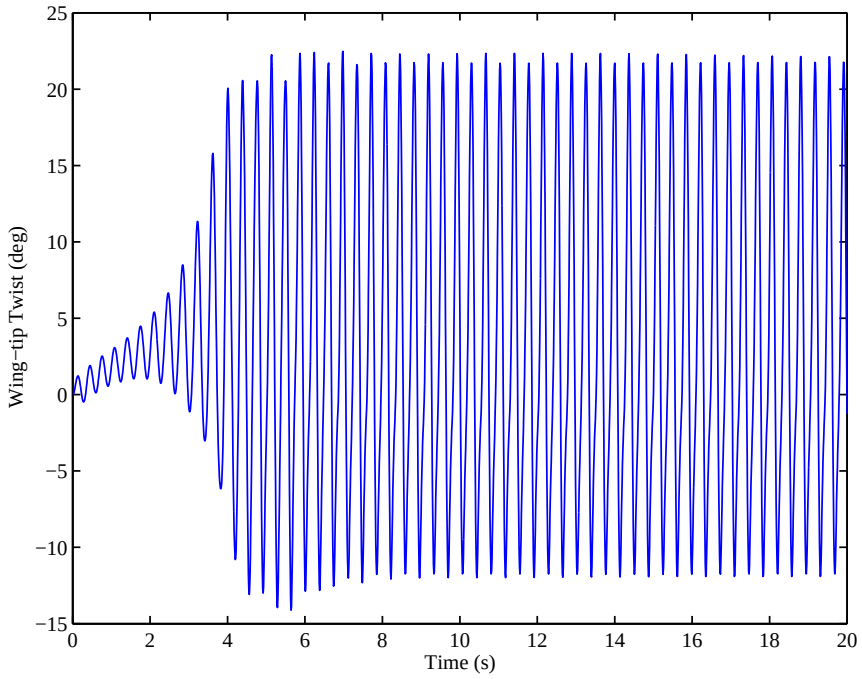

(b) Twist

Figure 4.23: Wing-tip displacement and twist for damaged wing, $V_\infty = 37$ m/s

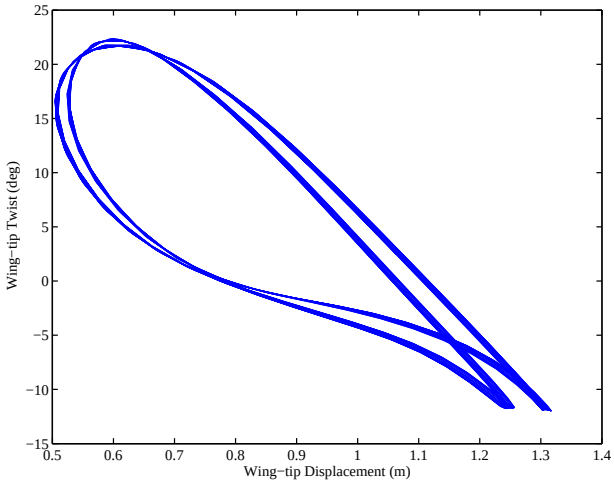

(a) Twist-displacement

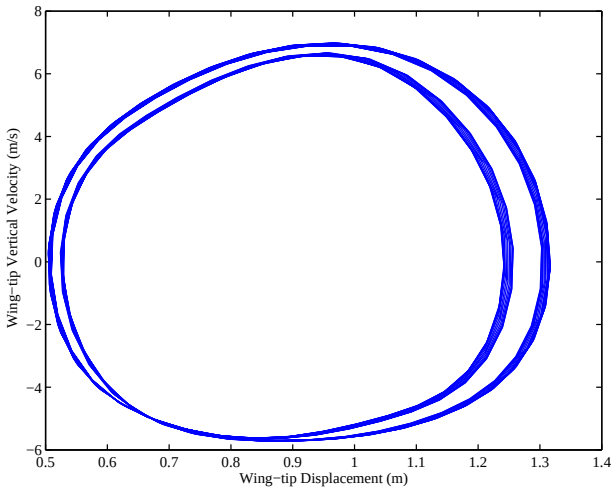

(b) Phase portrait

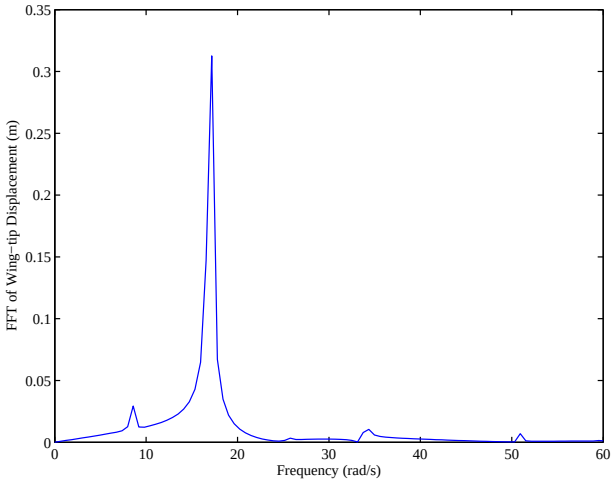

(c) Displacement

Figure 4.24: Phase portraits and FFT for damaged wing, $V_\infty = 37$ m/s

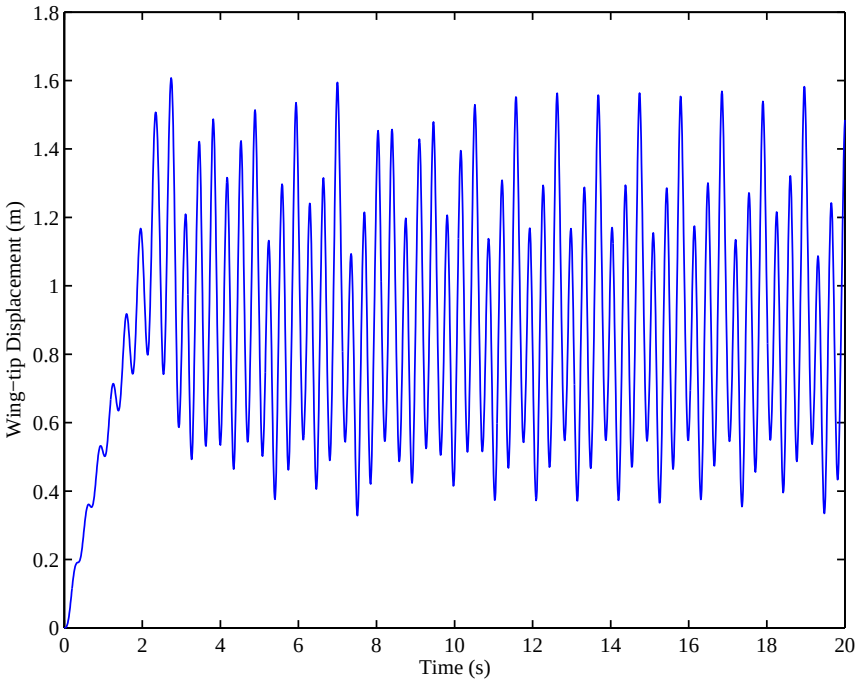

(a) Displacement

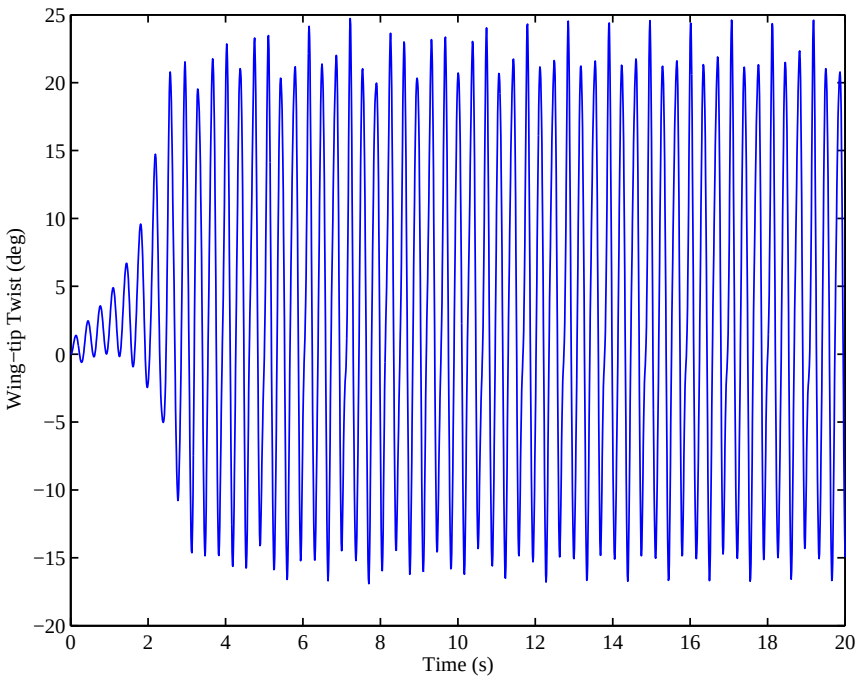

(b) Twist

Figure 4.25: Wing-tip displacement and twist, $V_\infty = 39$ m/s

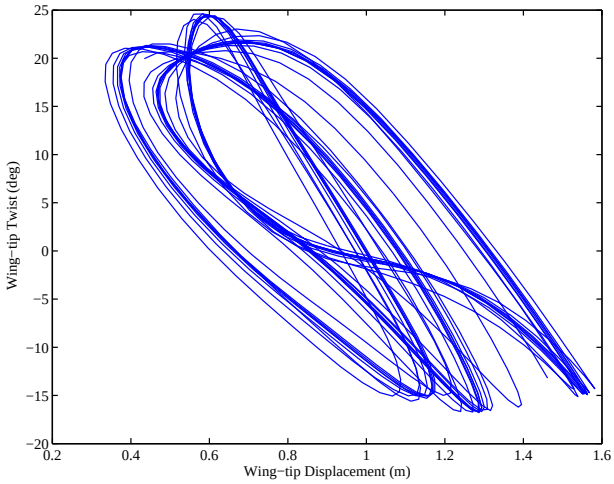

(a) Twist-displacement

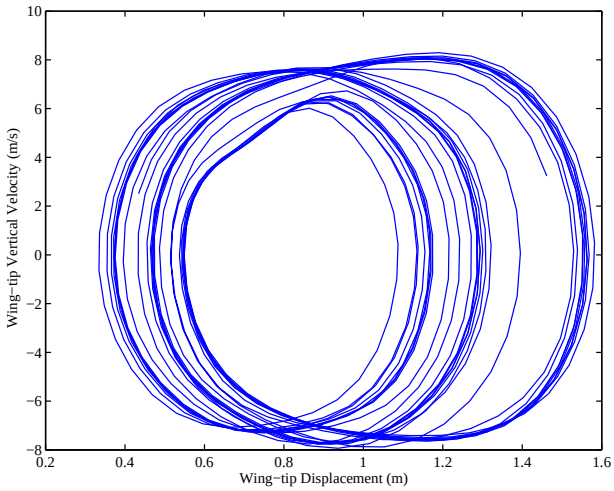

(b) Phase portrait

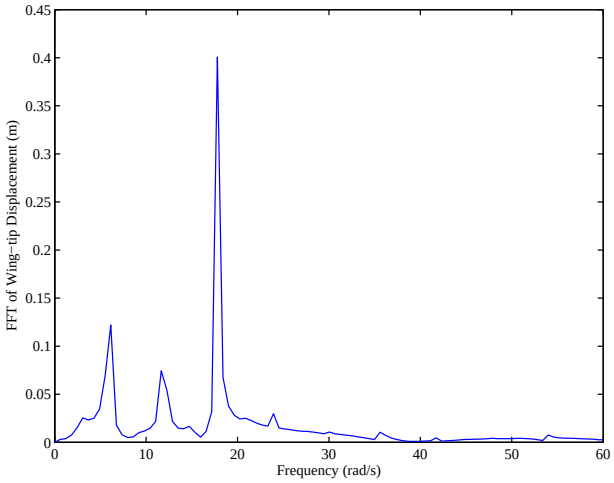

(c) Displacement

Figure 4.26: Phase portraits and FFT, $V_\infty = 39$ m/s

however, the upper bound for them have increased to 1.79 m and 27 deg, respectively which shows the effect of reduced overall stiffness caused by the crack.

Increasing the flow velocity to 41 m/s causes the angle of attack to enter the nonlinear range. The nonlinear coupling between large deformations and angle of attack becomes even more significant which makes the oscillations have a much richer frequency content. As can be seen in Fig. 4.29, the LCO is still bounded between -0.2 m and 1.88 m for the displacement and between -22.4 deg and 27.5 deg for the twist. However, the distinct harmonics cannot be identified anymore. This fact is verifiable by inspecting Figure 4.30 where between frequencies 1.22 rad/s and 20.25 rad/s many other frequencies contribute to the frequency content of the response. The time-histories of the damaged wing for the same air velocity (i.e., $V_\infty = 41$ m/s), show an even more complex response. Figure 4.31 shows that the upper bound of the wing-tip displacement increases to 2.47 m, and the wing-tip twists between -22.9 deg and 28.2 deg. Moreover, Fig. 4.32 shows that no periodic pattern can be identified for this case which would indicate a chaotic behavior.

In short, by comparing phase plots in Figs. 4.22 through 4.32, it can be clearly seen that the complexity of LCO increases with the existence of damage and increasing air velocity. This can be attributed to the larger deformations due to higher air velocity speed and lower stiffness for the damaged wing coupled with the nonlinear effects of the large angles of attack. While for $V_\infty = 37$ m/s the LCO only shows one harmonic for the clean wing, there will be two harmonics for the damage wing. Increasing the speed to $V_\infty = 39$ m/s will result in three harmonics for the undamaged wing, whereas the damaged wing have a more complex LCO. Eventually, at the speed of $V_\infty = 41$ m/s, the angle of attack passes the aerodynamic stall region and the LCO for both damaged and undamaged wing becomes chaotic. However, it remains bounded for both cases.

A similar analysis has been carried out for a wing with a positive layup of $\beta = 45°$

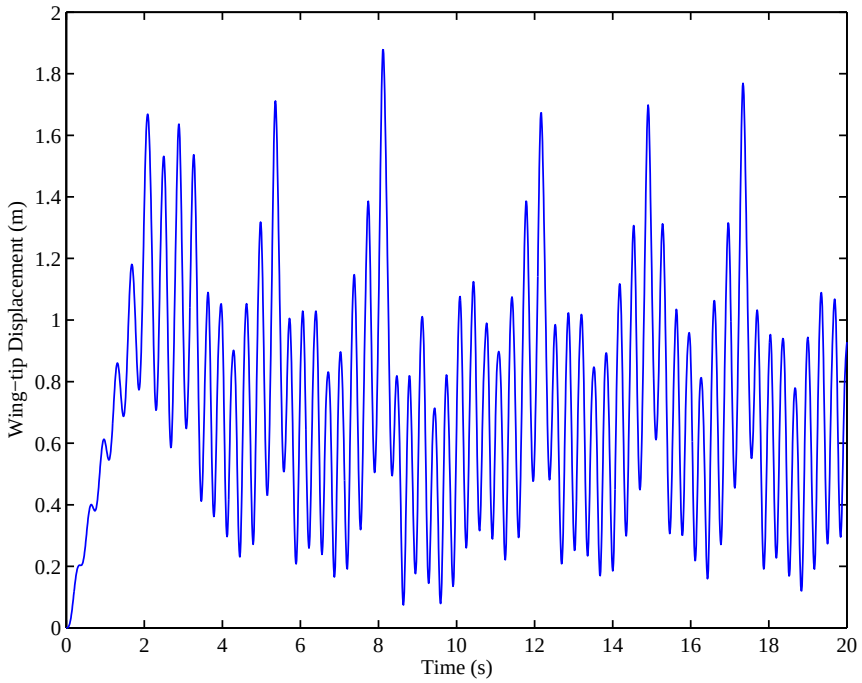

(a) Displacement

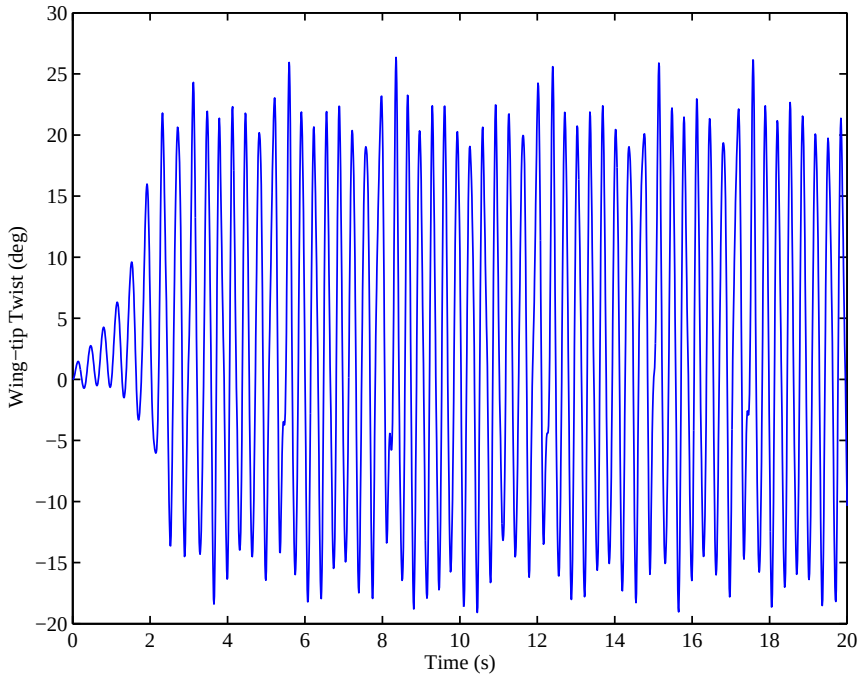

(b) Twist

Figure 4.27: Wing-tip displacement and twist for damaged wing, $V_\infty = 39$ m/s

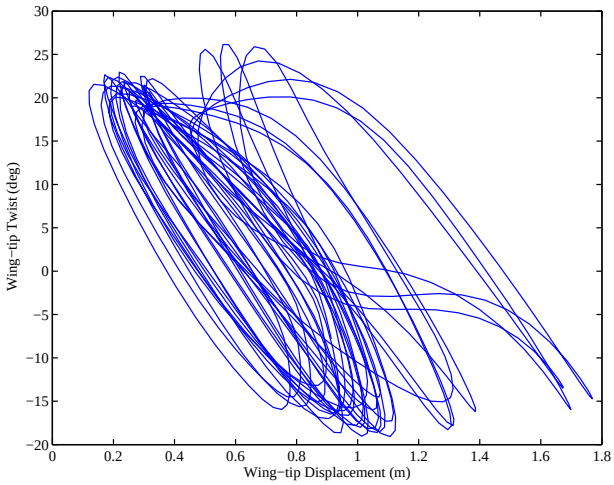

(a) Twist-displacement

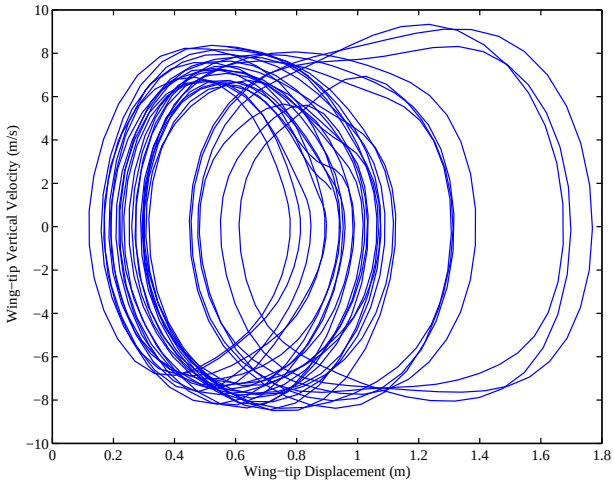

(b) Phase portrait

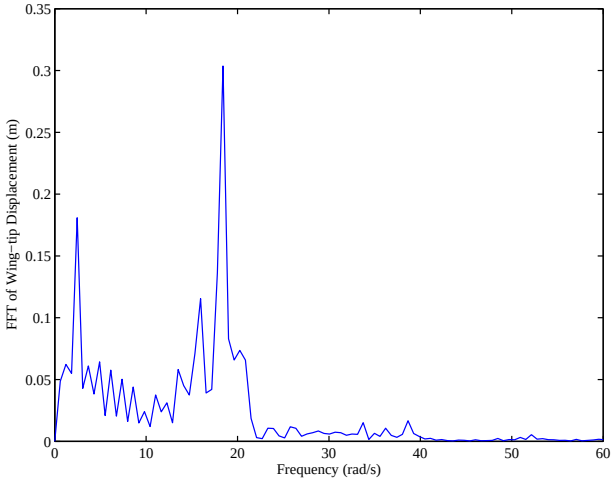

(c) Displacement

Figure 4.28: Phase portraits and FFT for damaged wing, $V_\infty = 39$ m/s

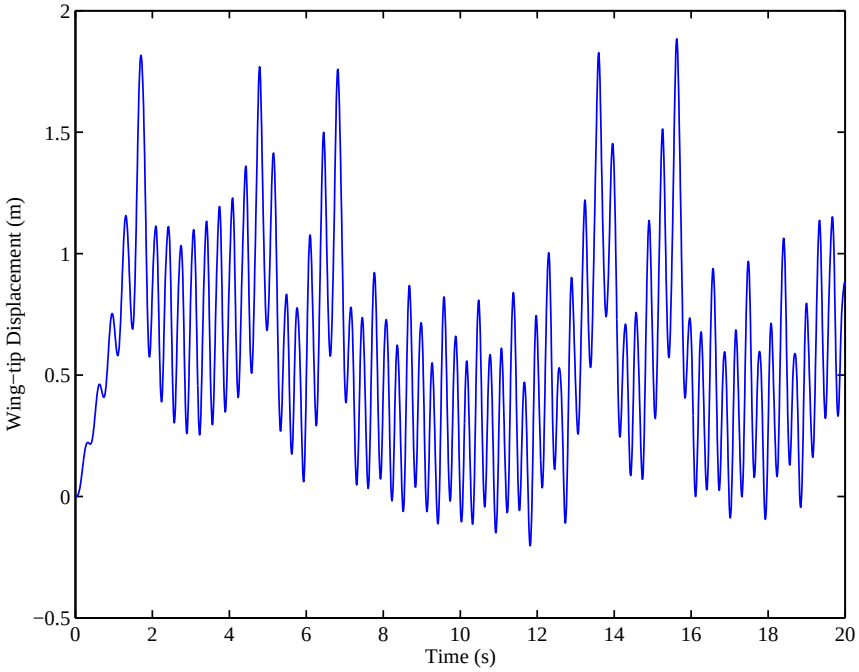

(a) Displacement

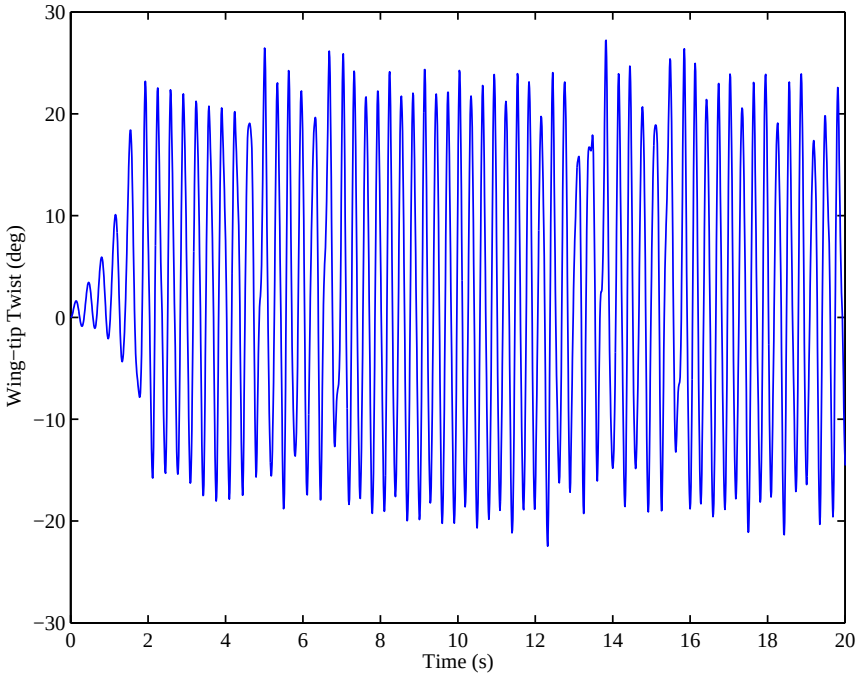

(b) Twist

Figure 4.29: Wing-tip displacement and twist, $V_\infty = 41$ m/s

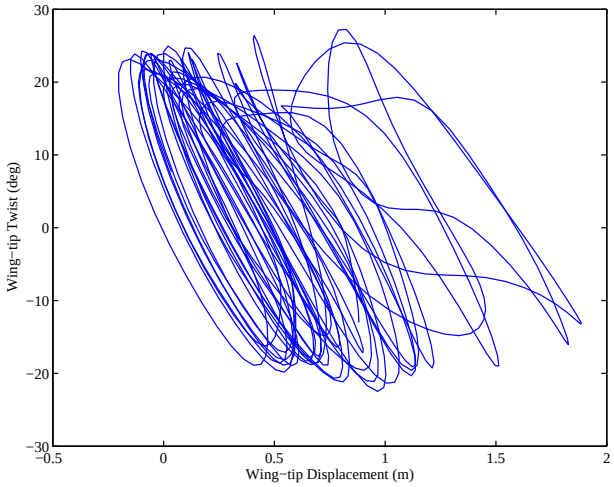

(a) Twist-displacement

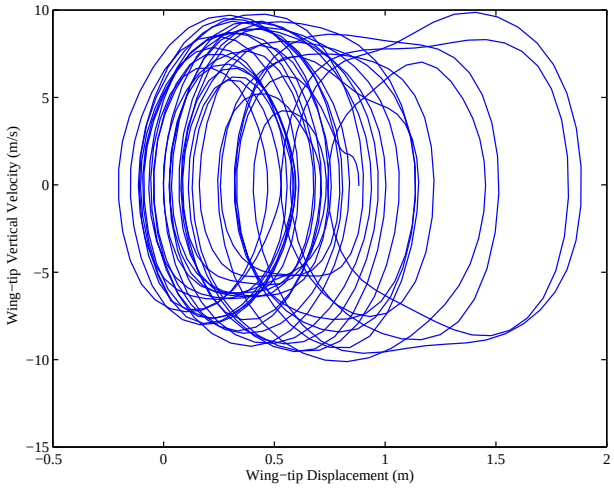

(b) Phase portrait

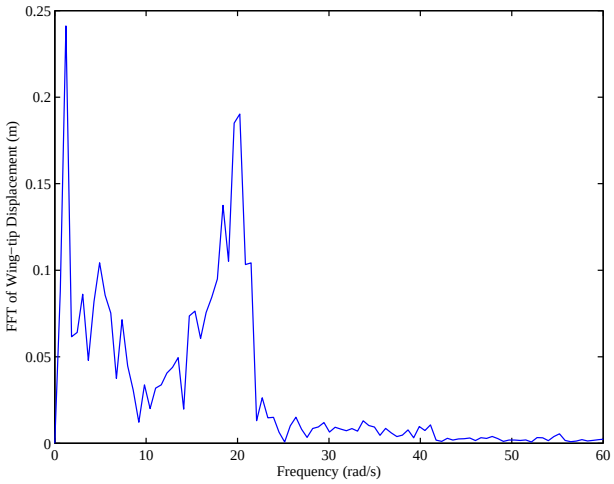

(c) Displacement

Figure 4.30: Phase portraits and FFT, $V_\infty = 41$ m/s

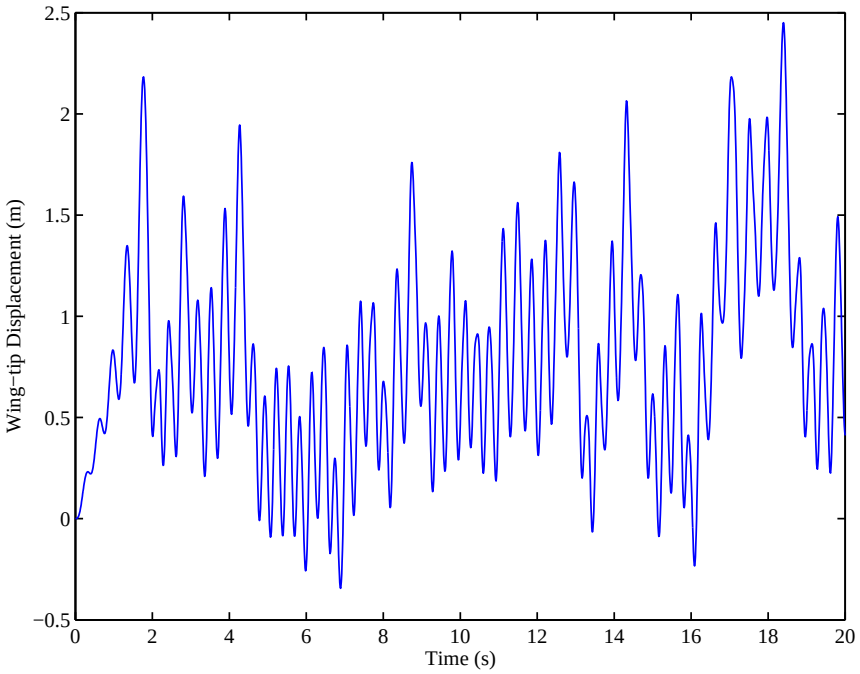

(a) Displacement

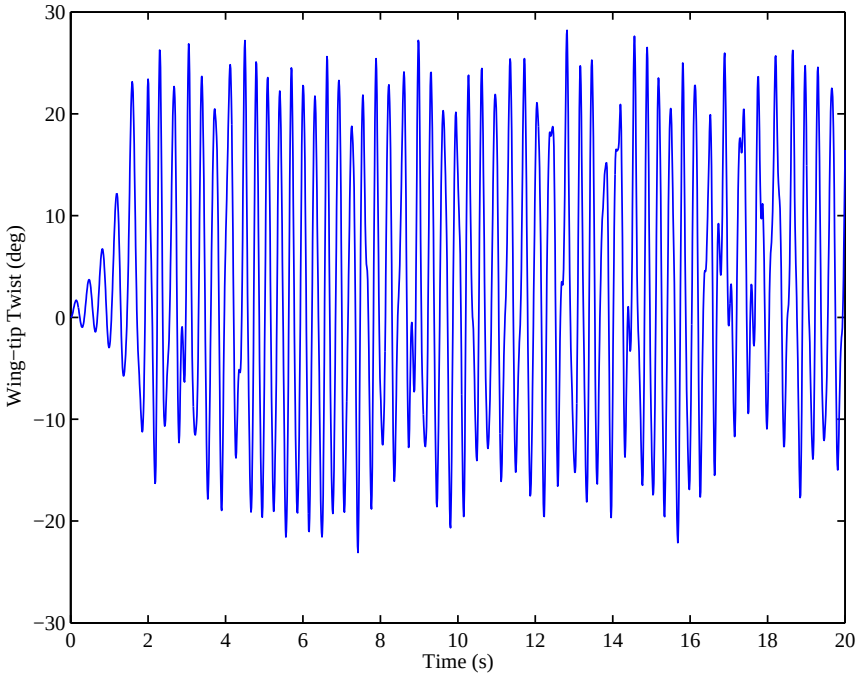

(b) Twist

Figure 4.31: Wing-tip displacement and twist for damaged wing, $V_\infty = 41$ m/s

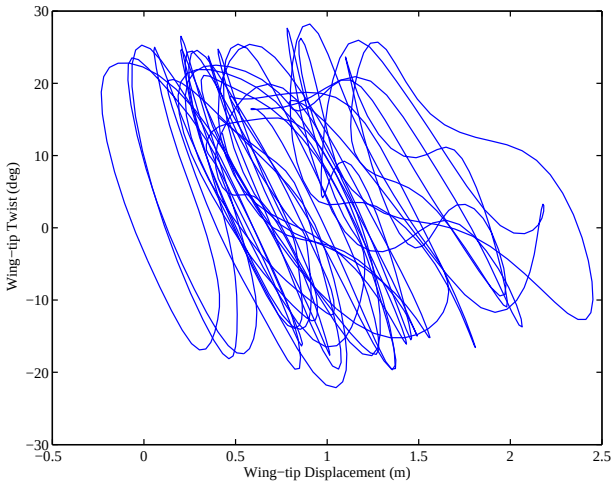

(a) Twist-displacement

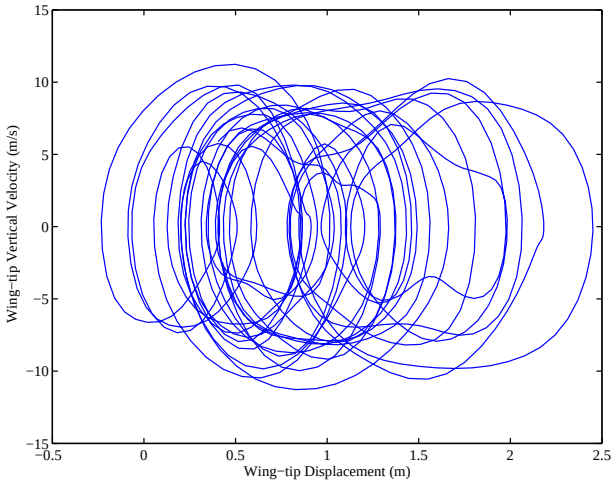

(b) Phase portrait

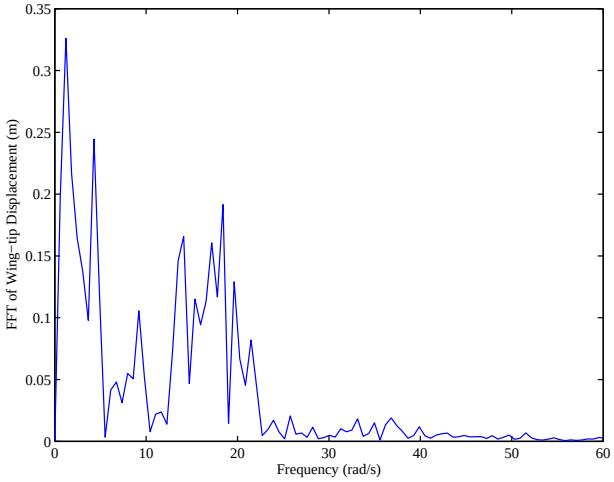

(c) Displacement

Figure 4.32: Phase portraits and FFT for damaged wing, $V_\infty = 41$ m/s.

which provides a negative bending-twist coupling. For the undamaged wing, the simulation was first done for an air velocity close to the linear flutter speed, namely $V_\infty = 56$ m/s. The time histories of tip vertical displacement and twist at this velocity are shown in Fig. 4.35. Although the speed in this case is much higher than the speed for the wing with $\beta = 0°$, the negative bending-twist coupling prevents the wing to deform as mush. As it can be seen in the figure, at the beginning the oscillations grow exponentially and reach to 0.72 m at 4.7 s. However, due to geometric stiffness, the oscillations cannot grow beyond that point and start to subside in amplitude, eventually settling into a stable LCO in which the wing tip oscillates harmonically between 0.09 m and 0.48 m. The same observation is made for the tip twist where the wing oscillates between -22.2 deg and 22.5 deg. In that figure, the existence of LCO is verified by the phase portrait of the wing-tip displacement. FFT plot shows that two harmonics exist where the frequency of 31.8 rad/s is dominant. Because of the higher bending stiffness, the flutter frequency is much higher than that of the wing with orthotropic layup (i.e. $\beta = 0°$). It should be noted that, according to Fig. 4.36, during the stable phase of the LCO, the tip displacement and twist oscillations are out of phase such that the upper limit of the tip displacement, 0.58 m, corresponds to the lower limit of the tip twist, -22.2 deg. This would appear to be the limiting mechanism by which the aerodynamic lift and pitching moment, along with geometric stiffness, would sustain a bounded LCO.

For the damaged wing at the same speed of $V_\infty = 56$ m/s, Figs. 4.33 and 4.34 show that the LCO is qualitatively the same. However, it seems that the damage has slightly decreased the bending stiffness and the bending-twist coupling such that the tip displacement varies between 0.19 m and 0.58 m. Twist remains largely unaffected by the existence of damage and varies between -22.1 deg and 22.6 deg.

Figures 4.37 and 4.38 show that, unlike the case of $\beta = 0°$, increasing the air speed will not result in a chaotic LCO. This is mainly owing to the bending-stiffness coupling

effect which prevents the wing to undergo very large deformations. In fact, as a result of the coupling, a favorable bending moment limits the amplitude of oscillations between -0.08 m and 0.42 m for the stable segment of the LCO at the speed of 57 m/s. In this case, however, two harmonics exist and the one at 31.8 rad/s is dominant.

For the case of a damaged wing, it can be seen in Figs. 4.39 and 4.40 that the two harmonics are formed because of the nonlinear aerodynamic effects. However, since the displacement is not very large, the LCO would not become chaotic, as opposed to the wing with $\beta = 0°$. The tip displacement is bounded between -0.49 m and 0.79 m, while the twist varies between -24.5 deg and 25.5 deg. Figure 4.40 shows that, unlike the undamaged wing, in this case the harmonic at 2.7 rad/s is dominant.

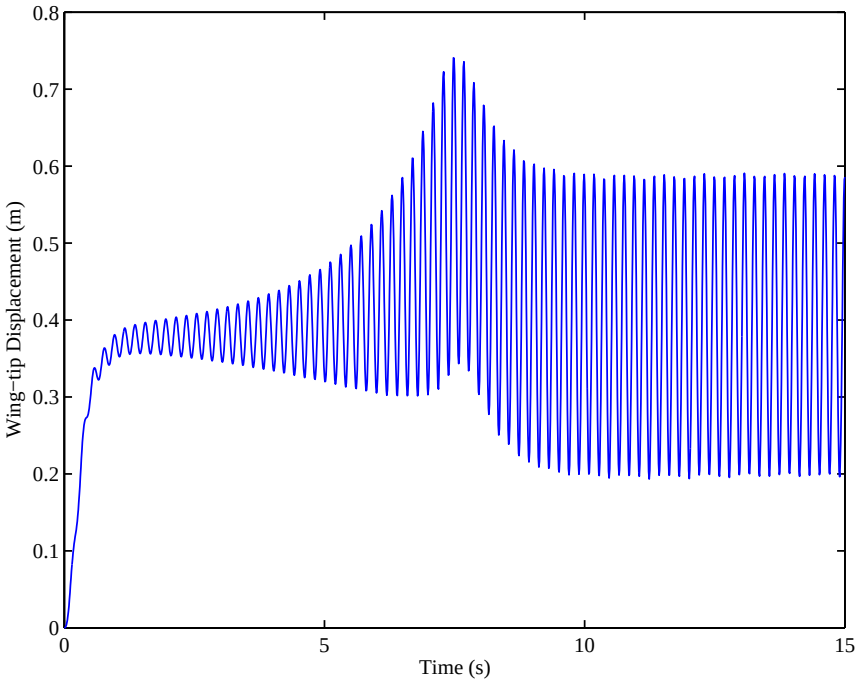

(a) Displacement

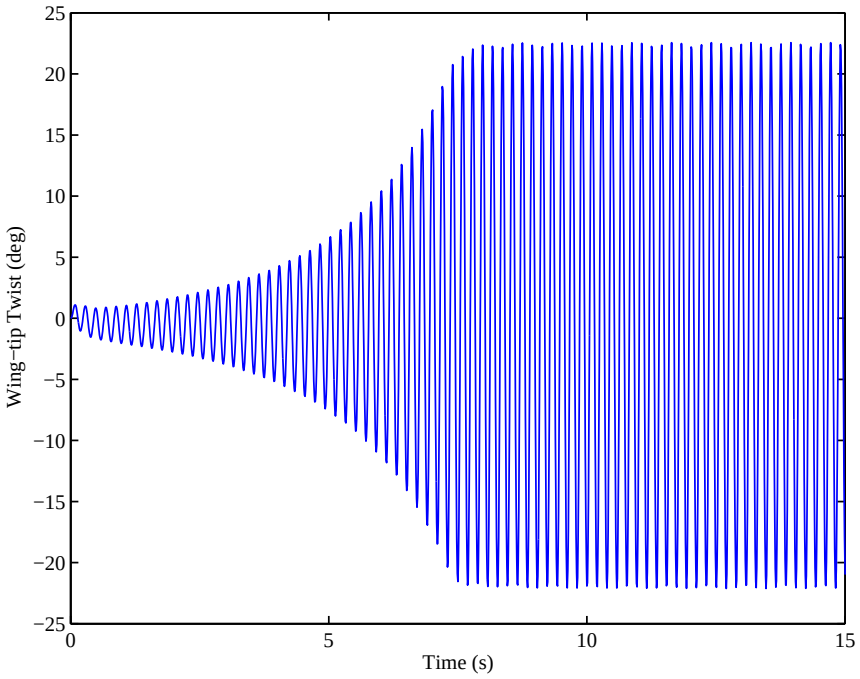

(b) Twist

Figure 4.33: Wing-tip displacement and twist, $V_\infty = 56$ m/s

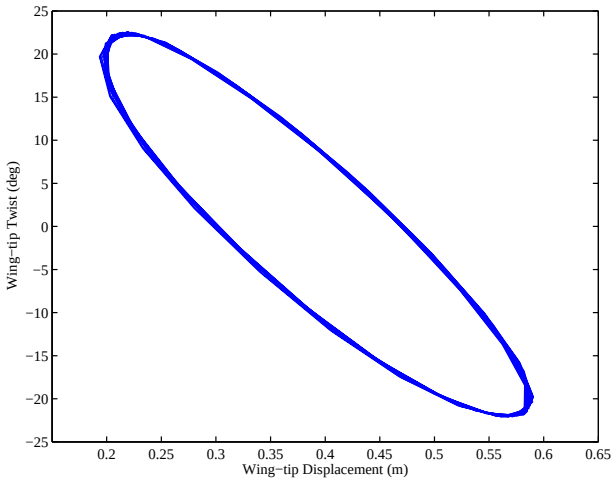

(a) Twist-displacement

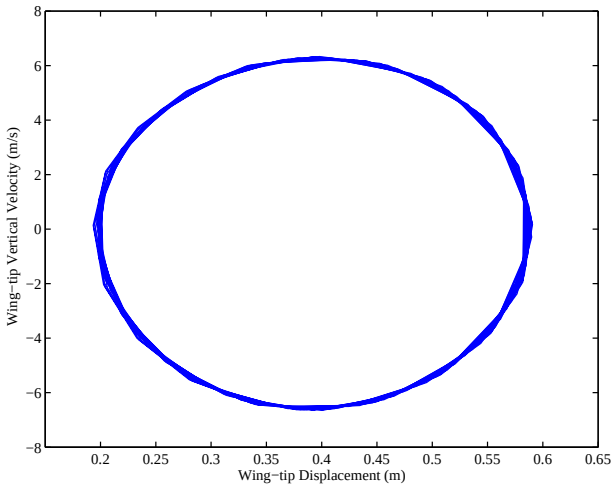

(b) Phase portrait

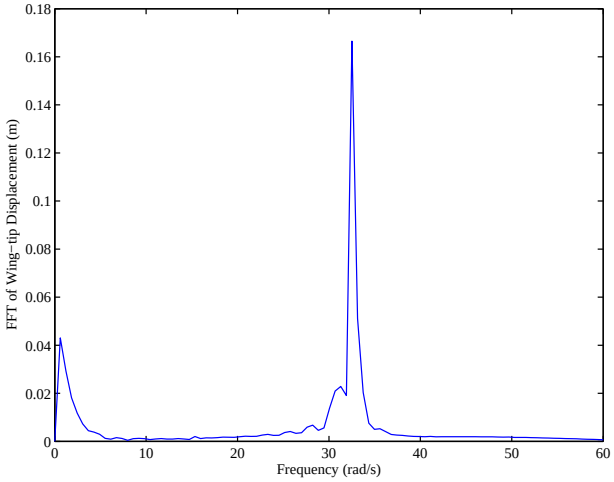

(c) Displacement

Figure 4.34: Phase portraits and FFT, $V_\infty = 56$ m/s

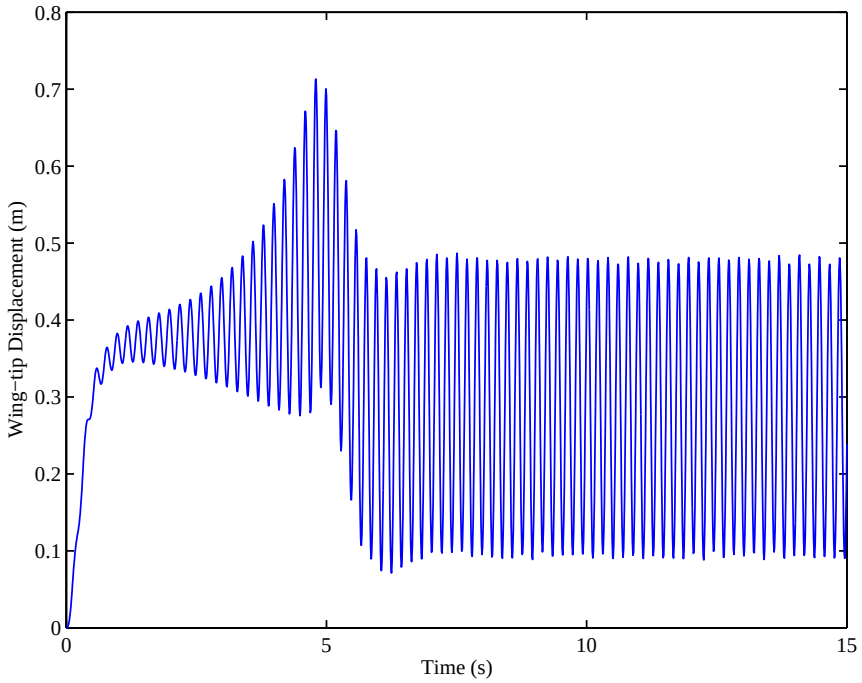

(a) Displacement

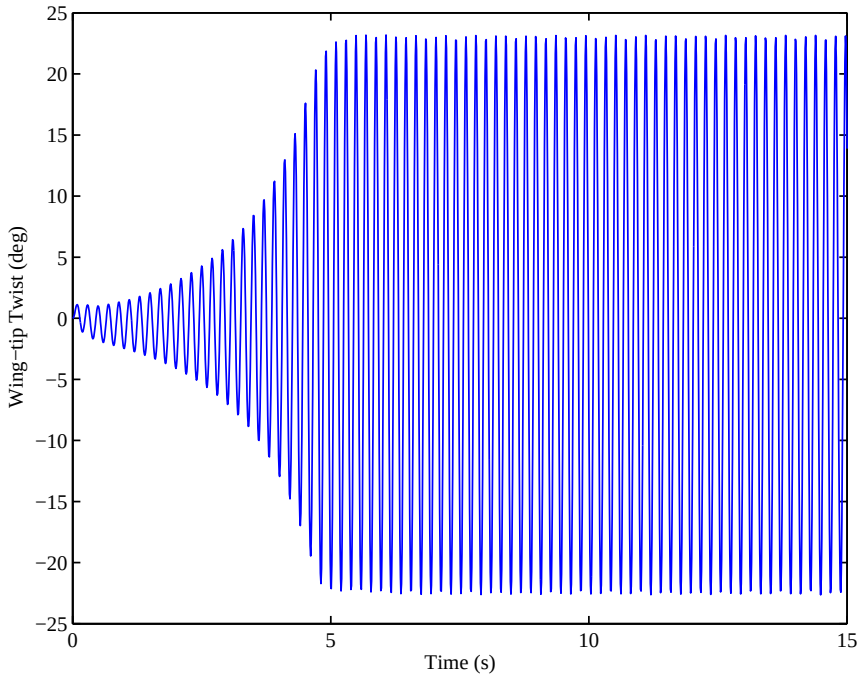

(b) Twist

Figure 4.35: Wing-tip displacement and twist for damaged wing, $V_\infty = 56$ m/s

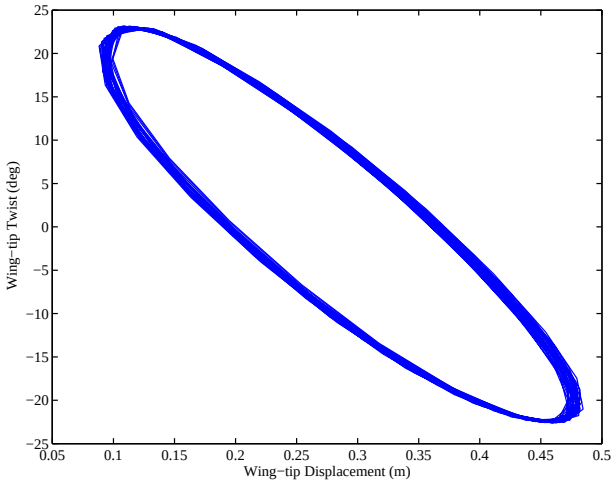

(a) Twist-displacement

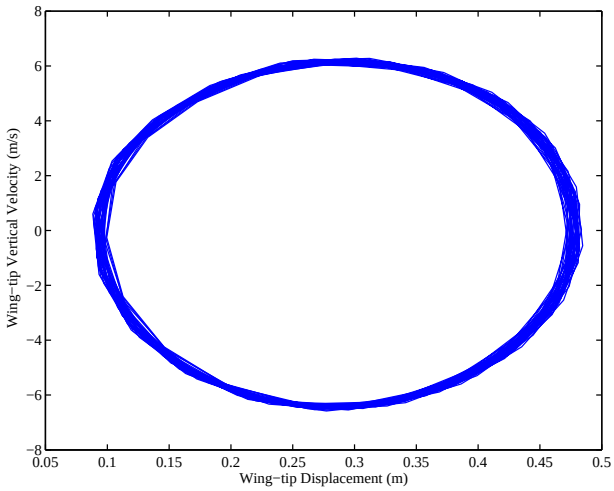

(b) Phase portrait

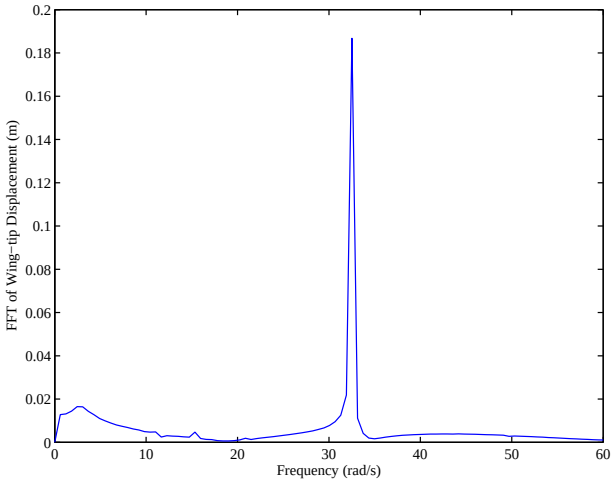

(c) Displacement

Figure 4.36: Phase portraits and FFT for damaged wing, $V_\infty = 56$ m/s

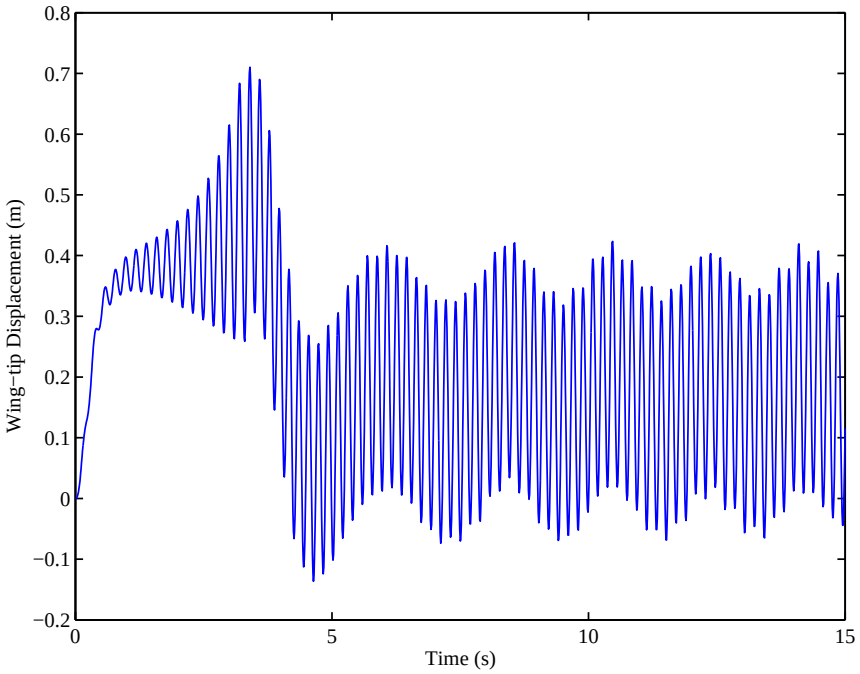

(a) Displacement

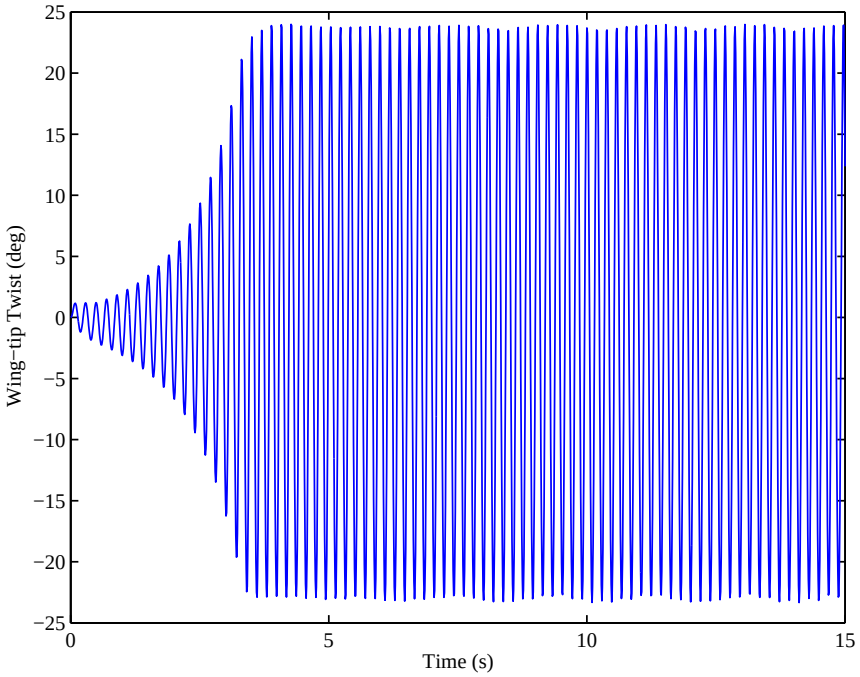

(b) Twist

Figure 4.37: Wing-tip displacement and twist, $V_\infty = 57$ m/s

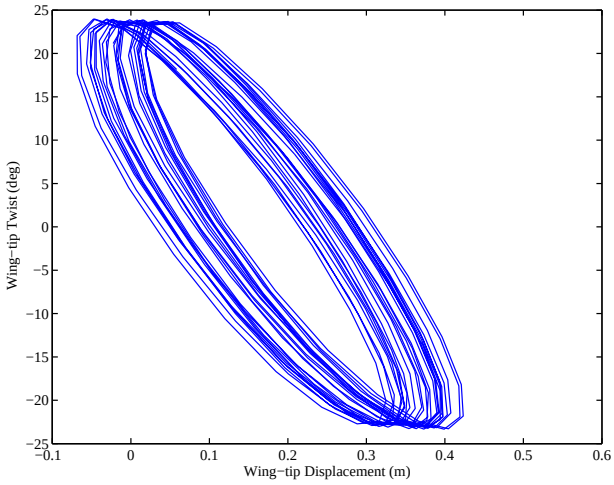

(a) Twist-displacement

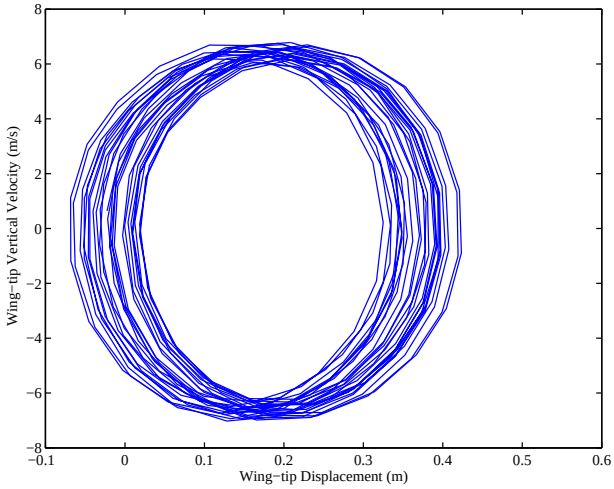

(b) Phase portrait

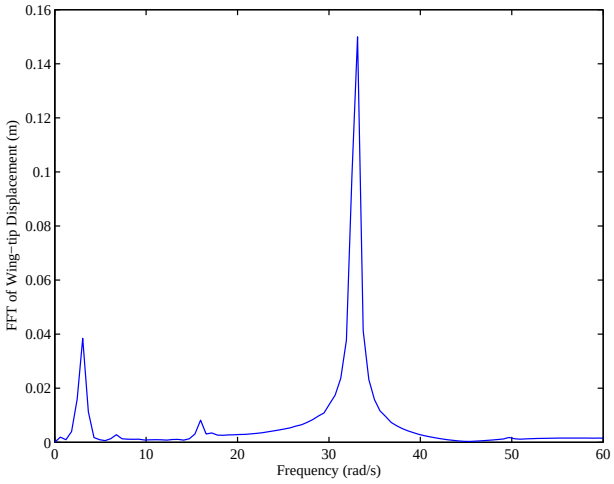

(c) Displacement

Figure 4.38: Phase portraits and FFT, $V_\infty = 57$ m/s

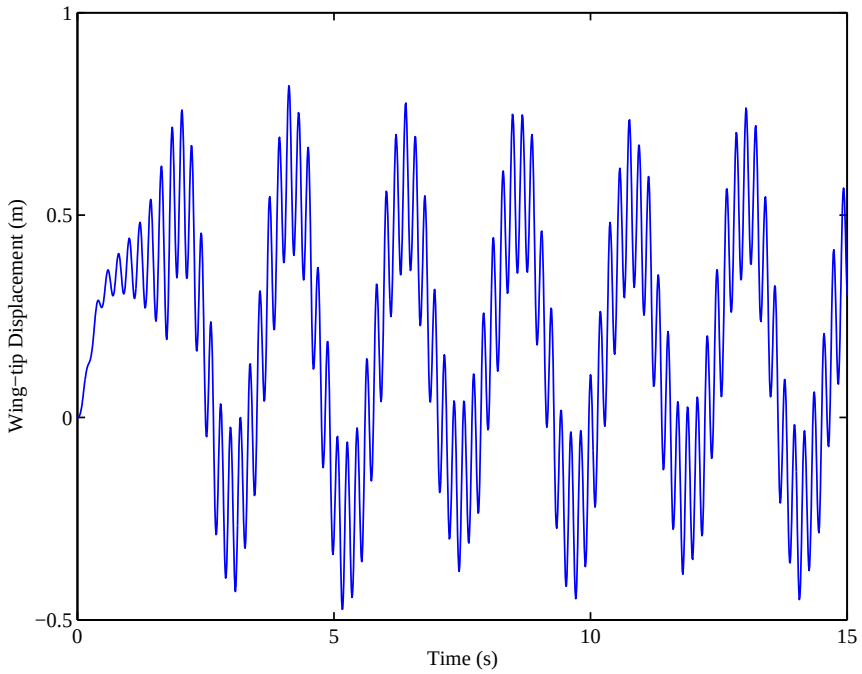

(a) Displacement

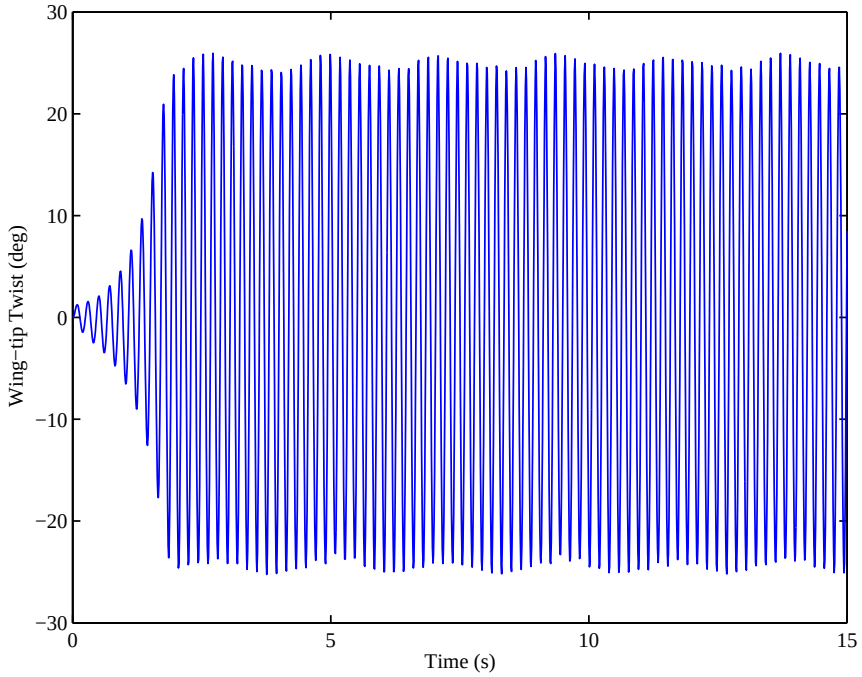

(b) Twist

Figure 4.39: Wing-tip displacement and twist for damaged wing, $V_\infty = 57$ m/s

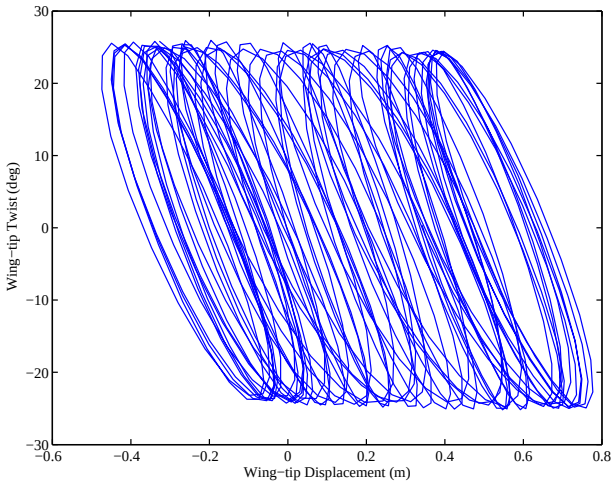

(a) Twist-displacement

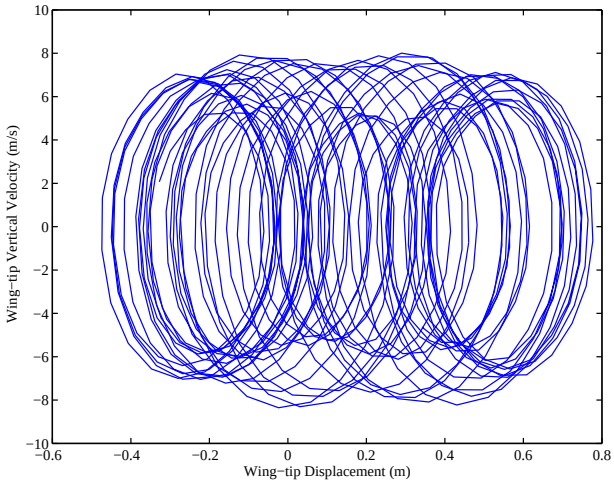

(b) Phase portrait

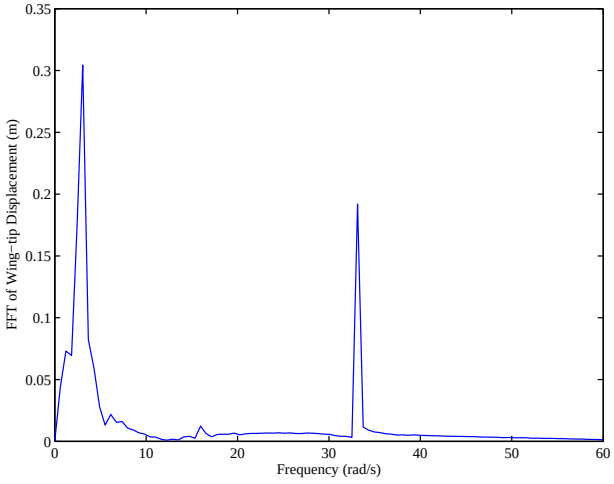

(c) Displacement

Figure 4.40: Phase portraits and FFT for damaged wing, $V_\infty = 57$ m/s

CHAPTER V
FLUTTER SUPPRESSION CONTROL SYSTEM

5.1 Introduction

Flutter, left unchecked, can seriously compromise the structural integrity of a wing and may eventually lead to a catastrophic failure of the aircraft. Both passive and active mechanisms have been proposed by researchers to address the issue of flutter suppression, some of which were reviewed in Subsec. 1.2.3. However, because of the advent of light weight and reliable processors and sensors, active flutter suppression has become more prevalent. Model-based feedback control offers various advantages over the passive control including the reduction of overall weight and increasing the robustness at the presence of structural uncertainty and atmospheric disturbances. Therefore, in this study a feedback control flutter suppression system for HALE aircraft wings is proposed. The joined 3D/1D modeling, developed and studied in the previous chapters, provides an economical and reliable model for aeroelastic analysis and nonlinear simulations. Although this approach drastically reduces the DOF of the model, the model arising from finite element discretization is still prohibitively large for designing a control law. Therefore, there is an obvious need for ROM to keep only a small number of dominant modes and discard other modes with no physical significance. This goal is achieved here by using POD and the method of snapshots. On the other hand, only a subset of state variables are available for feedback through sensor measurements. Hence, even for an ROM, other states need to be estimated. Here a Kalman filter is used to estimated the state variables and send them to the controller to compute the input to the actuators. Therefore, the final controller will be configured in an LQR/LQG framework. To avoid unnecessary complexity of

the control system, the actuator is chosen to be a trailing edge flap which provides the damping forces and moments for suppressing flutter. The effects of the number and location of the sensors and actuators will also be studied in this chapter. The final design must possess enough robustness properties to withstand the structural damages of the kinds studied in the previous chapter. The performance of the flutter suppression control system is investigated through nonlinear time simulation of the joined 3D/1D model with the controller in the loop.

5.2 Reduced Order Model of the Joined Model

The physical and structural properties of the wing model used in this section is described in Sec. 4.3. Dynamical equations of the structural system acted upon by some time-dependent external loads can be describes as

$$\underline{\underline{M}}\,\underline{\ddot{u}}(t) + \underline{\underline{G}}\,\underline{\dot{u}}(t) + \underline{\underline{K}}\,\underline{u}(t) = \underline{F}(t). \tag{5.1}$$

The full order $\underline{\underline{M}}$, $\underline{\underline{G}}$, and $\underline{\underline{K}}$ matrices are available from the FEM model solved by ABAQUS. They can be requested as an output file with *.mtx* extension at the end of an static analysis. The joined 3D/1D model has 26400 DOF. The matrices, therefore, are highly sparse 26400×26400 matrices. In order to use POD, the impulse response of the wing is obtained by loading the wing the tip for a very short duration of time with two transverse forces as well as a twist moment. A dynamic simulation using ABAQUS is then performed to find responses for all DOF. The time step must be small enough to capture all relevant frequencies. Hence, a fixed time-step equal to 0.01 is used. In order to extract only first six dominant modes of the system, six snapshots are chosen. Time histories for all nodes for these six time points are put in a matrix of snapshots, Eq. 2.102, with six columns. Following Sec. 2.5, singular value decomposition is then performed on this snapshot matrix to extract the six

Table 5.1: Natural frequencies of the joined and reduced-order models (rad/s)

Mode num.	Joined 3D/1D freqs.	POD freqs. I	POD freqs. II
1	17.5655	17.5655	17.5655
2	35.3346	35.3346	35.3241
3	109.6931	109.6931	109.5254
4	214.4486	214.4492	—
5	298.5263	298.5343	—
6	304.1003	304.3762	—
7	573.0332	—	—
8	586.2803	—	—
⋮	⋮	—	—

base vectors of the reduced-order system. The natural frequencies of the joined and ROM are presented in Table 5.1. As can be seen in the table, the frequencies of the reduced-order model agree very well with those of the first six frequencies of the joined model. Since the contributions of high-frequency modes are much smaller than those from the low-frequency modes, only the first three modes are picked for the control system design using a matrix of snapshots with only three columns. As for the previous case, the results in Table 5.1 show that the frequencies agree very well with those from the joined model. Therefore, the ROM used for controller design will have only 3 DOF.

The same procedure can be followed for the wings with different layups with structural couplings. The results are not presented here in order to avoid unnecessary repetition.

5.3 Trimming Using the Control System

Since the controller designed in the previous section adds artificial damping to the system, whereby damping out the oscillations of the wing, for a specific air velocity it can be employed as a trimmer to bring the wing, which is initially at rest, to the final configuration. In order to accomplish this task, the controller is active throughout the

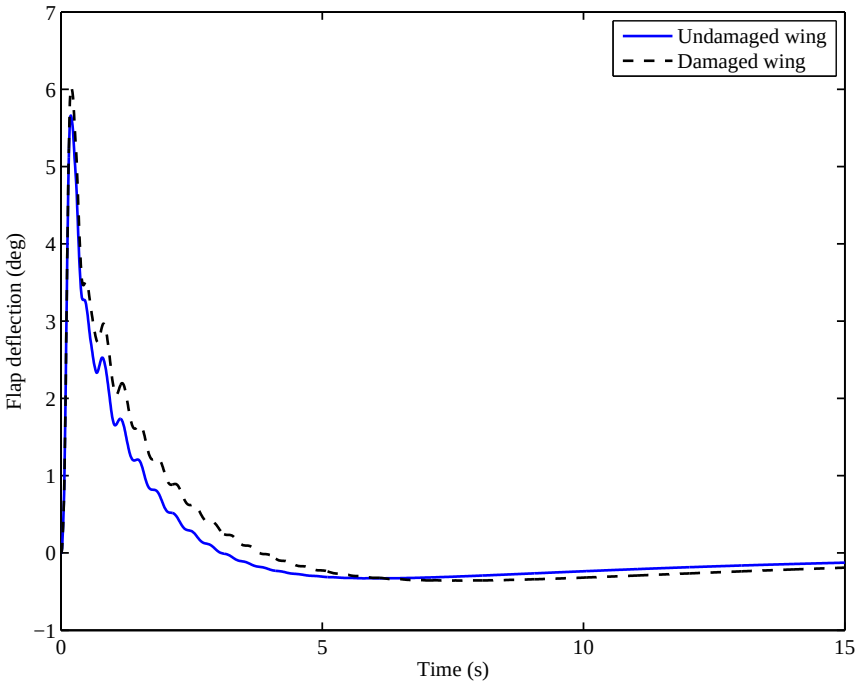

Figure 5.1: Flap deflection for trim

simulation and prevents the wing from undergoing flutter condition from the onset by driving the wing-tip vertical velocity and twist rate to zero. Therefore, the final configuration characterized by steady state deformations and zero velocities represent the trim condition.

Two test cases are considered in this section and the simulation results are compared. Here the results for the baseline configuration, with no structural coupling, are presented. The first case is an undamaged wing with the air velocity, V_∞, equal to 36 m/s which is slightly above the flutter speed. The second case is the same wing with a chord-wise crack at the leading edge with crack length to chord ratio of 0.2, at the same air velocity, i.e. $V_\infty = 36$ m/s. It should be noted that for this analysis, as it was the case for the flutter analysis, only the effect of an existing damage is considered and the damage is not allowed to grow.

The flap deflection to trim is shown in Figure 5.1. At the beginning, a large control input is required to move the wing from the rest. Therefore, the flap deflection is

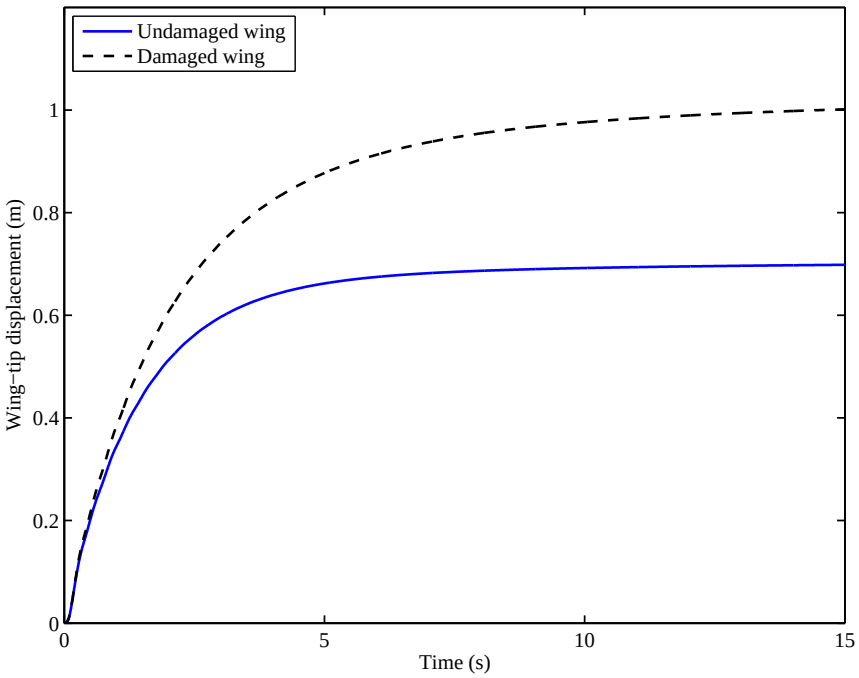

(a) Displacement

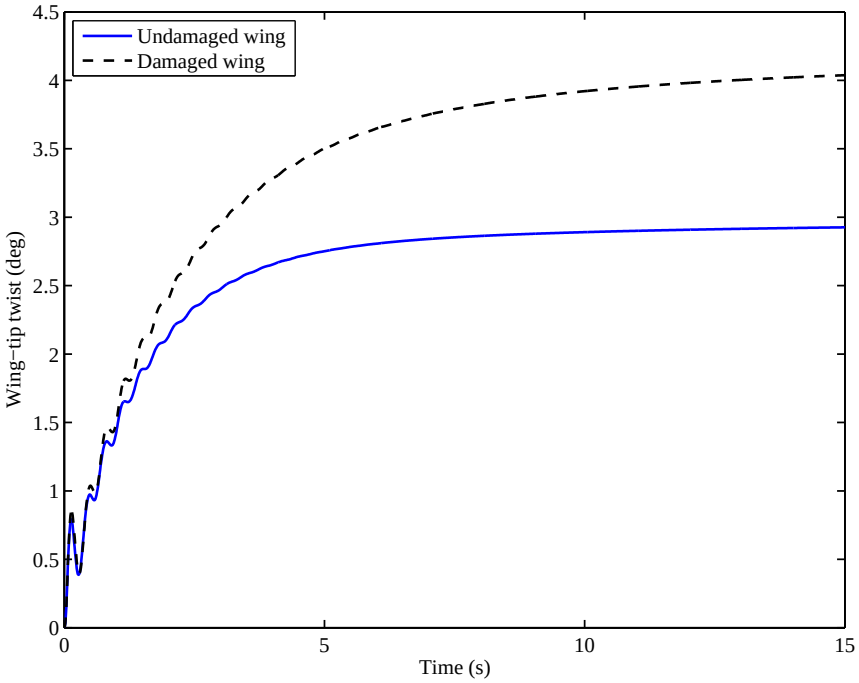

(b) Twist

Figure 5.2: Wing-tip displacement and twist for trim

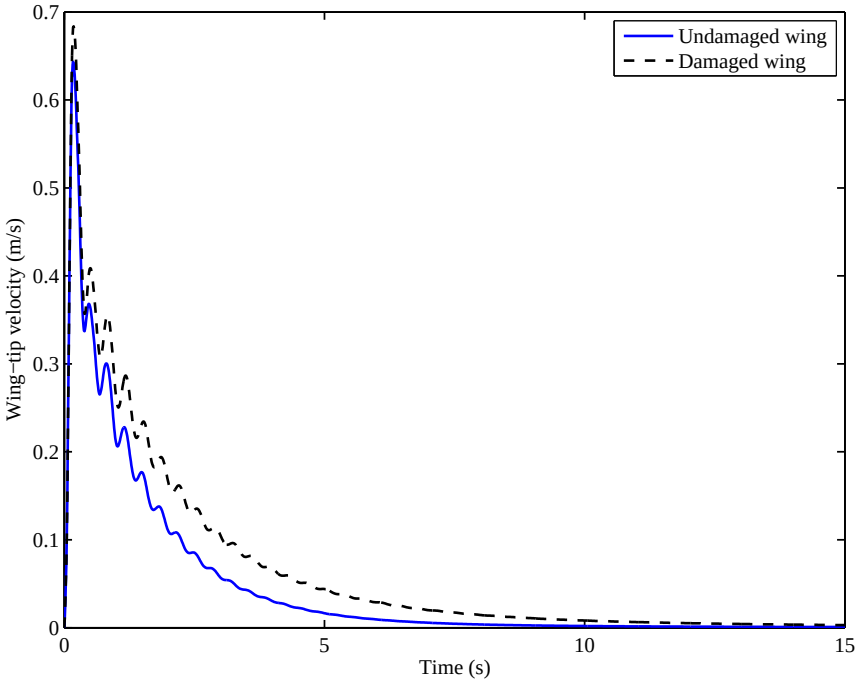

(a) Velocity

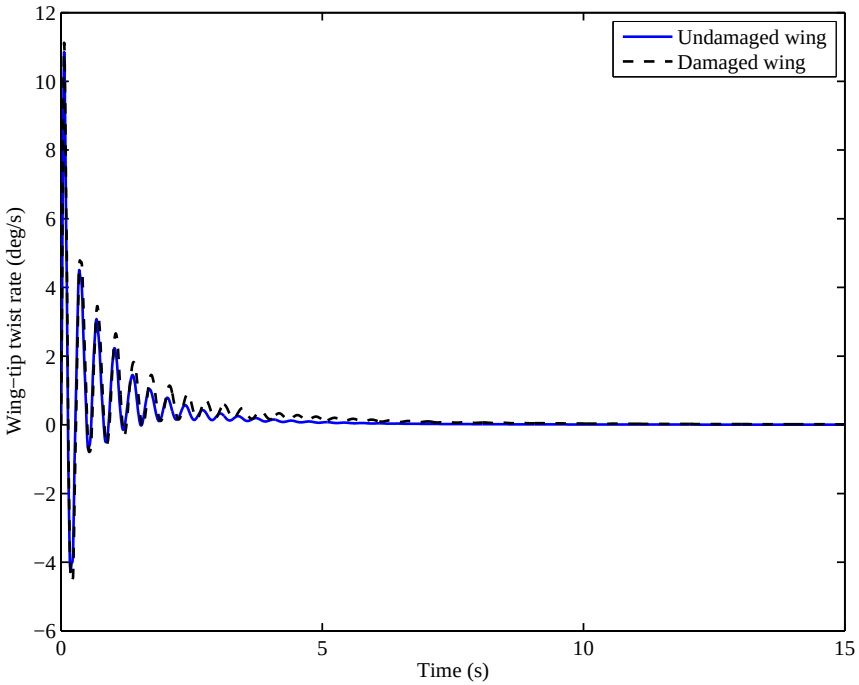

(b) Twist rate

Figure 5.3: Wing-tip velocity and twist rate for trim

initially big and peaks at 0.19 sec. It reaches to 5.65 deg and 6.05 deg for undamaged and damaged wings, respectively. However, the flap deflection decreases afterward and eventually approaches zero after trimming the wing and suppressing the oscillations. Figure 5.2 shows the simulation results for the wing-tip displacement and twist for both damaged and undamaged wings. It can be observed from the figure that the control system has been able to bring both cases to the trim condition. The trim condition is equivalent to the steady-motion of the aeroelastic system. This fact can be verified by inspecting Figure 5.3 in which the wing-tip velocities are depicted. It is easily verifiable that, despite the initial increase in the velocities which is the result of the transition from the initial configuration, both tip velocities and twist rates are eventually driven to zero by the control system. Inspecting Figure 5.1 reveals that the flap deflections for both damaged and undamaged wings are close in magnitude. This implies that the control forces and moments applied on both wings must be close in magnitude as well. However, it can be immediately observed in Figure 5.2 that the steady state condition is achieved slightly faster for the undamaged wing, and although the undamaged wing-tip displacement and twist measures are 0.70 m and 2.96 deg, respectively, those measures for the damaged wing go up to 1.01 m and 4.05 deg, respectively. In fact, the larger steady state deformations for the damaged wing are directly attributable to the stiffness reduction due to the existence of the crack.

5.4 Flutter Suppression

In this section the performance of the control system is evaluated for suppressing flutter. To this end, the wings studied in Sec. 5.3 are considered here. The air speed is also slightly above the flutter speed for the undamaged wing and is the same for both damaged and undamaged wings, i.e., $V_\infty = 36$ m/s. However, instead of having the controller on from the outset, as was the case for trimming, it is initially off, which allows the oscillations build up and undergo flutter. After 10 s, when the oscillations

are settled into a stable limit cycle, the controller is turned on to suppress the flutter. The task of flutter suppression system is to drive the wing-tip velocity and twist rate to zero.

Figures 5.4 and 5.5 show the simulation results for the wing-tip displacement and twist, respectively, for both damaged and undamaged wings. In order to highlight the effect of the flutter suppression system, in these figures, the results for the uncontrolled wings are overlaid on top of those of the controlled wings. The results for the velocities and twist rates are not shown here for the sake of brevity.

As can be seen in Fig. 5.4, if the controller remains off throughout the simulation, the wing-tip oscillations will eventually settle into a stable limit-cycle, such that the wing tip would oscillate between 0.51 m and 0.84 m for the undamaged wing, and between 0.55 m and 1.21 m for the damaged wing. The same situation holds to be true for the wing-tip twist. Figure 5.5 shows that while the twist angle for the uncontrolled wing is between -6.55 deg and 11.40 deg for undamaged wing, it would oscillate between -9.95 deg and 20.45 deg for the damaged wing. However, since the controller will be on after 10 sec, the feedback mechanism provides additional damping to the system and the the fluctuations will be suppressed for both wings. It can be verified from the figures the flutter is damped out after that. The steady-state will be the same as that of the trim condition, considered in Sec. 5.3.

The flap deflection, depicted in Fig. 5.6, is also worth noting. To have a clear view of the transient phase of the control, only the segment between 9 s and 17 s is shown in the figure and the reset of the flap deflection to zero is not shown. Comparing Figs. 5.6 and 5.1 reveals that whereas the flap deflections for trimming for damaged and undamaged wing are close in magnitude, it is no longer the case for the flutter suppression. While the flap deflection for the undamaged wing varies between -5.05 deg and 7.65 deg, the damaged wing needs a much bigger control effort and the flap deflects between -10.62 deg and 17.72 deg, which is more than twice as much. This is

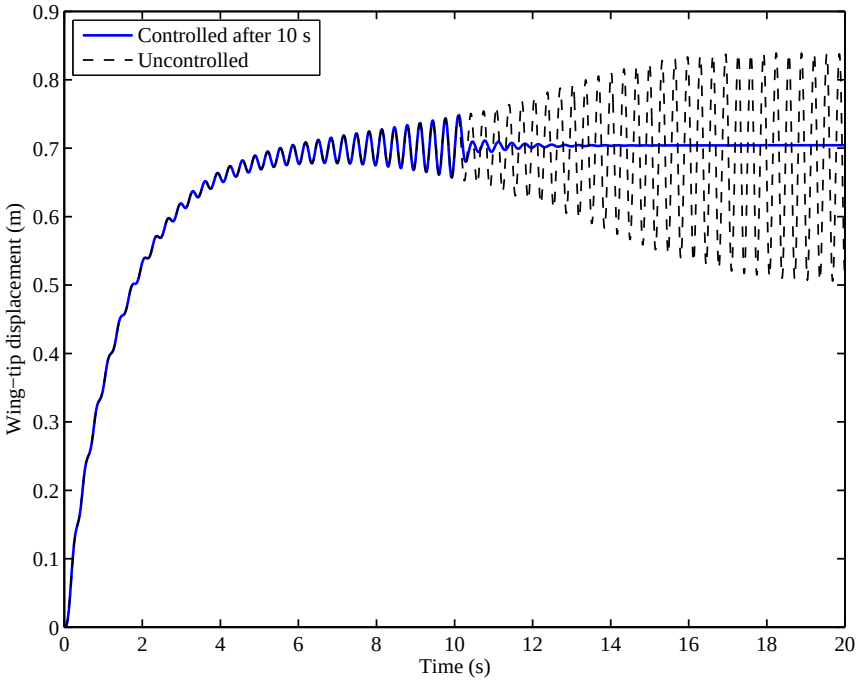

(a) Undamaged wing

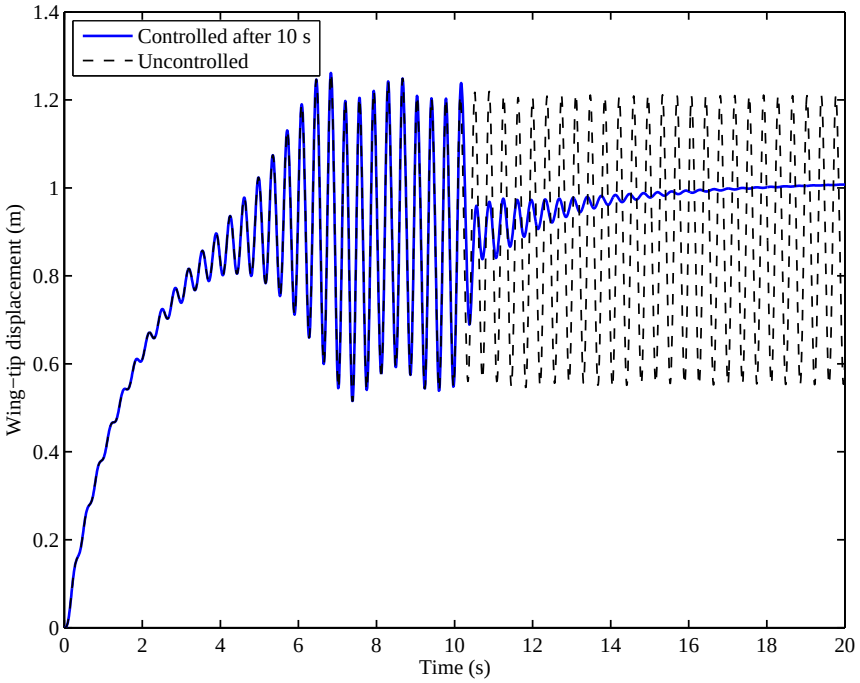

(b) Damaged wing

Figure 5.4: Wing-tip displacement for flutter suppression

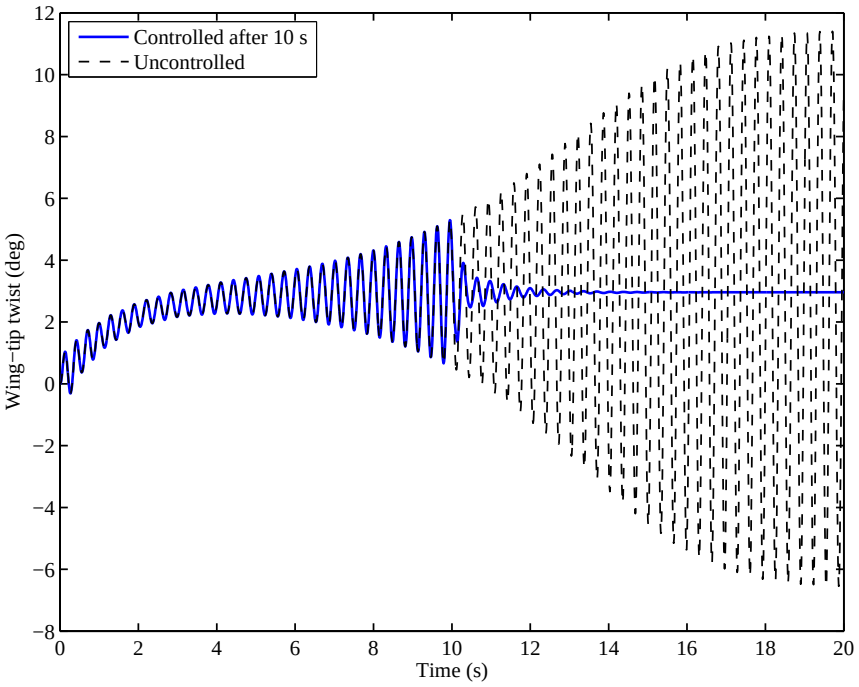

(a) Undamaged wing

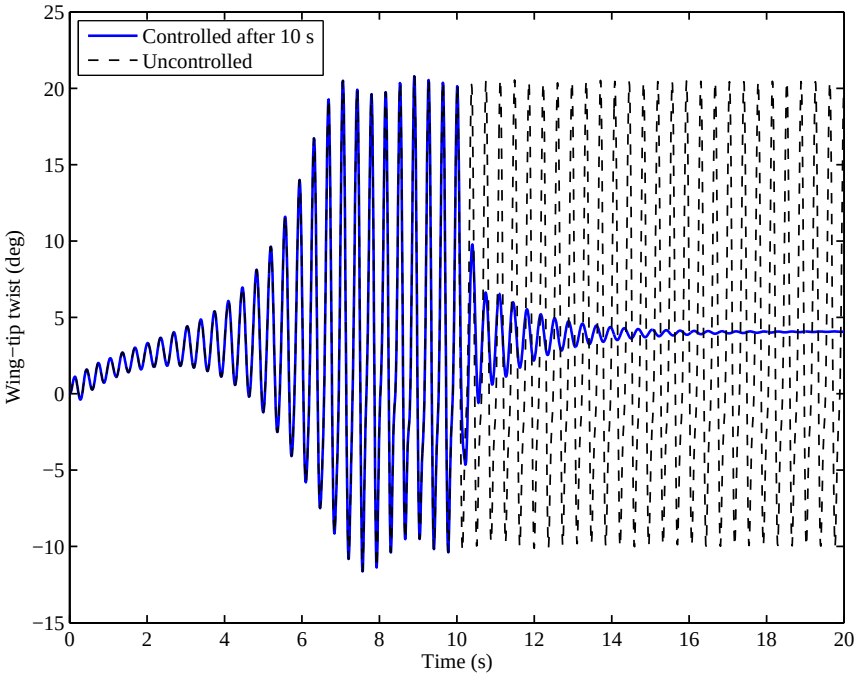

(b) Damaged wing

Figure 5.5: Wing-tip twist for flutter suppression

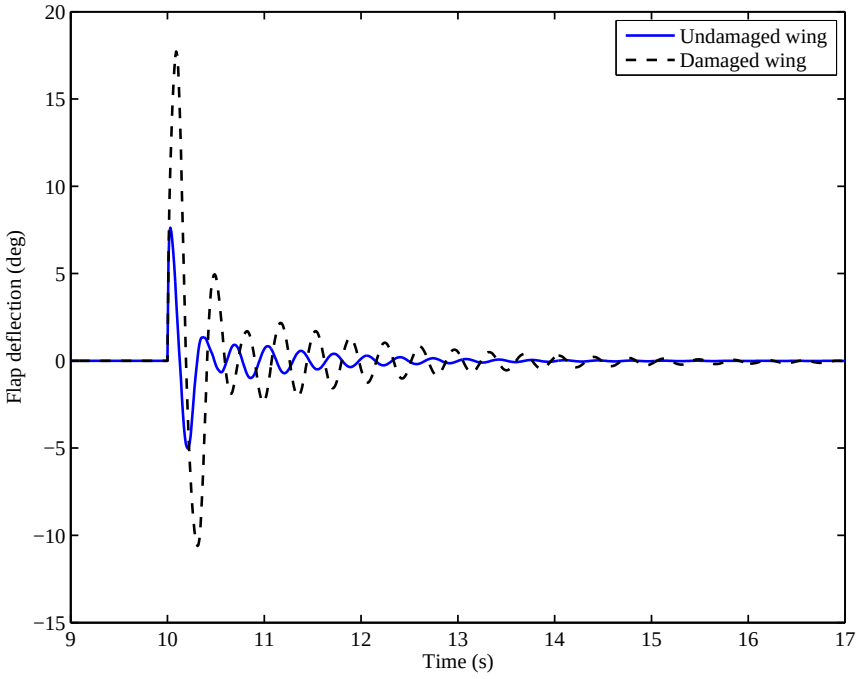

Figure 5.6: Flap deflection between 9 s and 17 s for flutter suppression

due to the fact that, compared with the damaged wing, the limit cycle oscillations for the undamaged wing have a lower amplitude and a lower acceleration which requires a smaller force and moment. Hence, a smaller flap deflection is sufficient to compensate. However, even at the presence of a crack, by turning the flutter suppression system on during the flight the designer can ensure that flutter will not take place.

The performance of the flutter suppression system can be negatively affected by a decrease in the control effectiveness. This may occur as a result of a partial loss of the control surface due to damage or a mechanical system malfunction. The effect is studied here by reducing the flap control power, $C_{l\delta}$. Two cases are simulated for the damaged wing. The simulation results for the wing-tip displacement and the flap deflection are presented in Figs. 5.7 and 5.8, respectively. As can be seen in Figure 5.7, when the control effectiveness is decreased by 25% of its nominal value, the control system would still be able to suppress the flutter, though it would take longer before the oscillations are damped out. Figure 5.8 also proves that the control effort is also much higher for the case of partial loss of flap control power, such that the flap deflects

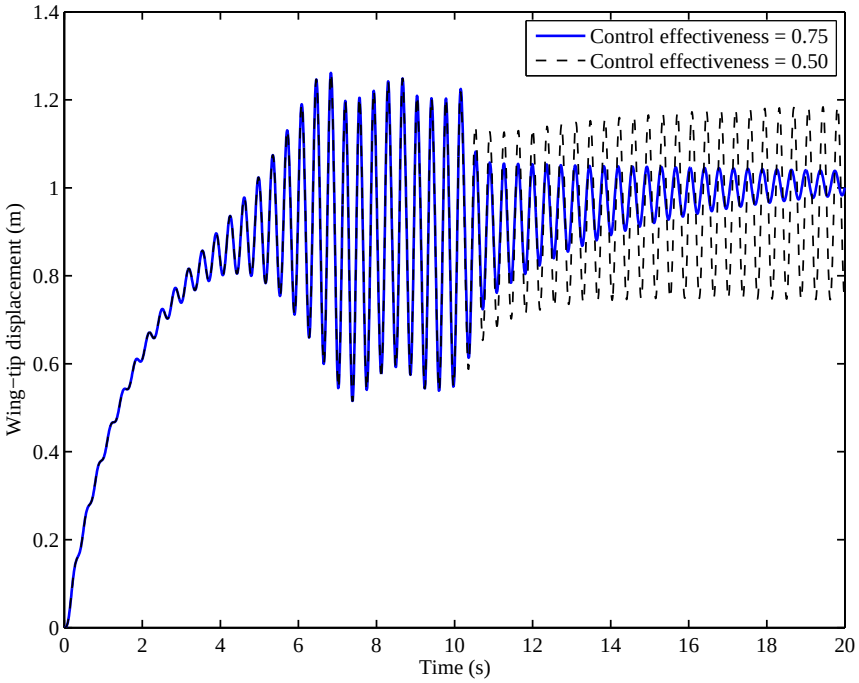

Figure 5.7: Tip displacement for reduced control effectiveness

between -18.25 deg and 27.70 deg. The situation becomes even more problematic by a further loss of control power, such that when the flap loses 50% of its control power the control system is no longer able to completely suppress the flutter. In that case, the control system can only reduce the amplitude of oscillations so that the wing settles into a new stable limit cycle with a lower amplitude between 0.78 m and 1.19 m.

So far, while designing and analyzing the performance of the control system, it was always assumed that both sensor and actuator were located at or near the wing-tip. This can be beneficial, as the wing motions are more pronounced near the wing-tip and they can be measured more easily by sensors for feedback. Also, a smaller control effort may be required as an applied shear force near the tip produces a larger bending moment on the wing. It is, however, not always possible due to the system design and integration considerations. Therefore, flap and sensors might be non-collocated. While studying the effects of flap/sensor non-collocation on the performance of the

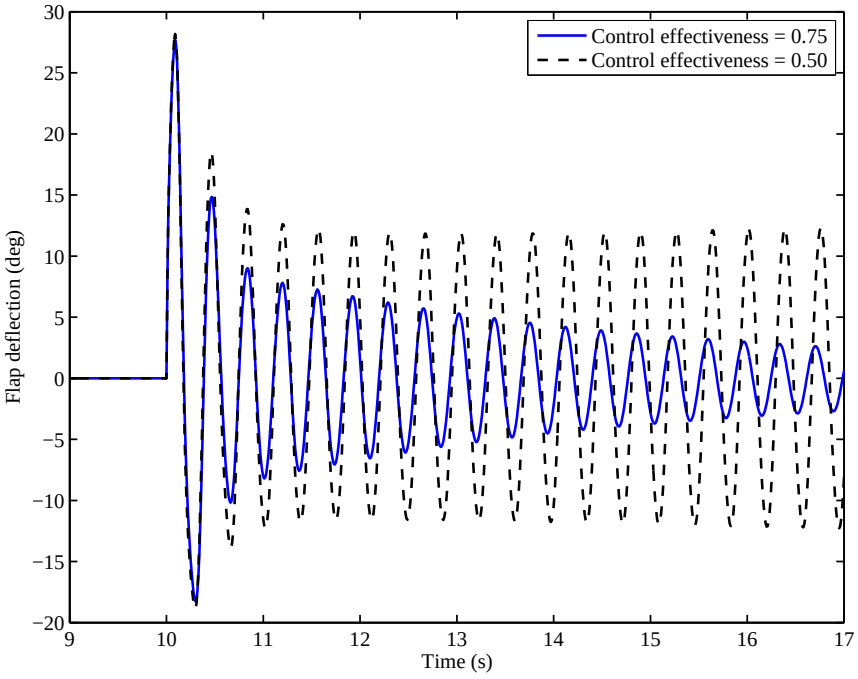

Figure 5.8: Flap deflection for reduced control effectiveness

controller, it was found that the system is not sensitive to the location of the sensor, and as long as the sensor can provide the control system with velocity measurements, the flutter suppression system would be able to accomplish the intended task. This is partly because the first structural modes are dominant for the present flutter scenario and there are no structural nodes along the span. However, the situation is different for the flap location. Figures 5.9 and 5.10 show the simulation results for two different flap locations along the span of the damaged wing, with the sensor location fixed at the wing-tip. It can be seen from Fig. 5.9 that, moving the flap further towards the root, will have a degrading effect on the controller performance which is akin to the loss of the flap control power. Therefore, when the flap is located at 25% of the span, the controller fails to effectively suppress the oscillations, and it can only partially reduce the amplitude of fluctuations. This might be attributed to the fact that the controller bending moment would be reduced by shortening the distance between the control force and the wing-root.

Figure 5.10 also shows similar behavior to Fig. 5.8, though the control effort is

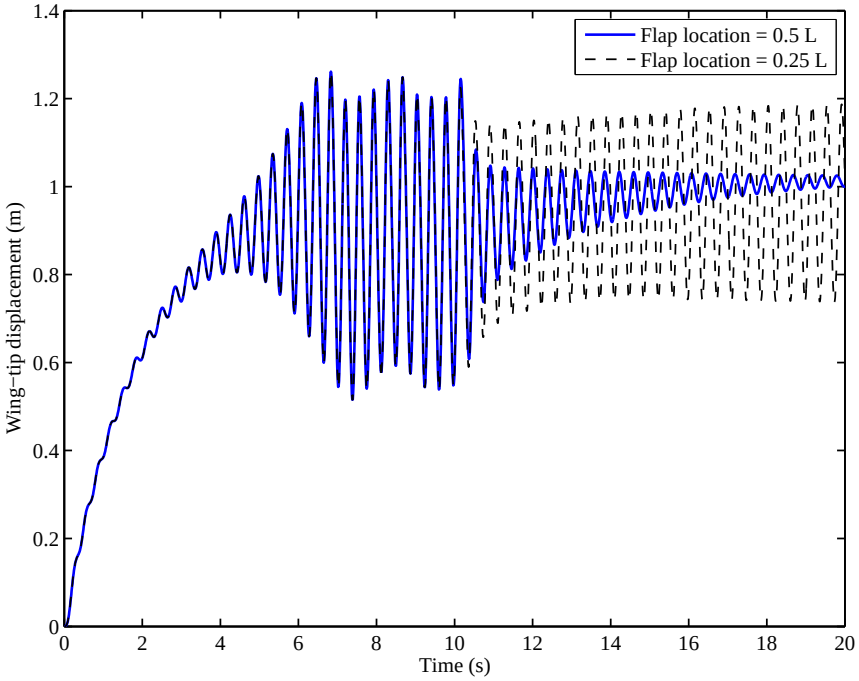

Figure 5.9: Tip displacement for noncollocated sensor and actuator

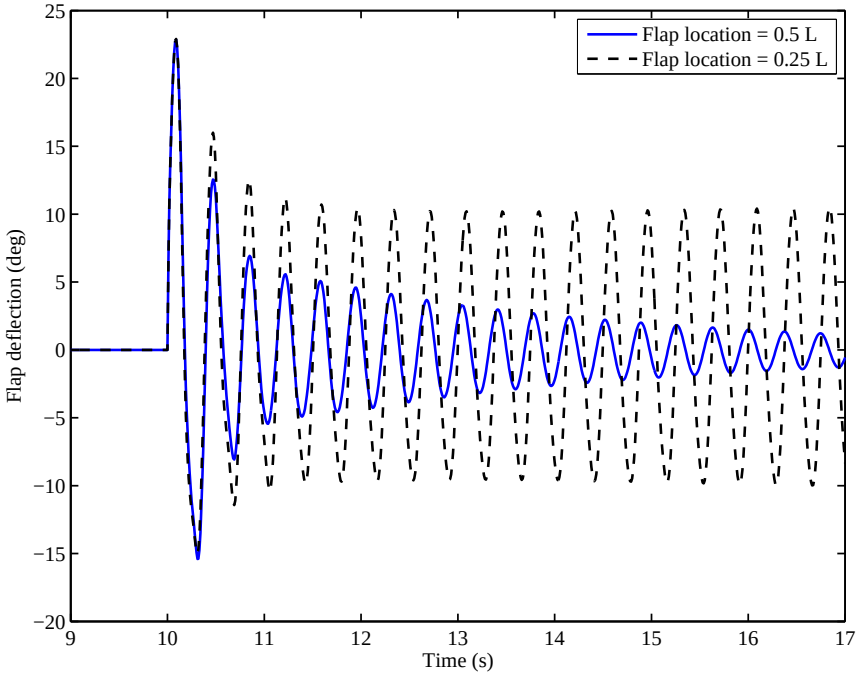

Figure 5.10: Flap deflection for noncollocated sensor and actuator

slightly lower in the former. To avoid unnecessary repetition, the results for the twist and velocities, as well as undamaged wing, are not presented here.

A few points regarding the amplitude of the flap deflections must be noted. Firstly, the actuator saturation is not considered while designing the controller. Therefore, the flap deflection needed might exceed what the actuator can actually deliver. Secondly, the controller has very high authority which makes the flap deflection large. By extending the flap along the span, the actual flap deflection can be made smaller. The effects of these factors must be considered in any actual implementation of the controller and they deserve more consideration in future studies.

CHAPTER VI
CONCLUSIONS AND FUTURE WORK

6.1 Conclusions

In this thesis, a joined 3D/1D FE modeling approach was presented for aeroelastic analysis of damaged HALE aircraft wings. Most of the wing structure was modeled using a displacement-based geometrically exact 1D beam model and the damage was encapsulated in a small area modeled as a full 3D continuum. The solid and the beam parts were then rigorously combined using a transformation between the joined nodes of the two models at their intersection. The transformation was derived using the recovery equations of variational asymptotic beam model and employed to eliminate the six DOF of the single joined node of the beam. The proposed approach has the additional benefit of making it possible to use aerodynamic models for aeroelastic analysis, avoiding the use of a computationally expensive CFD method. To compute aerodynamic forces and moments acting on the structure, the finite-state induced flow theory of Peters was integrated with the 1D beam element, providing a nonlinear aeroelastic element capable of static and dynamic analysis. The nonlinear aeroelastic element was coded as a user-defined element, UEL, for a commercial FE software, namely Abaqus, which expedited the analysis by using solving and post-processing capabilities of Abaqus. The model was also used to evaluate the performance of a flutter suppression system, designed using LQR/LQG method. The controller was also coded for use in Abaqus. The findings are summarized as follows.

- *Static and dynamic structural analysis of beam-like structures.* It was shown that the joined 3D/1D approach can greatly reduce the computational cost for beam like structures. The stress analysis showed that although the accuracy of

the results for the joined 3D/1D method is totally comparable to that of full 3D FE analysis, the simulation time was less than one fifth the former. The same was true for eigenvalue analysis. The joined method was also demonstrated to be capable of dealing with damaged structures where the damage was either a crack, modeled using XFEM, or delamination, modeled using cohesive elements.

- *Linear divergence and flutter analysis.* Linear aeroelastic analysis revealed that the presence of damage, in form of chord-wise crack or span-wise skin delamination, can negatively affect the aeroelastic stability characteristics of HALE aircraft wings. It was shown that bigger cracks near to the wing-root have the most noticeable effect on both divergence dynamic pressure and flutter boundary, and the effects of damage will fade away as the crack moves towards the wing-tip. Through a parametric study, it was also demonstrated that a negative bending-twist stiffness coupling can greatly improve the aeroelastic instability conditions for both damaged and undamaged wings.

- *Nonlinear divergence.* It was shown that, a linear analysis would over-predict the divergence dynamic pressure, for both damaged and undamaged wings. Although a linear eigenvalue analysis cannot differentiate between a leading edge and a trailing edge crack, it was found that a nonlinear quasi-static simulation predicts a leading edge crack would grow at a lower sub-critical dynamic pressure than that of a trailing edge crack. Also, it was seen that if the separated area between the beam and the skin near the wing-root is large, the skin delamination can also grow at sub-critical dynamic pressures.

- *Nonlinear flutter and LCO.* Nonlinear flutter analysis was also carried out for two different layup arrangements for damaged and undamaged wings. For a HALE aircraft wing without any stiffness coupling, it was found that at post-flutter air speeds the interaction between large structural deformations and nonlinear

aerodynamic effects, will make the LCO more complex, such that when the air speed is high enough the LCO becomes chaotic. This was even more pronounced for a damaged wing as the reduction in the overall stiffness would result in higher bending and twist deformations. However, for a wing with a negative bending-twist stiffness coupling resulting from a positive symmetric layup the effects of nonlinear aerodynamics were dominant. This is because the stiffness coupling prevents the wing from undergoing very large deformation, and the LCO would never become chaotic; it remains periodic even at post-flutter conditions. However, for this case, period doubling can occur with increasing the air speed.

- *ROM and flutter suppression system.* A ROM with only a few dominant modes of the FOM was constructed using POD and the method of snapshots. The ROM was exploited to design a flutter suppression system where the wing-tip velocity and twist rate were measured by sensors and fed-back to the controller to determine the deflection of the trailing edge flap. The controller's task, then, was to provide additional damping to the system and force the wing-tip velocities to zero. It was shown that the controller could be used as a regulator, to bring the wing to a trim condition, as well as a flutter suppression to damp out the detrimental oscillations of the wing. It was also demonstrated that the control system is robust enough even when some of flap control power is lost, and also in the presence of crack. The effects of non-collocated sensor and actuator pairs was also studied to find out if the flap were moved far from the sensor towards the wing-root, whether the controller would be able to completely remove unwanted fluctuations. The simuluation results show that this effect is akin to the partial loss of the flap control power.

6.2 Future Work

This research was an initial, yet important, step towards providing a computationally economical method for rigorous aeroelastic analysis of damaged HALE aircraft wings. Several improvements can be suggested for future research in order to expand the scope and applicability of the method.

- *Adding rigid body DOF.* Flight dynamic equations are absent from the present approach and, thus, it is applicable to the structures with no rigid body DOF, such as an aircraft flying at cruise conditions or a wing tested in a wind tunnel. Therefore, the method in its current form cannot be used for flight dynamics problems. By including rigid body DOF to the formulation, the joined 3D/1D model may well be employed to study the effects of various maneuvers and flight conditions on the aeroelastic behavior of HALE aircrafts.

- *Using an aerodynamic model acting on the 3D part.* In the present research, it has been assumed that aerodynamic loads are not directly acting on the 3D part of the model, which encompasses only a small area of the wing. Although this assumption is expedient, adding a simplified aerodynamic model for the 3D part would result in more reliable analysis results.

- *Expanding the applicability of the method to low $\mathcal{AR}$ wings.* The present joined solid/beam (3D/1D) model was developed specifically for HALE aircraft wings, which have a very high $\mathcal{AR}$. A similar approach can be pursued to develop a joined solid/plate (3D/2D) model for low to moderate $\mathcal{AR}$ wings. If such an approach is sought then it would become necessary to integrate the 2D structure with a low-order aerodynamic model, such as a vortex lattice or panel method, to compute unsteady aerodynamic loads. It is true that, compared with joined 3D/1D model, the computational cost would be higher for a joined 3D/2D model.

However, it would still be more economic than a full 3D coupled CFD/CSD analysis.

- *Optimization and studying different damage scenarios.* The present work was focused on investigating the effects of existing damage on the aeroelastic behavior of HALE aircraft wings. Therefore, it was assumed that both the size and location of the damage were known *a priori*. An interesting subject would be to use the joined model when the damage characteristics are not predetermined. Accordingly, stochastic and statistical methods can also be invoked to predict the size and location of damage. The effects of flutter on structural fatigue can also be studied in the future. The method can also be assessed using structural data of operational aircraft. Typical structural optimization problems are computationally intensive, requiring several rounds of simulations. The joined 3D/1D approach may also be potentially used for that purpose, greatly reducing the computational cost.

- *Controller optimization.* The designed flutter suppression system has not been optimized for the best performance in terms of flap deflection. In practice, therefore, the actuator might saturate and fail to provide the required input. Considering actuator's rate and position saturation while designing the controller is recommended as a future work. The sensor/actuator placement needs optimization as well to deliver the best performance of the control system. Also, if rigid-body DOF would be present, flap deflection required for flutter suppression might conflict with the required input for trimming aircraft in lateral/directional channel. A separate actuation mechanism, such as a piezoelectric sensor/actuator, might be employed to tackle the issue.

REFERENCES

[1] D. H. Hodges, *Nonlinear Composite Beam Theory*. Reston Virginia: AIAA, 2006.

[2] W. Yu, D. H. Hodges, and J. C. Ho, "Variational asymptotic beam sectional analysis – an updated version," *International Journal of Engineering Science*, vol. 59, pp. 40–64, 2012.

[3] K. S. Surana, "Isoparametric elemetns for cross-sepctional properties and stress analysis of beams," *International Journal for Numerical Methods in Engineering*, vol. 14, pp. 475–497, 1979.

[4] ——, "Transition finite-elements for axisymmetric stress-analysis," *International Journal for Numerical Methods in Engineering*, vol. 15, pp. 809–832, 1980.

[5] ——, "Transition finite-elements for three dimensional stress analysis," *International Journal for Numerical Methods in Engineering*, vol. 15, pp. 991–1020, 1980.

[6] ——, "Geometrically non-linear formulation for the three dimensional solid-shell transition finite elements," *Computers and Structures*, vol. 15, pp. 549–566, 1982.

[7] W. F. Cofer and K. M. Will, "A three-dimensional, shell-solid transition element for general nonlinear analysis," *Computers and Structures*, vol. 38, pp. 449–462, 1991.

[8] T. C. Gmür and A. M. Schorderet, "A set of three-dimensional solid to shell transition elements for structural dynamics," *Computers and Structures*, vol. 46, pp. 583–591, 1993.

[9] T. C. Gmür and R. H. Kauten, "Three-dimensional solid to beam transition elements for structural dynamics analysis," *International Journal for Numerical Methods in Engineering*, vol. 36, pp. 1429–1444, 1993.

[10] C. R. Dohrmann and S. W. Key, "A transition element for uniform strain hexahedral and tetrahedral finite elements," *International Journal for Numerical Methods in Engineering*, vol. 44, pp. 1933–1950, 1999.

[11] C. R. Dohrmann, S. W. Key, and M. W. Heinstein, "Methods for connecting dissimilar three-dimensional finite element meshes," *International Journal for Numerical Methods in Engineering*, vol. 47, pp. 1057–1080, 2000.

[12] E. Garusi and A. Tralli, "A hybrid stress-assumed transition element for solid-to-beam and plate-to-beam connections," *Computers and Structures*, vol. 80, pp. 105–115, 2002.

[13] K. S. Chavan and P. Wriggers, "Consistent coupling of beam and shell models for thermo-elastic analysis," *International Journal For Numerical Methods In Engineering*, vol. 59, pp. 1861–1878, 2004.

[14] J. I. Curiskis and S. Valliappan, "A solution algorithm for linear constraint equations in finite element analysis," *Computers and Structures*, vol. 8, pp. 117–124, 1978.

[15] J. F. Abel and M. S. Shephard, "An algorithm for multipoint constraints in finite element analysis," *International Journal for Numerical Methods in Engineering*, vol. 14, pp. 464–467, 1979.

[16] M. S. Shephard, "Linear multipoint constraints applied via transformation as part of a direct stiffness assembly process," *International Journal for Numerical Methods in Engineering*, vol. 20, pp. 2107–2112, 1984.

[17] M. A. Aminpour, J. B. Ransom, and S. L. McCleary, "Coupled analysis of independently modelled finite element subdomains," in *33rd AIAA/ASME/ASCE/AHS/ASC Structures, Structural Dynamics, and Materials Conference, Dallas, TX*, 1992.

[18] ——, "A coupled analysis method for structures with independently modelled finite element subdomains," *International Journal for Numerical Methods in Engineering*, vol. 38, pp. 3695–3718, 1995.

[19] J. M. Housner, M. A. Aminpour, C. DVavila, J. E. Schiermeier, W. J. Stroud, J. B. Ransom, and R. E. Gillian, "An interface element for global/local and substructuring analysis," in *MSC 1995 World Users Conference, Los Angeles, CA*, 1995.

[20] M. A. Aminpour and T. Krishnamurthy, "A two-dimensional interface element for multi-domain analysis of independently modelled three-dimensional finite element meshes," in *38th AIAA/ASME/ASCE/AHS/ASC Structures, Structural Dynamics and Materials Conference, Kissimmee, FL*, 1997.

[21] J. E. Schiermeier, R. Kansakar, D. Mong, J. B. Ransom, M. A. Aminpour, and W. J. Stroud, "P-version interface elements in global/local analysis,"

International Journal For Numerical Methods In Engineering, vol. 53, pp. 181–206, 2002.

[22] D. J. Monaghan, I. W. Doherty, D. M. Court, and C. G. Armstrong, "Coupling 1d beams to 3d bodies," in *7th International Meshing Roundtable Sandia National Laboratories Dearborn Michigan*, 1998.

[23] R. W. McCune, C. G. Armstrong, and D. J. Robinson, "Mixed-dimensional coupling in finite element models," *International Journal For Numerical Methods In Engineering*, vol. 49, pp. 725–750, 2000.

[24] K. W. Shim, D. J. Monaghan, and C. G. Armstrong, "Mixed dimensional coupling in finite element stress analysis," *Engineering with Computers*, vol. 18, pp. 241–252, 2002.

[25] I. V. Avdeev, A. I. Borovkov, O. L. Kiylo, M. R. Lovell, and D. O. Jr, "Mixed 2d and beam formulation for modeling sandwich structures," *Engineering Computations*, vol. 19, pp. 451–466, 2002.

[26] H. Song and D. H. Hodges, "Rigorous joining of asymptotic beam models to three-dimensional finite element models," *Computer Modeling in Engineering and Sciences*, vol. 85, no. 3, pp. 239 –250, 2012.

[27] H. S. Hoseini and D. H. Hodges, "Joining 3-d finite elements to variational asymptotic beam models," in *57th AIAA/ASCE/AHS/ASC Structures, Structural Dynamics, and Materials Conference, San Diego, CA*, 2016.

[28] M. Goland and Y. L. Luke, "The flutter of a uniform wing with tip weights," *Journal of Applied Mechanics*, vol. 15, pp. 13–20, 1948.

[29] J. M. Housner and M. Stein, "Flutter analysis of swept-wing subsonic aircraft with parametric studies of composite wings," NASATN–D–7539, Tech. Rep., 1974.

[30] L. Librescu and O. Song, "On the static aeroelastic tailoring of composite aircraft swept wings modelled as thin-walled beam structures," *Composite Engineering*, vol. 2, no. 5–7, pp. 497–512, 1992.

[31] M. Lillico, R. Butler, S. Guo, and J. R. Banerjee, "Aeroelastic optimization of composite wings using the dynamic stiffness method," *Aeronautical Journal*, vol. 101, pp. 77–86, 1997.

[32] S. A. Fazelzadeh and H. Sadat-Hoseini, "Nonlinear flight dynamics of a flexible aircraft subjected to aeroelastic and gust loads," *Journal of Aerospace Engineering*, vol. 25, no. 1, pp. 51–63, 2011.

[33] T. A. Weisshaar, "Aeroelastic tailoring of forward swept composite wings," *Journal of Aircraft*, vol. 18, no. 8, pp. 669–676, 1981.

[34] I. Lottati, "Flutter and divergence aeroelastic characteristics for composite forward swept cantilevered wing," *Journal of Aircraft*, vol. 22, no. 11, pp. 1001–1007, 1985.

[35] J. A. Green, "Aeroelastic tailoring of aft-swept high-aspect-ratio composite wings," *Journal of Aircraft*, vol. 24, no. 11, pp. 812–819, 1987.

[36] L. Librescu, L. Meirovitch, and O. Song, "Refined structural modeling for enhancing vibrational and aeroelastic characteristics of composite aircraft wing," *Recherche Aerospatiale*, pp. 715–724, 1996.

[37] H. S. Hoseini and D. H. Hodges, "Aeroelastic analysis of high aspect ratio wings using joined 3d finite elements and variational asymptotic beam models," in *58th AIAA/ASCE/AHS/ASC Structures, Structural Dynamics, and Materials Conference, Grapevine, TX*, 2017.

[38] E. Livne, "Future of airplane aeroelasticity," *Journal of Aircraft*, vol. 40, no. 6, pp. 1066–1092, 2003.

[39] E. Livne and T. A. Weisshaar, "Aeroelasticity of nonconventional airplane configurations: past and future," *Journal of Aircraft*, vol. 40, no. 6, pp. 1047–1065, 2003.

[40] M. A. Shubov, "Flutter phenomenon in aeroelasticity and its mathematical analysis," *Journal of Aerospace Engineering*, vol. 19, pp. 1–12, 1 2006.

[41] M. J. C. Henshaw *et al.*, "Non-linear aeroelastic prediction for aircraft applications," *Progress in Aerospace Sciences*, vol. 43, pp. 65–137, 2007.

[42] D. Tang and E. H. Dowell, "Experimental and theoretical study on aeroelastic response of high-aspect-ratio wings," *AIAA Journal*, vol. 39, no. 8, pp. 1430–1441, 2001.

[43] C. T. Tran and D. Petot, "Semi-empirical model for the dynamic stall of airfoils in view of the application to the calculation of responses of a helicopter blade in forward flight," *Vertica*, vol. 5, no. 1, pp. 35–53, 1981.

[44] D. Tang and E. H. Dowell, "Effects of geometric structural nonlinearity on flutter and limit cycle oscillations of high-aspect-ratio wings," *Journal of Fluid and Structures*, vol. 19, pp. 291–306, 2004.

[45] M. J. Patil, D. H. Hodges, and C. E. S. Cesnik, "Limit cycle oscillations in high-aspect-ratio wings," *Journal of Fluids and Structures*, vol. 15, pp. 107–132, 2001.

[46] ——, "Nonlinear aeroelasticity and flight dynamics of high-altitude long-ednurance aircraft," *Journal of Aircraft*, vol. 38, no. 1, pp. 88–94, 2001.

[47] M. J. Patil and D. H. Hodges, "On the importance of aerodynamic and structural geometrical nonlinearities in aeroelastic behavior of high-aspect-ratio wings," *Journal of Fluids and Structures*, vol. 19, no. 7, pp. 905 –915, 2004.

[48] ——, "Flight dynamics of highly flexible flying wings," *Journal of Aircraft*, vol. 43, no. 6, pp. 1790–1799, 2006.

[49] Z. Jian and X. Jinwu, "Nonlinear aeroelastic response of high-aspect-ratio flexible wings," *Chinese Journal of Aeronautics*, vol. 22, pp. 355–363, 2009.

[50] D. H. Hodges, "Geometrically-exact, intrinsic theory for dynamics of curved and twisted anisotropic beams," *AIAA Journal*, vol. 41, pp. 1131–1137, 2003.

[51] L. Demasia and E. Livne, "Aeroelastic coupling of geometrically nonlinear structures and linear unsteady aerodynamics: two formulations," *Journal of Fluids and Structures*, vol. 25, pp. 918–935, 5 2009.

[52] A. Arena, W. Lacarbonara, and P. Marzocca, "Nonlinear aeroelastic formulation and postflutter analysis of flexible high-aspect-ratio wings," *Journal of Aircraft*, vol. 50, no. 6, pp. 1748–1764, 2013.

[53] P. Mardanpour, D. H. Hodges, R. Neuhart, and N. Graybeal, "Effect of engine placement on nonlinear trim and stability of flying wing aircraft," in *Proceedings of the 53rd AIAA/ASME/ASCE/AHS/ASC Structures, Structural Dynamics and Materials Conference*, 2012.

[54] ——, "Engine placement effect on nonlinear trim and stability of flying wing aircraft," *Journal of Aircraft*, vol. 50, no. 6, pp. 1716–1725, 2013.

[55] P. Mardanpour, P. W. Richards, O. Nabipour, and D. H. Hodges, "Effect of multiple engine placement on aeroelastic trim and stability of flying wing aircraft," *Journal of Fluids and Structures*, vol. 44, pp. 67–86, 2014.

[56] P. Mardanpour, D. H. Hodges, and R. Rezvani, "Nonlinear aeroelasticity of high-aspect-ratio wings excited by time-dependent thrust," *Nonlinear Dynamics*, vol. 75, no. 3, pp. 475–500, 2014.

[57] D. A. Peters, S. Karunamoorthy, and W. M. Cao, "Finite state induced flow models; part i: two-dimensional thin airfoil," *Journal of Aircraft*, vol. 32, no. 2, pp. 313 –322, 1995.

[58] M. Castellani, J. E. Cooper, and Y. Lemmens, "Nonlinear static aeroelasticity of high aspect ratio wing aircraft by fem and multibody methods," in *15th Dynamics Specialists Conference, AIAA SciTech Forum, San Diego, California*, 2016.

[59] F. E. Eastep, V. B. Venkayya, and V. A. Tishler, "Divergence speed degradation of forward-swept wings with damaged composite skin," *Journal of Aircraft*, vol. 21, no. 11, pp. 921–923, 1984.

[60] W. Chen and H. Lin, "Flutter analysis of thin cracked panels using the finite element method," *AIAA Journal*, vol. 23, no. 5, pp. 795–801, 1985.

[61] T. W. Strganac and Y. I. Kim, "Aeroelastic behavior of composite plates subject to damage growth," *Journal of Aircraft*, vol. 33, no. 1, pp. 68–73, 1996.

[62] D. Yuting and Y. Chao, "Methods and advances in the study of aeroelasticity with uncertainties," *Chinese Journal of Aeronautics*, vol. 27, pp. 461–474, 2014.

[63] M. L. Spearman, "Wind-tunnel studies of the effects of stimulated damage on the aerodynamic characteristics of airplanes and missiles," NASA Langley Research Center, Hampton, VA, NASA-TM-84588, 1982.

[64] N. J. Lindsley, P. S. Berany, and C. L. Pettitz, "Effects of uncertainty on nonlinear plate aeroelastic response," in *43rd AIAA/ASME/ASCE/AHS/ASC Structures, Structural Dynamics and Materials Conference, Denver, CO*, 2002.

[65] C. L. Pettit, "Uncertainty quantification in aeroelasticity: recent results and research challenges," *Journal of Aircraft*, vol. 41, no. 5, pp. 1217–1229, 2004.

[66] T. Ueda, "Aeroelastic analysis considering structural uncertainty," *Aviation*, vol. 9, no. 1, pp. 3–7, 2005.

[67] S. Murugan, R. Ganguli, and D. Harursampath, "Aeroelastic response of composite helicopter rotor with random material properties," *Journal of Aircraft*, vol. 45, no. 1, pp. 306–322, 2008.

[68] D. M. Pitt, D. P. Haudrich, M. J. Thomas, and K. E. Griffin, "Probabilistic aeroelastic analysis and its implications on flutter margin requirements," in *49th AIAA/ASME/ASCE/AHS/ASC Structures, Structural Dynamics and Materials Conference, Schaumburg, IL*, 2008.

[69] H. H. Khodaparast, J. E. Mottershead, and K. J. Badcock, "Propagation of structural uncertainty to linear aeroelastic stability," *Computers and Structures*, vol. 88, pp. 223–236, 2010.

[70] A. V. Styuart, E. Livne, L. Demas, and M. Mor, "Flutter failure risk assessment for damage-tolerant composite aircraft structures," *AIAA Journal*, vol. 49, no. 3, pp. 655–669, 2011.

[71] S. Wu and E. Livne, "Probabilistic aeroservoelastic reliability assessment considering control system component uncertainty," *AIAA Journal*, vol. 54, no. 8, pp. 2507–2520, 2016.

[72] R. K. Kapania and F. Castel, "A simple element for aeroelastic analysis of undamaged and damaged wings," *AIAA Journal*, vol. 28, no. 2, pp. 329–337, 1990.

[73] H. Zhang, "Nonlinear aeroelastic effects in damaged composite aerospace structures," Master's thesis, Georgia Institute of Technology, Atlanta, GA, 1996.

[74] B. Douxchamps, "Nonlinear aeroelastic effects in damaged composite aileron-wing structures," Master's thesis, Georgia Institute of Technology, Atlanta, GA, 1997.

[75] O. A. Bauchau, H. Zhang, R. G. Loewy, and S. N. Atluri, "Nonlinear aeroelastic effects in damaged composite aerospace structures," in *35th AIAA Aerospace Sciences Meeting and Exhibit, Reno, NV*, 1997.

[76] T. Kim, S. N. Atluri, and R. G. Loewy, "Modeling of microcrack damaged composite plates undergoing nonlinear bimodular flutter oscillations," *AIAA Journal*, vol. 36, no. 4, pp. 598–606, 1998.

[77] K. Wang, D. J. Inman, and C. R. Farrar, "Modeling and analysis of a cracked composite cantilever beam vibrating in coupled bending and torsion," *Journal of Sound and Vibration*, vol. 284, pp. 23–49, 2005.

[78] K. Wang and D. J. Inman, "Crack-induced effects on aeroelasticity of an unswept composite wing," *AIAA Journal*, vol. 45, no. 3, pp. 542–551, 2007.

[79] H. J. Conyers, "The effect of wing damage on aeroelastic behavior," PhD thesis, Duke University, Durham, NC, 2009.

[80] H. J. Conyers, E. H. Dowell, and K. C. Hall, "Aeroelastic studies of a rectangular wing with a hole: correlation of theory and experiment," in *2010 Aerospace Systems Conference, Los Angeles, CA*, 2010.

[81] T. D. Dang, R. K. Kapania, and M. J. Patil, "Analytical modeling of cracked thin-walled beams under torsion," *AIAA Journal*, vol. 48, no. 3, pp. 664–675, 2010.

[82] G. Kerschen, J. C. Golinval, A. F. Vakakis, and L. A. Bergman, "The method of proper orthogonal decomposition for dynamic characterization and order reduction of mechanical systems: an overview," *Nonlinear Dynamics*, vol. 41, pp. 147–169, 2005.

[83] J. P. Thomas, K. C. Hall, and E. H. Dowell, "Reduced-order aeroelastic modeling using proper orthogonal decompositions," in *International Forum of Aeroelasticity and Structural Dynamics, Williamsburg*, 1999.

[84] K. C. Hall, J. P. Thomas, and E. H. Dowell, "Proper orthogonal decomposition technique for transonic unsteady aerodynamic flows," *AIAA Journal*, vol. 38, no. 10, pp. 1853–1862, 2000.

[85] T. Lieu and M. Lesoinne, "Parameter adaptation of reduced order models for three-dimensional flutter analysis," in *42nd AIAA Aerospace Sciences Meeting and Exhibit, Reno, Nevada, 5 - 8 January*, 2004.

[86] T. Lieu, C. Farhat, and M. Lesoinne, "Reduced-order fluid/structure modeling of a complete aircraft configuration," *Computer Methods in Applied Mechanics and Engineering*, vol. 195, pp. 5730–5742, 2006.

[87] D. Amsallem and C. Farhat, "Interpolation method for adapting reduced-order models and application to aeroelasticity," *AIAA Journal*, vol. 47, no. 7, pp. 1803–1813, 2008.

[88] D. Amsallem, J. Cortial, K. Carlberg, and C. Farhat, "On-demand cfd-based aeroelastic predictions using a database of reduced-order bases and models," in *47th AIAA Aerospace Sciences Meeting Including The New Horizons Forum and Aerospace Exposition, Orlando, Florida, 5 - 8 January*, 2009.

[89] K. B. Lazarus, E. E. Crawley, and C. Y. Lin, "Fundamental mechanisms of aeroelastic control with control surface and strain actuation," *Journal of Guidance, Control, and Dynamics*, vol. 18, no. 1, pp. 10–17, 1995.

[90] A. M. Lucas, J. Valasek, and T. W. Strganac, "Gust load alleviation of an aeroelastic system using nonlinear control," in *50th AIAA/ASME/ASCE/AHS/ASC Structures, Structural Dynamics and Materials Conference, Palm Springs, CA*, 2009.

[91] V. S. Suryakumar, Y. Babbar, T. W. Strganac, and A. S. Mangalam, "Control of a nonlinear wing section using fly-by-feel sensing," in *AIAA Atmospheric Flight Mechanics Conference, AIAA AVIATION Forum, Dallas, TX*, 2015.

[92] S. A. Fazelzadeh, A. Rasti, and H. Sadat-Hoseini, "Optimal flutter suppression of nonlinear typical wing section using time-domain finite elements method," *Journal of Aerospace Engineering*, vol. 27, no. 5, pp. 1–10, 2013.

[93] M. J. Patil, "Nonlinear aeroelastic analysis, flight dynamics, and control of a complete aircraft," PhD thesis, Georgia Institute of Technology, Atlanta, GA, 1999.

[94] H. Sadat-Hoseini, S. A. Fazelzadeh, A. Rasti, and P. Marzocca, "Final approach and flare control of a flexible aircraft in crosswind landings," *Journal of Guidance, Control, and Dynamics*, vol. 36, no. 4, pp. 946–957, 2013.

[95] H. S. Hoseini and D. H. Hodges, "Flutter suppression for finite element modeling of damaged hale aircraft wings," in *2018 AIAA/ASCE/AHS/ASC Structures, Structural Dynamics, and Materials Conference, Kissimmee, FL*, 2018.

[96] M. Karpel, "Design for active flutter suppression and gust alleviation using state-space aeroelastic modeling," *Journal of Aircraft*, vol. 19, no. 3, pp. 221–227, 1982.

[97] J. J. Block and T. W. Strganac, "Applied active control for a nonlinear aeroelastic structure," *Journal of Guidance, Control, and Dynamics*, vol. 21, no. 6, pp. 838–845, 1998.

[98] K. D. Frampton and R. L. Clark, "Experiments on control of limit-cycle oscillations in a typical section," *Journal of Guidance, Control, and Dynamics*, vol. 23, no. 5, pp. 956–960, 2000.

[99] J. Ko, T. W. Strganac, J. L. Junkins, M. R. Akella, and A. J. Kurdila, "Structured model reference adaptive control for a wing section with structural nonlinearity," *Journal of Vibration and Control*, vol. 8, pp. 553–573, 2002.

[100] A. Behal, P. Marzocca, V. M. Rao, and A. Gnann, "Nonlinear adaptive control of an aeroelastic two-dimensional lifting surface," *Journal of Guidance, Control, and Dynamics*, vol. 29, no. 2, pp. 382–390, 2006.

[101] K. W. Lee and S. N. Singh, "Global robust control of an aeroelastic system using output feedback," *Journal of Guidance, Control, and Dynamics*, vol. 30, no. 1, pp. 271–275, 2007.

[102] X. Wei and J. E. Mottershead, "Robust passivity-based continuous sliding-mode control for under-actuated nonlinear wing sections," *Aerospace Science and Technology*, vol. 60, pp. 9–19, 2017.

[103] P. Ghorawat, K. W. Lee, S. N. Singh, and G. Chmaj, "Robust finite-time control of an uncertain aeroelastic system using leading-and trailing-edge flaps," *Advances in Systems Science*, vol. 539, pp. 318–328, 2017.

[104] B. Raghavan, M. J. Patil, and C. A. Woolsey, "Trajectory tracking for high aspect-ratio flying wings," in *AIAA Atmospheric Flight Mechanics Conference and Exhibit, Honolulu, HI*, 2008.

[105] J. Ouellette, B. Raghavan, M. J. Patil, and R. K. Kapania, "Flight dynamics and structural load distribution for a damaged aircraft," in *AIAA Atmospheric Flight Mechanics Conference, Chicago, Il*, 2009.

[106] V. S. Suryakumar, Y. Babbar, T. W. Strganac, and A. S. Mangalam, "A load-based feedback approach for distributed aeroservoelastic control," in *AIAA Atmospheric Flight Mechanics Conference, AIAA Aviation Forum, Washington, D.C.*, 2016.

[107] M. J. Patil and D. H. Hodges, "Output feedback control of the nonlinear aeroelastic response of a slender wing," *Journal of Guidance, Control, and Dynamics*, vol. 25, no. 2, pp. 302–308, 2002.

[108] P. W. Richards, "Design strategies for rotorcraft blades and half aircraft wings ap[plied to damage tolerant wind turbine blade design," PhD thesis, Georgia Institute of Technology, Atlanta, GA, 2015.

[109] C. M. Shearer and C. E. S. Cesnik, "Nonlinear flight dynamics of very flexible aircraft," *Journal of Aircraft*, vol. 44, no. 5, pp. 1528–1545, 2007.

[110] ——, "Trajectory control for very flexible aircraft," *Journal of Guidance, Control, and Dynamics*, vol. 31, no. 2, pp. 340–357, 2008.

[111] B. Raghavan, "Flight dynamics and control of highly flexible flying-wings," PhD thesis, Virginia Polytechnic Institute and State University, Blacksburg, VA, 2009.

[112] B. Raghavan and M. J. Patil, "Flight dynamics of high aspect-ratio flying wings: effect of large trim deformation," *Journal of Aircraft*, vol. 46, no. 5, pp. 1808–1812, 2009.

[113] ——, "Flight control for flexible, high-aspect-ratio flying wings," *Journal of Guidance, Control, and Dynamics*, vol. 33, no. 1, pp. 64–74, 2010.

[114] D. Amsallem, J. Cortial, K. Carlberg, and C. Farhat, "A method for interpolating on manifolds structrual dynamics reduced-order models," *International Journal for Numerical Methods in In Engineering*, vol. 80, pp. 1241–1258, 2009.

[115] D. Amsallem and C. Farhat, "An online method for interpolating linear parametric reduced-order models," *SIAM Journal on Scientific Computing*, vol. 47, no. 5, pp. 2169–2198, 2011.

[116] T. Bui-Thanh, K. Willcox, O. Ghattas, and B. van Bloemen Waanders, "Goal-oriented, model-constrained optimization for reduction of large-scale systems," *Journal of Computational Physics*, vol. 224, pp. 880–896, 2007.

[117] D. Amsallem and C. Farhat, "Stabilization of projection-based reduced-order models," *International Journal for Numerical Methods in Engineering*, vol. 91, pp. 358–377, 2012.

[118] O. A. Bauchau, *Flexible Multibody Dynamics*. London: Springer, 2011.

[119] ——, *Dymore User's Manual*. Atlanta, GA: Georgia Institute of Technology, 2007.

[120] L. Sirovich, "Turbulence and the dynamics of coherent structures, partsi-iii," *Quarterly of Applied Mathematics*, vol. 45, no. 3, pp. 561–590, 1987.

[121] A. Preumont, *Vibration Control of Active Structures*. Netherlands: Kluwer Academic Publishers, 1997.

[122] N. Moës, J. Delbow, and T. Belytschko, "A finite element method for crack growth without remeshing," *International Journal for Numerical Methods in Engineering*, vol. 46, pp. 131–150, 1 1999.

[123] G. Alfano and M. A. Crisfield, "Finite element interface models for the delamination analysis of laminated composites: mechanical and computational issues," *International Journal for Numerical Methods in Engineering*, vol. 50, no. 7, pp. 1701–1736, 2001.

[124] T. L. Anderson, *Fracture Mechanics*. Boca Raton: CRC Press, 2005.

[125] K. Park and G. H. Paulino, "Computational implementation of the ppr potential-based cohesive model in abaqus: educational perspective," *Engineering Fracture Mechanics*, vol. 93, pp. 239–262, 2012.

[126] L. Librescu and O. Song, *Thin-Walled Composite Beams Theory and Application*. Netherlands: Springer, 2006.